THE UNIVERSITY *of* EDINBURGH

Theory of elastic and inelastic X-ray scattering

Andrés Moreno Carrascosa

Thesis submitted for the degree of Doctor of Philosophy

University of Edinburgh

2017

Declaration of Authorship

I, Andrés MORENO CARRASCOSA, declare that this thesis titled, "Theory of elastic and inelastic X-ray scattering." and the work presented in it are my own. I confirm that:

- This work was done wholly or mainly while in candidature for a research degree at this University.
- Where any part of this thesis has previously been submitted for a degree or any other qualification at this University or any other institution, this has been clearly stated.
- Where I have consulted the published work of others, this is always clearly attributed.
- Where I have quoted from the work of others, the source is always given. With the exception of such quotations, this thesis is entirely my own work.
- I have acknowledged all main sources of help.
- Where the thesis is based on work done by myself jointly with others, I have made clear exactly what was done by others and what I have contributed myself.

Signed:

Date:

"Science is a bit like the joke about the drunk who is looking under a lamppost for a key that he has lost on the other side of the street, because that is where the light is. It has no other choice."

Noam Chomsky

"We especially need imagination in science. It is not all mathematics, nor all logic, but it is somewhat beauty and poetry."

María Montessori

Abstract

X-rays have been widely exploited to unravel the structure of matter since their discovery in 1895. Nowadays, with the emergence of new X-ray sources with higher intensity and very short pulse duration, notably X-ray Free Electron Lasers, the number of experiments that may be considered in the X-ray regime has increased dramatically, making the characterization of gas phase atoms and molecules in space and time possible. This thesis explores in the theoretical analysis and calculation of X-ray scattering atoms and molecules, far beyond the independent atom model.

A method to calculate inelastic X-ray scattering from atoms and molecules is presented. The method utilizes electronic wavefunctions calculated using *ab-initio* electronic structure methods. Wavefunctions expressed in Gaussian type orbitals allow for efficient calculations based on analytical Fourier transforms of the electron density and overlap integrals. The method is validated by extensive calculations of inelastic cross-sections in H, He^+, He, Ne, C, Na and N_2. The calculated cross-sections are compared to cross-sections from inelastic X-ray scattering experiments, electron energy-loss spectroscopy, and theoretical reference values.

We then begin to account for the effect of nuclear motion, in the first instance by predicting elastic X-ray scattering from state-selected molecules. We find strong signatures corresponding to the specific vibrational and rotational state of (polyatomic) molecules.

The ultimate goal of this thesis is to study atomic and molecular wavepackets using time-resolved X-ray scattering. We present a theoretical framework based on quantum electrodynamics and explore various elastic and

inelastic limits of the scattering expressions. We then explore X-ray scattering from electronic wavepackets, following on from work by other groups, and finally examine the time-resolved X-ray scattering from non-adiabatic electronic-nuclear wavepackets in the H_2 molecule, demonstrating the importance of accounting for the inelastic effects.

Lay summary

X-ray scattering and diffraction is enormously useful to identify and characterise matter. X-rays interact very weakly with matter as they only interact with electrons, and for a long time it has been necessary to rely on crystalline samples that present a very large number of molecules in almost identical orientations. The emergence of new, much more intense, X-ray sources such as Free-Electron Lasers make it possible to study samples without intrinsic long-range order e.g. molecules in the gas-phase. In this thesis we aim to predict X-ray scattering using computational tools in gas-phase atoms and molecules.

We demonstrate how atoms and molecules in a specific state interact with X-rays, producing scattering patterns that reflect the physical behaviour of the system. In this case, X-ray scattering is considered to be elastic, without any exchange of energy with the atom or molecule.

The X-rays can also exchange energy with an atom or molecule in an internal process called inelastic X-ray scattering. Inelastic X-ray scattering provide information about the energy levels of a system. In this thesis we present a new computational tool to calculate inelastic X-ray scattering in atoms and molecules.

An important aspect of X-ray Free Electron Lasers is that they deliver the X-rays in very short pulses, which makes it possible to study an atomic or molecular process unfold in time. We explore the time-evolution of atomic or molecular system excited into a nonstationary state or superposition of states using theoretical methods. In the case of a molecule undergoing a chemical reactions, this is sometimes referred to as molecular movie.

Acknowledgements

First, I would like to express my sincere gratitude to my supervisor, Dr Adam Kirrander. His advice, patience and continuous support have been essential during my PhD. Thank you for letting me learn from you.

I would like to thank the other members of the Kirrander group (past and present) for all the help and companionship. They are Minas Stefanou, Darren Bellshaw, Nikola Zotev, Dr Thomas Northey, Dr Maria Tudorovskaya, Dr Kenichiro Saita and Dr David Rogers.

I need to say thank you to all my friends, here and abroad, which make me a better person. Marta thanks you for all the proofreading and all the support in general. Maica, Juanjo, Esther, George, Jon, Pablo and the ones that I forget, thank you all for the great moments.

And last but not least, Mamá, tío, Ángel, muchísimas gracias por haberme guiado hasta aquí, sin vosotros no sería quien soy.

Contents

List of Figures

List of Tables

List of Abbreviations

AIMS	*Ab-initio* Multiple Spawning
AIXRDEI	*Ab-initio* X-ray Diffraction Elastic and Inelastic
CASSCF	Complete Active Space Self-Consistent Field
CASPT2	Complete Active Space Perturbation Theory 2nd order
CI	Configuration Interaction
CSF	Configuration State Function
DESY	Deutsches Elektronen-Synchrotron
DNA	DeoxyriboNucleic Acid
EELS	Electron Energy-Loss Spectroscopy
ESRF	European Synchrotron Radiation Facility
FFT	Fast-Fourier Transform
FLASH	Free-Electron LASer in Hamburg
GOS	Generalised Oscillator Strength
GTO	Gaussian-Type Orbitals
HF	Hartree-Fock
IAM	Independent Atom Model
IXS	Inelastic X-ray Scattering
LCLS	Linac Coherent Light Source
MCE	MultiConfigurational Ehrenfest
MCSCF	MultiConfigurational Self-Consistent Field
MCTDH	MultiConfigurational Time-Dependent Hartree
MRCI	Multi-Reference Configuration Interaction
NIST	National Institute of Standards and Technology
PEC	Potential Energy Curve
QED	Quantum Electro-Dynamics
RPA	Random-Phase Approximation
RPAE	Random-Phase Approximation with Exchange

SACLA	SPring-8 Angstrom Compact free electron LAser
SASE	Self-Amplified Stimulated Emission
SCF	Self-Consistent Field
SD	Slater Determinant
SHARC	Surface-Hopping ARbitrary Couplings
SME	Scattering Matrix Elements
SOD	Second Order Differentiation
TDA	Tamm-Dancoff Approximation
TD-DFT	Time-Dependent Density Functional Theory
TDSE	Time-Dependent Schrödinger Equation
UED	Ultrafast Electron Diffraction
XFEL	X-ray Free-Electron Laser

List of publications

Work from this thesis has been published (or soon will be) in the following papers:

T. Northey *et al. J. Chem. Phys.* **145**. Elastic X-ray scattering from state-selected molecules, 154304 (2016)

A. M. Carrascosa, T. Northey, and A. Kirrander. *Phys. Chem. Chem. Phys.* **19**. Imaging rotations and vibrations in polyatomic molecules with X-ray scattering, 7853 (2017)

A. Moreno Carrascosa and A. Kirrander. *Phys. Chem. Chem. Phys.* **19**. Ab initio calculation of inelastic scattering, 19545 (30 2017)

A. M. Carrascosa and A. Kirrander. *Manuscript*. Time-resolved X-ray scattering from LiF molecules (2017)

A. M. Carrascosa and A. Kirrander. *Manuscript*. Time-resolved X-ray scattering from H-Atom electronic wavepackets (2017)

A. M. Carrascosa *et al. Manuscript*. Time-resolved X-ray scattering from H_2 molecules (2017)

Chapter 1

Introduction

The objective of this thesis is to develop new methods to calculate and characterise X-ray scattering from atoms and molecules in the gas phase. Although predominantly theoretical, this work aims to bridge experiment and theory and to generate a powerful tool to elucidate molecular dynamics.

X-rays were discovered in the late 19th century and continue to play a critical role in physics, chemistry, biomedicine and materials science. At the moment, the emergence of new X-ray sources such as XFELs is enabling studies of non-crystalline samples [7, 8] and time-resolved studies comparable in scope and ambition to ultrafast spectroscopies as demonstrated by recent work from our group [9, 10] as well as others [11–14].

Recent developments in the time resolution of X-ray experiments makes it possible to study ultrafast processes such as electron dynamics and bond-breaking [9]. Ultrafast chemistry, in the time-range of femtoseconds or even attoseconds, has evolved since the first spectroscopic techniques were discovered. From the first X-ray intermediate trapping experiments [15] and the first picosecond-resolution synchrotron experiments [16], to the recent *molecular movies* by ultrafast X-ray and electron scattering [17–20], it has only been thirty years.

Nowadays, the reduction in X-ray pulse duration has allowed the study of different systems using ultrafast X-ray scattering [9, 21, 22]. However, these processes are still not completely characterised from a theoretical point of view. The simulation of ultrafast X-ray scattering processes correctly is one of the main challenges in ultrafast chemistry. For example, the ring-opening reaction of 1,3-cyclohexadiene investigated experimentally in

[21], would benefit from a reliable simulation of nuclear and electronic dynamics in the X-ray scattering process.

The theory and computational procedures necessary to explain ultrafast time-dependent X-ray experiments constitute the basis of this thesis, which follows in the footsteps of previous approaches found in the literature since the 1990s [23] and goes beyond such methods with newly-developed techniques. In the last few years several attempts have been made to explain the explicit time-dependence of a scattering event and the electron dynamics associated with it. With this work we aim to unravel the different ingredients necessary to develop a full quantum electrodynamic description of this contemporary problem. Möller and Henriksen [11, 12] and Santra *et al.*[24, 25] have established the pillars on which the study of ultrafast X-ray scattering rests, and Kowalewski *et al.*[26] followed the assumptions established in [11] to isolate elastic and inelastic contributions on the general X-ray scattering picture. The theory developed here is based in the aforementioned work but it introduces a novel method to interpret and develop the theory necessary to calculate the evolution of the X-ray scattering signal from ultrafast photochemical processes.

Other problems such as the characterisation of inelastic X-ray scattering or state-selected X-ray scattering will also be discussed in this thesis. Electronic structure calculations form a key component in describing these scattering events, and such quantum chemical techniques and their applicability to these problems, which are crucial in the interpretation of recent ultrafast X-ray scattering and ultrafast electronic scattering experiments [27–34] , will be considered.

1.1 Historical background

The first experiments to generate X-rays were reported in 1785 when William Morgan described the characteristics of an early version of the X-ray tube [35], although he was unaware that he was generating and observing X-rays. Instead, the discovery of X-rays is accredited to Wilhem Röntgen

who characterised the first X-rays in 1895 [36]. Since then, this electromagnetic radiation with a wavelength on the order of Ångströms (10^{-10} m) and energy on the order of keV, has been widely exploited.

In 1912, Max von Laue, a former assistant of Max Planck in Berlin, discovered the diffraction of X-rays by crystals [37]. He postulated the wave motion of X-rays and the existence of periodic structures in crystalline materials. However, elucidation of the structure of matter using von Laue's method was difficult as many of the parameters in the experiment were unknown. William L. Bragg conceived a mathematical treatment that relates the distance between crystal planes to the X-ray diffraction angle and the X-ray wavelength, generalizing the Von Laue laws and providing a predictive method to interpret experiments. As a demonstration, William H. Bragg built the first X-ray spectrometer capable of analysing the diffraction angle produced by a fixed X-ray wavelength [38, 39].

Soon after Röntgen's discovery, it was postulated that X-ray-matter interaction produces other types of secondary radiation. In 1897 Sagnac postulated the existence of secondary radiation, explained in 1917 by Professor Barkla of Edinburgh, who discovered that it contained emitted electrons along with X-rays. Lise Meitner in 1922 and, independently, Pierre Victor Auger in 1923 explained the nature of the electrons emitted; they established that a valence electron can be emitted when the X-ray produces an inner-shell electron vacancy in the atom or molecule. Arthur Compton postulated, in the same year, that the X-rays produced in the process can have a longer wavelength than the original beam. This results from the interaction of X-rays with electrons in the molecule, which can present an inelastic component, reducing the energy of the scattered X-ray. This process was named after him as *the Compton effect*.

X-rays have not lost importance over the years. The DNA structure was elucidated using X-ray Crystallography by Watson and Crick in 1953 [40] following the lead of Dorothy Crowfoot Hodgkin who solved the structures of Cholesterol [41] and vitamin B12 [42]. In 1954 David Green, Vernon Ingram and Max Perutz published a seminal paper describing how, in principle, X-ray diffraction could be used for the direct determination of a protein

structure [43]. Perutz along with Kendrew would solve the structure of the protein Myoglobin four years later [44].

1.2 Sources of X-rays

1.2.1 X-ray tubes

The first X-rays were produced in cold cathode tubes, the design of which was improved upon by William Coolidge in order to increase the intensity of the X-rays produced and allow a degree of control over beam parameters such as X-ray energy [45]. The basic design is as follows; a metal filament made of tungsten is heated, emitting electrons which are then accelerated towards the anode. When the electrons strike the anode and they are decelerated, they emit so-called *Bremsstrahlung* (X-rays) with a continuous distribution of energies. However, the spectrum generated has sharp lines superimposed on it as illustrated in Fig. 1.2. These correspond to fluorescence due to the radiative relaxation of an valence electron after an inner-shell vacancy is created by the impact of the accelerated electrons. The emitted energies are characteristic of the material used for the anode. A commonly used material is copper, with K_α and K_β lines at 8047 eV and 8095 eV, respectively [46].

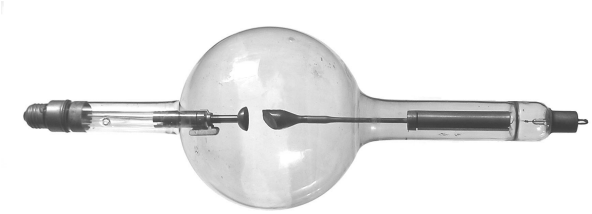

FIGURE 1.1: Photograph of an old Coolidge's tube. Taken from `n6vj.com`

Coolidge's tubes were widely adapted in X-ray diffraction experiments in crystalline samples [38, 47]. However, the overall intensity of X-rays is low and only a small fraction of the photons emitted can be utilized as radiation is emitted isotropically [48]. Synchrotron X-ray radiation, discussed

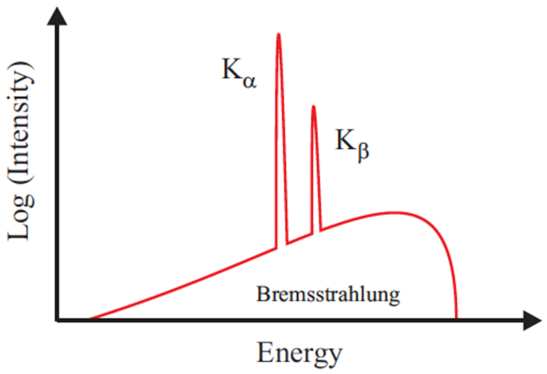

FIGURE 1.2: Spectra produced by an X-ray tube. K_α and K_β represent the fluorescent emission lines embedded into the continuum *Bremsstrahlung*.

next, does not have these drawbacks, presenting higher intensity and tunable X-ray parameters.

1.2.2 Synchrotrons

The first synchrotrons were built in the 1950s, initially for particle collision experiments in high-energy physics [49]. It was soon realised that the synchrotrons constituted a useful source of X-ray radiation, and in the 1970s the first synchrotron purposely built for generating X-rays was constructed (DESY).

To produce synchrotron radiation we use magnets accelerate to electrons which thus emit electromagnetic radiation. This effect is familiar in any charged particle accelerated up to relativistic speeds and it can be seen even in space, as supernovae explosions produce a significant number of high energy electrons moving around magnetic fields. This is the case in the Crab Nebulae (see Fig. 1.3) [50].

In the following we will refer to the term *brilliance* in order to characterise the X-rays produced in these facilities. This parameter is analogous to the X-ray intensity but it also accounts for the collimation of the X-ray and the

divergence of the beam. It can be calculated using the following expression,

$$\text{Brilliance} = \frac{\text{photons}}{\text{second mrad}^2\ \text{mm}^2\ 0.1\%\text{BW}} \tag{1.1}$$

where mrad accounts for the divergence of the X-ray beam, mm measure the size of the focal point in the X-ray and BW refers to the energy bandwidth of the X-ray pulse.

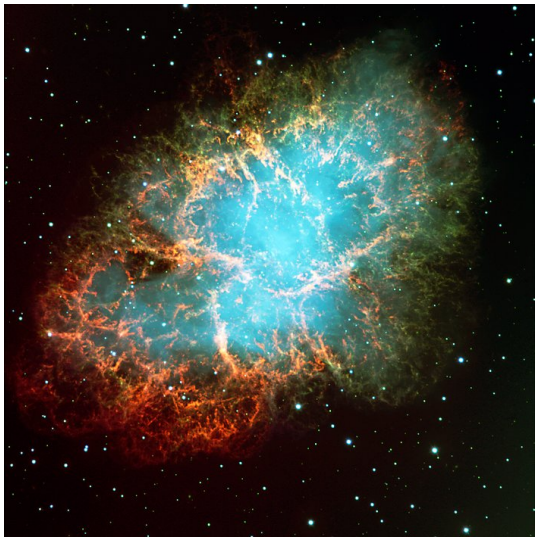

FIGURE 1.3: Photograph of the Crab Nebula in Taurus. One can observe the production of synchrotron radiation around the edges produced by the magnetic field curving the trajectory of high-energy electrons. Taken from `en.wikipedia.org/wiki/Crab_Nebula`

First generation synchrotrons were built using bent magnets in a storage ring. To increase the acceleration produced on electrons these devices were substituted by wigglers and undulators in the second and third generation synchrotrons. These were capable to increase the brilliance of the X-ray radiation produced. An undulator is a device placed in the straight regions of the synchrotron rings. Formed by a sequence of alternative magnets, it forces the electron to oscillate perpendicular to the direction of light (see Fig. 1.4). These oscillations are in phase, enhancing the final radiation field produced. The operation of a wiggler is analogous to the undulator. It does not need a straight portion of the section as it is built as a series of circular

arcs with different polarity. The curved geometry produces a lower electron oscillation angle and therefore a smaller brilliance.

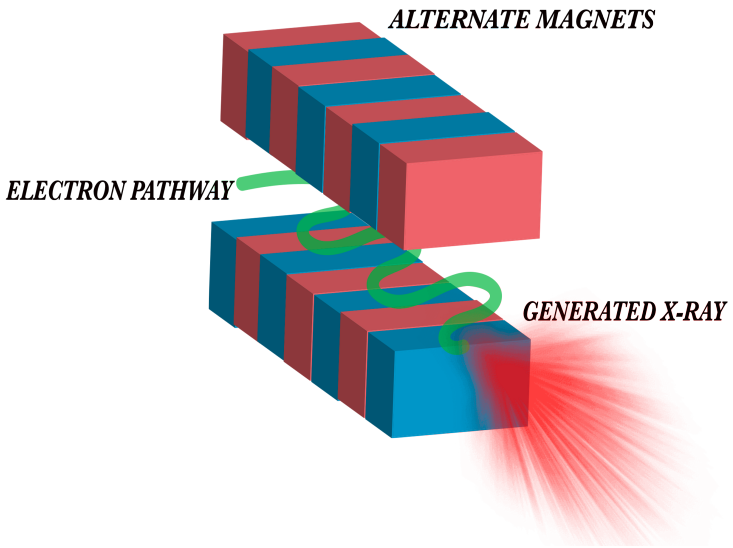

FIGURE 1.4: Scheme of the undulator operation. The electrons pass through alternated magnets producing X-ray radiation.

The European Synchrotron Radiation Facility (ESRF) in Grenoble was the first of the third-generation hard X-ray sources to operate in 1994, achieving an energy of 6 GeV. The ESRF has been followed by the Advanced Photon Source at Argonne National Laboratory in late 1996, and Spring-8 in Harima Science Garden City in Japan in 1997. The high energetic radiation produced by these synchrotrons allows the elucidation of complicated structures with reduced crystallinity [51].

1.2.3 Free-Electron Lasers

The idea of Self-Amplified Stimulated Emission (SASE) was proposed by Madey in 1971 [52] followed by the first operation in a free electron laser in 1977 [53]. Electrons traveling through an undulator are made to oscillate and thus emit photons. If their velocity is sufficiently high, the emitted photons will co-propagate with the electrons, causing them to oscillate coherently in micro-bunches separated by the X-ray wavelength. This process results in coherent and highly directed radiation, organized in short pulses.

The modulated radiation will enhance itself along the device as the field is incremented while the electrons move. This phenomenon is known as SASE and it is the principal effect constituting Free Electron Lasers (see Fig. 1.5). If somehow one could reduce the diameter of each micro-bunch, the effect of radiation would be more localized, generating stronger radiation fields and shorter X-ray pulses. Using linear accelerators with small diameters then produces higher electron densities and consequently higher brilliance.

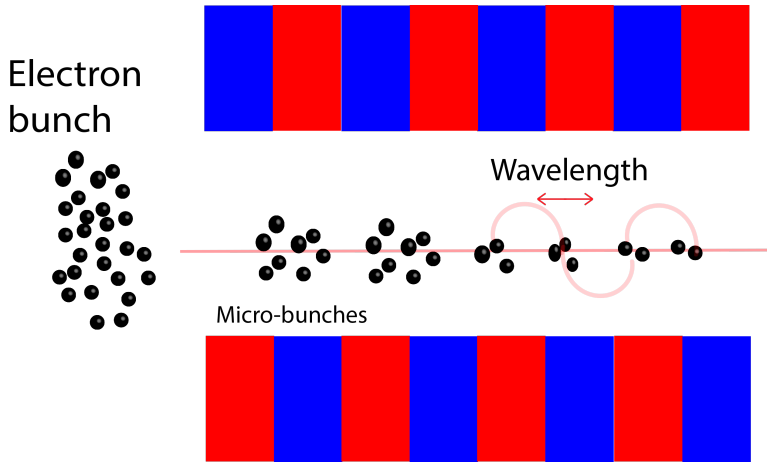

FIGURE 1.5: Schematic representation of SASE effect.

The first free-electron laser , FLASH, was opened in Hamburg in 2005. The energy of the X-rays generated oscillated around tenths of keV, situating FLASH as a soft-X-ray free-electron laser facility. In 2009, the Linac Coherent Light source (LCLS) was the first XFEL to accomplish X-ray energies surpassing 10 keV. It was and continues to be the free-electron laser that generates highest brilliance hard X-ray pulses with lowest pulse-duration. Following the opening of LCLS, another hard-XFEL with the same pulse properties named SACLA, was built in Japan a year after. Nowadays, new facilities are under construction, one of the most important examples being the European XFEL that it is being built close to FLASH. In Fig. 1.6 we can see a comparison of the evolution in the X-rays sources presented above according to the X-ray energy and the maximum pulse brilliance achieved.

The simulations performed by our group, as based on time-resolved

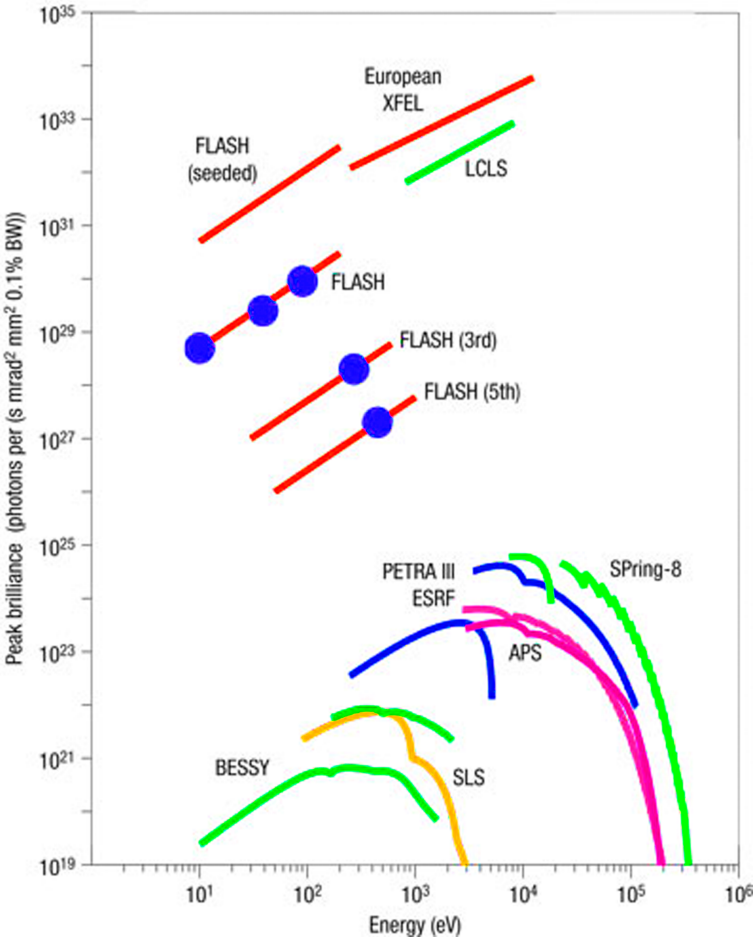

FIGURE 1.6: Comparison of different Synchrotron and X-ray Free Electron Laser sources using the brilliance peak and the photon energies. Figure taken from Ref. [54].

gas phase X-ray scattering experiments, require the intensity and pulse-duration granted by XFELs [2, 9, 55].

1.3 Opportunities at XFELs

1.3.1 Biomolecular X-ray Crystallography

The small scattering cross-section of X-rays produces a weak signal in diffraction. This leads to long data acquisition times, especially when dealing with non-crystalline samples. As biomolecular systems present short-range order, the emergence of X-ray sources such as XFELs entailed a great advance on the macromolecular X-ray crystallography [56]. Likewise, the short X-ray pulses produced by XFELs allow the measuring of X-ray diffraction before the sample gets damaged by the powerful X-ray pulses [57, 58].

The lack of periodic order in the biological samples presents some other inconveniences. Although viruses and other biological entities with ordered structures can be studied by diffraction of isolated samples [59], in most of the cases a biomolecular crystal should be used to obtain a reliable X-ray diffraction. It is important to note that growing big crystals out of hydrophobic compounds is difficult, leading to solutions as the gas-dynamic virtual nozzle proposed by Weierstall *et al.* [60]. Using this technique, successive micro-crystals are passed through the XFEL beam embedded on a liquid jet, were femtosecond X-ray pulses diffract from them. As these micro-crystals posses a random orientation in the jet, data acquisition becomes complicated, requiring subsequent approaches such as a viscose matrix to fix the orientation of the sample or another fixed target methods [61–63].

The higher frequency of repetition expected in the new XFEL facilities will solve all the problems coming from the crystal production and measurement. Faster diffraction detectors will be able to record the diffraction produced by single proteins in solution, overcoming all issues presented when solid samples are required.

1.3.2 Time-resolved X-ray scattering

First experiments using time-resolved X-ray diffraction were performed at the ESRF in Grenoble, where a mechanical chopper was fitted along the X-ray beam giving $\sim$ 100 ps X-ray pulses. A pump-probe scheme was used for this; an optical laser initiates the dynamical process and an X-ray pulse diffracts from the sample at different time delays [64]. Neutze *et al.* performed the first experiments using picosecond X-ray pulses to probe the excited state dynamics of I_2 [8]. Michael Wulff, one of the pioneers in this technique, also collaborated with Richard Neutze mapping the evolution of transient isomers of CH_2I_2 [65] and the photolysis of Br_2 [16, 66]. Although synchrotron experiments opened the way for the time-resolved X-ray experiments, the time-duration of the pulses achieved was not short enough to probe the atomic motions produced during the process.

X-ray free electron lasers can produce intense X-ray pulses of very short duration, making them suitable to study ultrafast chemical dynamics reduced even to the molecular motion. Processes like the structural changes occurring in a chromophore following the absorption of light have been studied using femtosecond X-ray pulses at LCLS [67] and even bond formations in Au oligomer complexes have been mapped using this technique [68].

Another feature associated with the high intensity profile granted by XFELs is the opportunity to study gas-phase ultrafast processes. The internal dynamics of the molecule can be isolated due to the low density of the gas, leading to structural determination by X-ray diffraction at each of the steps in the process. This has been demonstrated widely in the literature, with examples like the study of gas-phase state-selected Iodine molecules [69] or the electrocyclic ring opening reaction of ciclohexadiene [9].

Nowadays, studying coupled nuclear and electronic propagation with Ultrafast X-ray Diffraction [11, 13, 23, 24, 70] is one of the main challenges to achieve using XFELs. This theoretical studies have inspired some of the work presented in Ch. 5 and Ch. 6.

It is important to remark that although X-ray scattering techniques have undergone great advances with the emergence of synchrotrons and XFELs,

other experimental X-ray techniques have also benefited from their appearance. The pulsed X-ray radiation generated in novel sources such as XFELs has made non-linear and X-ray multidimensional spectroscopies a viable proposition. Techniques such as Coulomb explosion imaging use the ultrashort pulse durations and high intensities provided by new X-ray sources [71, 72].

1.4 Electron scattering

The De Broglie wave-particle duality [73] allows considering the electrons as waves with an associated wavelength. In this sense, accelerated electron beams can be used as a probing tool analogous to X-rays. In fact, the elastic and inelastic cross sections produced in X-ray scattering have the same magnitude as in the electron scattering regime. However, at large values of q, the electron scattering process involves more than one interaction, causing the first Born approximation to break down.

To produce accelerated electrons, a device analogous to the X-ray tube is used. Electrons are produced in a cathode and then accelerated towards an anode. Instead of striking the anode material, electrons scatter from the sample producing diffraction patterns. The larger scattering cross-section for electrons with respect to X-rays allows achieving ultrafast time-resolution for the study of molecular systems in the gas phase, as demonstrated by Ahmed Zewail in his numerous studies using ultrafast electron diffraction [74–76].

One of the drawbacks of ultrafast electron diffraction stems from the fact that electrons are charged particles and electron pulses suffer a great dispersion due to the Coulombic repulsion. This broadening limits the electron pulse duration, restricting the production of femtosecond or attosecond electron pulses. Nevertheless, new GeV sources accelerate the electrons up to relativistic speeds, reducing this effect and allowing the production of pulses with shorter time-duration [33]. This new feature, makes the experimental goals of ultrafast electron diffraction (UED) very similar to time-resolved X-ray diffraction ones. Recently, it has been shown by Centurion *et*

al. that the vibrational modes in I_2 can be characterised using UED [14], as well as the evolution of rotational modes in N_2 [17]. New approaches can probe reaction dynamics, as has been proposed by Wilkin *et al.* in the study of photo-dissociation in $C_2F_4I_2$ molecules through this technique (private communication).

Some of the characteristics of electron scattering will be exploited in this thesis, and the theoretical analogies with X-ray scattering will be highlighted in Ch. 4.

1.5 Interaction of X-rays with matter

We now consider the interaction of X-rays with an atom or molecule. Although the total Hamiltonian includes several terms, the interaction term between the radiation and material system governs these processes. The interaction Hamiltonian takes the form [77],

$$\hat{H}_{int} = \hat{p} \cdot \hat{A} + \frac{\hat{A}^2}{2} \tag{1.2}$$

where $\hat{p}$ is the momentum operator and $\hat{A}$ the vector potential describing the electromagnetic field (see Ch. 2 for further details). The first term refers to absorption and emission processes as it only involves one instance of the field, $\hat{A}$, and the second terms correspond to scattering as the vector field, $\hat{A}^2$, appears twice. In the following we will discuss resonant and non-resonant interactions that involve the interaction Hamiltonian.

1.5.1 Resonant X-ray matter interactions

Resonant interactions constitute the basis for X-ray spectroscopy [78, 79]. All resonant interactions are governed by the linear term in the interaction Hamiltonian, $p\hat{A}$, and involve an initial absorption of an X-ray photon [80] which excites a core electron to a virtual or unoccupied level. Considering the typical energies of core electrons, this implies soft X-rays with energies in the range $0.1 - 10$ keV [48]. The absorption of a photon is followed by radiative or Auger decay as depicted in Fig. 1.7. The relative magnitudes of

these two outcomes depend on the lifetime of the core-hole (the larger the energy, the shorter the lifetime), with radiative decay favoured by longer lifetimes.

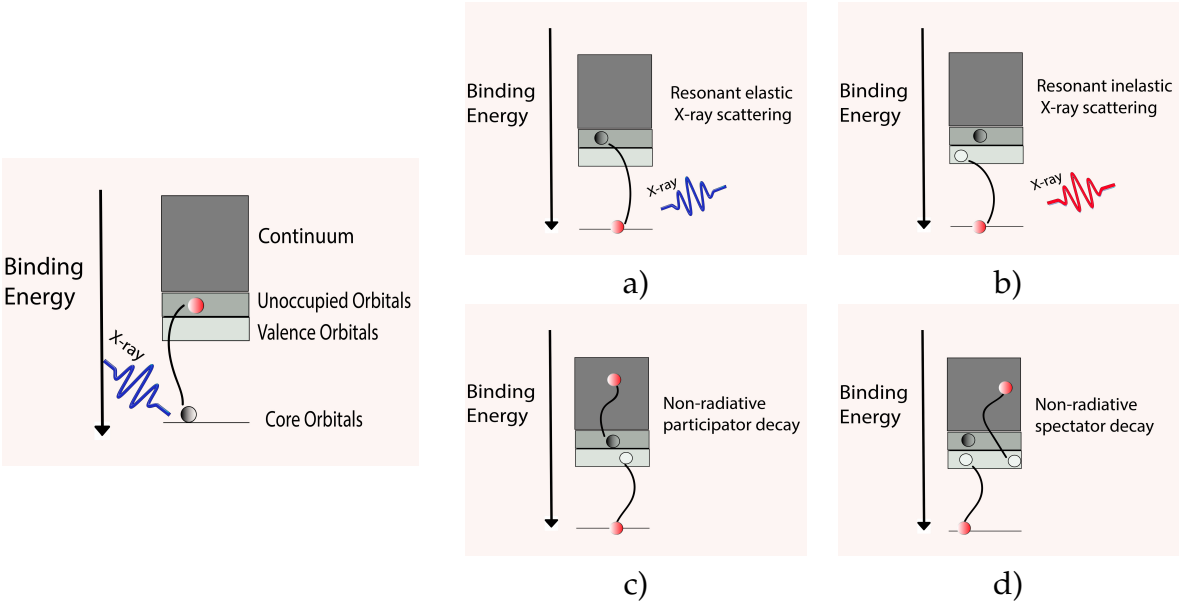

FIGURE 1.7: Different resonant x-ray-matter interaction possible scenarios. Starting from an excitation of the core electron, radiative decay schemes are shown in a) and b), while c) and d) represent ionisation situations or Auger Raman Scattering. The processes have been represented using a schematic form of one electron and three type of levels. This image is based on the concepts in [81].

1.5.2 Non-resonant X-ray matter interactions

Non-resonant scattering is dominant away from absorption edges [81]. These interactions are governed by the second term in the interaction Hamiltonian, $\hat{A}^2$ [82]. In the absence of resonant interactions, non-resonant X-ray scattering is the dominant process. As it is a two-photon process, the treatment of $\hat{p} \cdot \hat{A}$ requires second-order perturbation theory while $\hat{A}^2$ corresponds to first order [83].

Elastic scattering occurs when there is no change in the electronic structure of the sample, but an interaction of the X-ray with the electron density

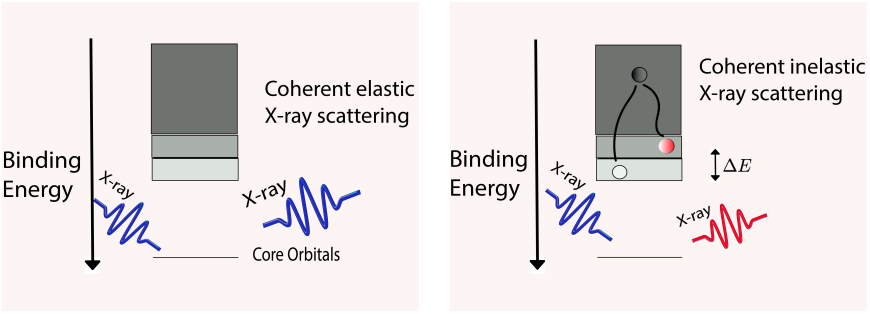

FIGURE 1.8: Non-resonant X-ray scattering interactions with matter. a) Elastic case b) Inelastic non-resonant scattering . Note that Inelastic non-resonant scattering can also involve an excitation into the continuum.

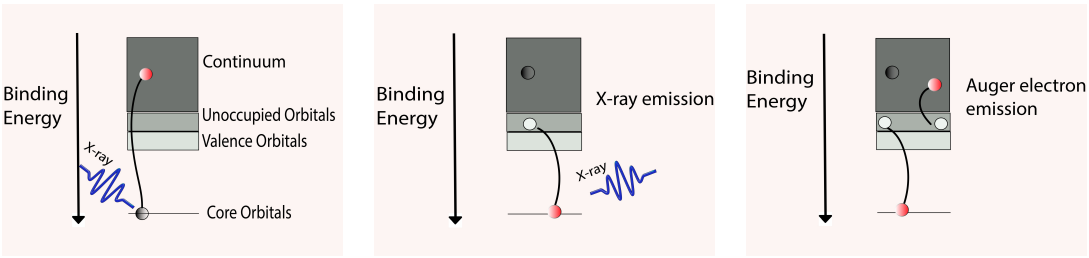

FIGURE 1.9: Non-resonant X-ray-matter interactions for processes not involving scattering. a) Excitation of a core-electron to continuum followed by b) radiative decay or c) Auger decay.

takes place [84]. Likewise, an analogous interaction can happen when a valence electron is excited during the process producing the so-called inelastic scattering (see Fig. 1.8) [3]. It is important to note that inelastic scattering can also result in ionisation. The focus of this thesis is on elastic and inelastic scattering.

Although the dominant non-resonant process is scattering, absorption of a photon can occur, exciting a core-electron into the continuum. The excitation of an inner-shell electron produces, as in the resonant case, a high-energy core-hole. This excitation is then followed by a reordering of the electrons either radiatively or by emission of Auger electrons as shown in Fig. 1.9.

1.6 Predicting X-ray Scattering

1.6.1 Overview

When an X-ray photon is scattered by an atom or molecule, the scattering cross-section of the process will be related to the change in the momentum of the X-ray photon and the quantum states of the atom or molecule. The differential cross section is directly related with the interaction Hamiltonian in Eq. (1.2). After considering a probabilistic treatment and applying Fermi's golden rule, the expression for the differential scattering cross section reads,

$$\frac{dI}{d\Omega} = \left(\frac{dI}{d\Omega}\right)_{\text{Th}} \sum_n \left(\frac{\omega_n}{\omega_0}\right)^2 |\langle \Psi_n | \sum_{j=1}^{N_{el}} e^{i\vec{q}\vec{r}_j} |\Psi_0\rangle|^2, \tag{1.3}$$

where $\left(\frac{dI}{d\Omega}\right)_{\text{Th}}$ is the Thomson cross section for an isolated electron, Ψ_0 and Ψ_n are the initial and final states of the atom or molecule respectively, ω_0 and ω_n are the angular X-ray frequencies of the incident and scattered X-rays and $\vec{q}$ is the scattering vector. According to the Waller-Hartree approximation the energy of the incident X-ray is approximately equal to the energy of the scattered X-ray, allowing us to set $\frac{\omega_n}{\omega_0}$ to unity. Using the closure relation of the wavefunction, we can express it as,

$$\frac{dI}{d\Omega} = \left(\frac{dI}{d\Omega}\right)_{\text{Th}} |\langle \Psi_0 | \sum_{i,j=1}^{N_{el}} e^{i\vec{q}(\vec{r}_i - \vec{r}_j} |\Psi_0\rangle|, \tag{1.4}$$

where the differential cross-section only depends on the ground state wavefunctions and the relative position vector $\vec{r}_i - \vec{r}_j$. This constitutes an approximation of the total scattering differential cross-section based on the pair-correlation function for the ground state,

$$\frac{dI}{d\Omega} = \int P(\vec{r}) \frac{\sin \vec{q}\vec{r}}{\vec{q}\vec{r}} d^3r + N, \tag{1.5}$$

where,

$$P(\vec{r}) = \sum_i \sum_{j \neq i} \int \Psi_0^* \Psi_0 \frac{d\tau_1 .. d\tau_n}{d^3 r_{ij}}. \tag{1.6}$$

The total differential cross section calculated above is formed by elastic and inelastic contributions collected through the term $\vec{r}_i - \vec{r}_j$, which is a two-electron operator. To obtain the ground state, Ψ_0, elastic differential cross section one can isolate $n = 0$ contributions from Eq. (1.3),

$$F(\vec{q}) = \frac{dI}{d\Omega} = \left(\frac{dI}{d\Omega}\right)_{\text{Th}} |\langle\Psi_0| \sum_{j=1}^{N_{el}} e^{i\vec{q}\vec{r}_j} |\Psi_0\rangle|^2, \tag{1.7}$$

where we notice the inclusion of a one-electron operator, $\vec{r}_i$. Using the previous expression one can isolate the contribution of the inelastic interactions to the total scattering cross section, $S(\vec{q})$,

$$S(\vec{q}) = I_{total}(\vec{q}) - F(\vec{q}). \tag{1.8}$$

In the following, we will explain the approaches used to calculate these quantities using theoretical methods. We will also introduce new computational procedures to treat the problem from a different perspective.

1.6.2 Independent Atom Model

In 1915 Debye proposed a method to calculate scattering cross-sections [47]. According to his procedure, one can tabulate the form-factors for all atoms and then combine them to obtain any molecular result. The tabulated atomic form factors are included in the *International Tables of Crystallography* [85], and their calculation is based on the assumption,

$$f_0(\vec{q}) = \int \rho^{el}(\vec{r}) e^{i\vec{q}\vec{r}} d^3r, \tag{1.9}$$

where $\rho^{el}(\vec{r})$ is the atomic electron density. These factors are obtained using Hartree-Fock wavefunctions for every atom in the periodic table [86–88]. Depending on the number of electrons in the system one can use different approaches to perform the calculation. To combine the tabulated atomic form-factors, we can use two approaches; the first one considers that the molecule under study is aligned in space, that is, the signal will be different depending on what is the direction of the X-ray beam. The second one

interprets the signal as a rotational averaged entity considering all possible orientations of the molecule.

Within the first approximation, the system is considered to be aligned and the atomic form factors will be then sum multiplied by a distance phase,

$$f_{mol} = \sum_{i}^{N_{at}} f_i(\vec{q}) e^{i\vec{q}\vec{r}_i}. \tag{1.10}$$

The isotropy of atoms, in which $\vec{q} = |q|$, will help for this purpose as we will not have any difference in the signal depending on symmetry or orientation. If we consider a full elastic signal, the intensity recorded by the detector will be proportional to the square of the form factor. This situation produces a formula that not only depends on the diagonal terms,

$$I(\vec{q}) \propto |f(\vec{q})|^2 = \sum_{i}^{N_{at}} |f_i(\vec{q})|^2 + 2\sum_{j>i}^{N_{at}} f_i(\vec{q}) f_j(\vec{q}) e^{i\vec{q}(\vec{r}_i - \vec{r}_j)}. \tag{1.11}$$

Unfortunately, the alignment of the systems usually requires further treatments of the sample, and for this reason is not the typical situation. Molecules, as an effect of temperature, are encountered of in all possible orientations when the experiment is performed, leading to a rotational averaged signal.

One can show that the element $e^{i\vec{q}(\vec{r}_i - \vec{r}_j)}$ is equal to $e^{i\vec{q}\vec{r}_{ij}\cos(\theta)}$ and the angles for the integration will go from $[0, \pi]$ and $[0, 2\pi]$ as shown in figure 1.10. According to these integration limits, the rotationally-averaged signal can be calculated through the angular integrals of the original aligned signal,

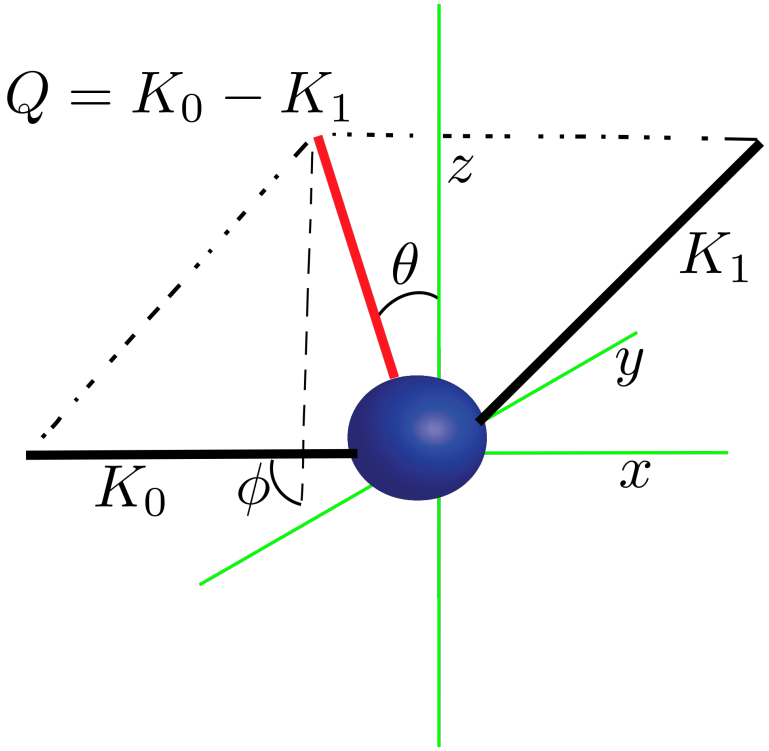

FIGURE 1.10: Graphical definition of the momentum transfer vector Q when the K_0 direction is parallel to the x-axis. K_0 and K_1 are the incoming and scattered vectors respectively. θ and ϕ represent the projection angles for the vector.

$$\int_0^{2\pi}\int_0^{\pi} f_i f_j e^{i\vec{q}\vec{r}_{ij}\cos(\theta)} d\phi d\theta = \tag{1.12}$$

$$2\pi \int_0^{\pi} f_i f_j e^{i\vec{q}\vec{r}_{ij}\cos(\theta)} d\theta = \tag{1.13}$$

$$2\pi f_i f_j \left(\frac{-1}{i\vec{q}\vec{r}_{ij}}\right)\left(e^{-i\vec{q}\vec{r}_{ij}} - e^{i\vec{q}\vec{r}_{ij}}\right) = \tag{1.14}$$

$$4\pi f_i f_j \frac{sin(\vec{q}\vec{r}_{ij})}{\vec{q}\vec{r}_{ij}}, \tag{1.15}$$

hence, the intensity expression will account for the rotational average if we include this relationship,

$$I_{deb} \propto \sum_{i}^{N_{at}} |f_i|^2 + 4\pi \sum_{j>i}^{N_{at}} f_i f_j \frac{sin(\vec{q}\vec{r}_{ij})}{\vec{q}\vec{r}_{ij}}, \tag{1.16}$$

which is the Debye relationship, derived in 1915 [47]. This formula is known as the independent atom model formalism, and it takes into account only the atomic form factors to calculate the molecular signal.

This method is appropriate for qualitative studies of molecular systems in their ground state. If the purpose of this work is a detailed description of the molecule, including its bonds and properties, or excited states study, another method beyond the independent atom model will be required, as discussed in subsequent chapters.

1.7 Computational Chemistry

As discussed in previous sections, the calculation of scattering cross-section is based on the knowledge of the wavefunction of the system. The calculation of time-independent wavefunction relies on the non-relativistic Schrödinger equation,

$$\hat{H}\Psi = E\Psi, \tag{1.17}$$

where $\hat{H}$ is the molecular Hamiltonian and Ψ the corresponding wavefunction. Consider a molecule with n electrons and m nuclei,

$$\hat{H}_{mol} = -\frac{1}{2}\left(\sum_{i}^{n} \nabla_i^2 + \sum_{A}^{m} \nabla_A^2\right) - \sum_{i,A}^{n,m} \frac{Z_A}{\vec{r}_{iA}} + \sum_{i>j}^{n} \frac{1}{\vec{r}_{ij}} + \sum_{A>B}^{m} \frac{Z_A Z_B}{\vec{r}_{AB}}, \tag{1.18}$$

where the lower-case indexes represent the electrons and the upper-case ones the nuclei. We can see that we have kinetic and potential energy terms for both entities and the equation can be rewritten as,

$$\hat{H}_{mol} = \hat{T}_e + \hat{T}_N + \hat{V}(\boldsymbol{R}, \boldsymbol{r}), \tag{1.19}$$

where we have named the kinetic terms as $\hat{T}$, and we have put together all the potential energy contributions as $\hat{V}$. The treatment using the Hamiltonian definition introduced above is problematic because of the crossed terms. This situation leads us to the approximations we will present in the next sections.

1.7.1 Born-Oppenheimer approximation

This approximation aims to separate the nuclear and electronic motion. As nuclei have much higher mass than electrons, the kinetic energy terms for them are negligible in comparison with the electronic ones. If one calculates the limit in which this approximation is valid, the Hamiltonian is modified, accounting only for the kinetic energy term for the electrons [89],

$$\lim_{m_e/M_N \to 0} \hat{H}_{mol} = \hat{H}_\infty = \hat{T}_e + \hat{V}(\boldsymbol{R}, \boldsymbol{r}), \tag{1.20}$$

where m_e is the mass of the electrons and M_N the mass of nuclei. In Eq. 1.20 we use $\hat{H}_\infty$ as the infinite nuclear mass Hamiltonian to denote that nuclei are fixed respectively to the electrons. This assumption allows us to introduce the nuclear degrees of freedom as a parameter on the electronic terms.

For every set of nuclear positions we will have a different solution for the infinite mass Schrödinger equation,

$$\hat{H}_\infty \Psi_j(\boldsymbol{r}; \boldsymbol{R}) = E\Psi_j(\boldsymbol{r}; \boldsymbol{R}), \tag{1.21}$$

regarding this expression one can formulate a decomposition of the total wavefunctions in terms of the different $\boldsymbol{R}$ values. Each value of $\boldsymbol{R}$ will constitute then a complete set,

$$\delta(\boldsymbol{r} - \boldsymbol{r}') = \sum_j \Psi_j(\boldsymbol{r}'; \boldsymbol{R}) \Psi_j^*(\boldsymbol{r}; \boldsymbol{R}). \tag{1.22}$$

Now, we can introduce the ansatz,

$$\Psi(\boldsymbol{r}, \boldsymbol{R}) = \sum_{j=1}^{n} \chi_j(\boldsymbol{R}) \Psi_j(\boldsymbol{r}; \boldsymbol{R}), \tag{1.23}$$

where we have decomposed the wavefunction into a nuclear part $\chi_j(\boldsymbol{R})$ and an electronic part $\Psi_j(\boldsymbol{r};\boldsymbol{R})$ which depends parametrically on the nuclear coordinates. Inserting the previous equation into the full Schrödinger equation gives,

$$(\hat{T}_N + \hat{H}_e)\Psi(\boldsymbol{r},\boldsymbol{R}) = E\Psi(\boldsymbol{r},\boldsymbol{R}), \tag{1.24}$$

which can be expanded as,

$$\left(-\frac{1}{2}\sum_{N}^{n}\nabla_N^2 + \hat{H}_\infty\right)\Psi_j(\boldsymbol{r};\boldsymbol{R})\psi(\boldsymbol{R}) = E\Psi_j(\boldsymbol{r};\boldsymbol{R})\psi(\boldsymbol{R}). \tag{1.25}$$

Multiplying the sides of this equation by the conjugate complex of the electronic wavefunction one can redefine a Schrödinger equation for the nuclear part,

$$\left(-\frac{1}{2}\sum_{N}^{n}\int \Psi_i(\boldsymbol{r};\boldsymbol{R})^*\nabla_N^2\Psi_i(\boldsymbol{r};\boldsymbol{R})d\boldsymbol{r} + E_i(\boldsymbol{R})\right)\psi(\boldsymbol{R}) = E\psi(\boldsymbol{R}). \tag{1.26}$$

This equation only accounts for the diagonal terms in i as a result of the approximation presented above. Although the dependence of the electronic wavefunction on $\boldsymbol{R}$ is just parametric, the ∇_N operator will take a different form on each value, making the situation complicated in terms of calculations.

Their derivatives will be approximately zero or negligible small as a consequence of the nuclei mass. The result of this assumption in solution of the Schrödinger equation is dramatic, allowing one to obtain potential energy surfaces without influence of the electronic coupling,

$$\left(-\frac{1}{2}\sum_{N}^{n}\nabla_N^2 + E_i(\boldsymbol{R})\right)\psi(\boldsymbol{R}) = E\psi(\boldsymbol{R}), \tag{1.27}$$

where $E_i(\boldsymbol{R})$ are the potential energies we are going to use in our treatments. The expansion coefficients, $\psi(\boldsymbol{R})$, can be interpret then as the wavefunctions for nuclei moving on these potential energy surfaces.

This approximation is widely used in quantum mechanics as it simplifies in a great measure the treatment of the time independent Schrödinger equation. However in certain cases one can overpass the limits imposed by it considering the derivative coupling non-zero elements [9, 10].

In the next sections, we will explain what methods have been developed to obtain the electronic structure of molecules and atoms based on the assumptions we have made here.

1.7.2 Electronic structure methods

Approximate wavefunctions can be calculated using computational methods. In the following we will describe these procedures based on the previous lines.

Hartree-Fock

Between 1928 and 1951 Douglas Hartree [90], Vladimir Fock [91] and John Clarke Slater [92] introduced the idea of the self-consistent field (SCF). Along with the molecular orbital theory, the self-consistent field establishes an elegant solution for the electron-electron repulsion terms. Based mainly on the Bohr atomic model it says that each electron will feel an averaged field produced by the rest of particles in the molecule or atom. Also, they postulated the requirement of a linear and antisymmetric combination of spin orbitals to solve the Schrödinger equation through their iterative process. The Hartree product is settled as the first expression to work out this procedure, adding this to the previous assumptions one can construct a complete framework for the solution of the time-independent Schrödinger equation.

The so-called Hartree-Fock method can be seen then as an iterative procedure to obtain a reliable solution of the Schrödinger equation. The central premise is the approximation of the multi-body wavefunction, $\Psi(x_1, x_2, ..., x_n)$, as a Slater determinant,

$$\Psi(x_1, x_2, ..., x_n) = \frac{1}{\sqrt{N!}} \begin{vmatrix} \phi_1(x_1) & \phi_2(x_1) & \phi_3(x_1) & ... & \phi_n(x_1) \\ \phi_1(x_2) & \phi_2(x_2) & \phi_3(x_2) & ... & \phi_n(x_2) \\ \phi_1(x_3) & \phi_2(x_3) & \phi_3(x_3) & ... & \phi_n(x_3) \\ . & . & . & . & . \\ . & . & . & . & . \\ . & . & . & . & . \\ \phi_1(x_n) & \phi_2(x_n) & \phi_3(x_n) & ... & \phi_n(x_n) \end{vmatrix} \quad (1.28)$$

where x_n represent the particle spin and spatial coordinates, n is the number of particles and $\phi(x)$ are single-particle spin-orbitals. The method can be applied to atoms or isolated molecules and it has no restrictions on the number of particles present on the system. To properly solve it one should make use of Rothaan-Hall equations, which expand the problem into a non-orthonormal basis, either Gaussian or Slater-type [93, 94]. It takes a number of approximate orbitals and chooses an electron, considering the rest as an static charge distribution moving around it. The Schrödinger equation is solved for this electron using the orbitals chosen at the beginning, repeating the process for all electrons on the system. As it is an iterative method we will repeat the same steps, calculating a new potential, until energy convergence is reached. The final set of orbitals will constitute the key parameter to obtain the electron density of the molecule or atom under consideration. One can define it as,

$$\rho(\boldsymbol{r}) = \sum_{i}^{N} b_i |\phi_i(\vec{r})|^2, \quad (1.29)$$

where the occupation numbers b can be $[0, 1]$ and $\phi(\vec{r})$ are mono electronic spin-orbitals.

The Hartree-Fock method works well for ground state calculations in systems described well by a single Slater determinant. However, as we explained before, the aim of our project encompasses both ground and excited state calculations, demanding more accuracy in the wavefunction description.

Multiconfigurational Methods

As we stated above, Hartree-Fock method has its limitations. There is an inherent error when this procedure is carried out, and the presence of only one Slater determinant limits the result [95, 96]. To extend the problem and take into account the correlation energy, defined as the error produced by a Hartree-Fock treatment, we can use a Configuration Interaction method. Based on the same ideas as the Hartree-Fock approach, these methods seek a diagonalisation of the N-particle Hamiltonian on the basis of N-electron Slater determinants. Depending on the number of Slater functions used to express each wavefunction one can get closer to the exact energy [96].

The drawback of this method lies in the enormous number of determinants required to study the full system even for a small molecule. However, one can truncate the number of configurations allowed, reducing the problem but constituting a great increase in the accuracy.

The procedure starts by calculating all possible combinations of electrons in spin-orbitals within the molecule, ordering them by the number of excitations from the ground initial state. Each of the wavefunctions produced will combine all possible permutations of electrons. The interaction between singles and the initial state is null as a consequence of Brillouin theorem, as well as all the interactions involving two different spin orbitals. The spin-orbitals used for this calculation are different from the HF ones. Instead, natural orbitals introduced by Löwdin [97] will be the perfect choice for this purpose.

One can consider that a variational principle applied to the HF orbitals when the number of configurations is small enough will reduce the difficulty of the CI treatment. This is the primary idea constituting the multi-configurational self-consistent field (MCSCF) methods , which truncate the full configuration interaction and use N Slater determinants optimised from a Hartree-Fock procedure.

The Complete Active Space Self-Consistent Field (CASSCF) method is an example of multi-configurational procedure based in the self-consistent field approach. A reduced number of orbitals and electrons are chosen to represent the restricted active space. All excitations within a threshold are

considered inside this active space, relying in a definition of the wavefunction of the form,

$$\Psi(\boldsymbol{r}) = \sum_{i=1}^{N_{conf}} c_i \psi_i(\vec{r}), \tag{1.30}$$

where the total wavefunction for a definite state is represented by the sum of several configurations N_{conf}. Each c_i will correspond to a value inside the configuration interaction vector and $\psi_i(\vec{r})$ are the different configurations expressed in terms of Slater determinants. This method is not limited to one-state definitions. The same set of orbitals is optimised to produce state-averaged results, that is, several states will be described using the same configurations and orbitals and the only difference will be the configuration interaction vectors associated with them. CASSCF notation in this thesis will express the level of accuracy we are including in the calculation by specifying the number of electrons and active orbitals used for the calculation, i.e. $\mathrm{CASSCF(N_{el}, N_{orbitals})}$.

One of the main drawbacks of Hartree-Fock is corrected using multiconfigurational procedures such as CASSCF. The correlation energy lacking in the single-determinant description of the wavefunction and the mean field approximation considered in Hartree-Fock procedures can be considered. We can divide the electron correlation in two main contributions, *dynamic* and *static correlation*. When electrons move, they will avoid the instantaneous position of other electrons producing an excess of energy when we consider a self-consistent field. It is called *dynamic correlation* as it depends on electron dynamics. On the other hand, *static correlation* is taken into account when a multi-determinant Slater picture is used to represent the wavefunction.

The results produced by the CASSCF method are reliable in terms of the energy for the different states. This method, using several slater determinants, is capable of correcting the static correlation not considered in Hartree-Fock methods. However, it shows a poor description of dynamical correlation. Only certain approaches such as multi-reference configuration

interaction (MRCI) or complete active space perturbation theory second order (CASPT2) will correct this drawback.

Although still limited by the number of active orbitals chosen in the MCSCF method preceding it, MRCI allows new excitations and therefore achieve better energies than previous procedures. The MRCI method uses by default Configuration State Functions (CSFs) to eliminate the averaged results introduced by the usage of Slater determinants. It takes into account, using a larger frame of possible excitations, the electron correlation not considered by the self-consistent field procedures. Methods such as CASPT2 use second order perturbation theory to solve the Schrödinger equation. CASPT2 uses a reference multiconfigurational result to start the calculation, achieving a level of accuracy greater than other approaches mentioned above. The main problems of CASPT2 are the singularities occasioned when the reference is not accurate enough.

1.7.3 Quantum dynamics

Up until now, we have considered stationary states. However, this is not a realistic picture when we are talking about photochemistry and time-resolved dynamics. To study the evolution of a wavefunction in time we need to use the time-dependent Schrödinger equation,

$$\imath\hbar\frac{d\Psi(\boldsymbol{r},t)}{dt} = \hat{H}\Psi(\boldsymbol{r},t), \tag{1.31}$$

with the time-dependent wavefunction $\Psi(\boldsymbol{r},t)$, in which $\boldsymbol{r}$ represents the electronic and nuclear degrees of freedom and t is the time. There are several ways in which we can solve this equation. Making use of the methods explained before, one can calculate stationary solutions for the time-independent Schrödinger equation and based on the separation of variables, this result can be used to treat it [95].

The problem of this treatment relies on the impossibility to find a general solution for the time-dependent equation. A coherent combination of eigenfunctions can be obtained as the valid result. To do so, we need to get a set of orthonormal basis functions that satisfy the conditions specified

by the Schrödinger equation; this procedure can be straightforward if we have only one nuclear degree of freedom in our wavefunction and the time dependency of the Hamiltonian is not explicit. As we will explain in the theory chapter the application of different pictures, such as Heisenberg [98] and Interaction [99] pictures, may help in the treatment of the time-dependent problems but in the presence of a multi-dimensional wavefunction, a discretisation using grid-based methods will be necessary [100].

Quasi-exact solutions of this equation can be achieved using different numerical methods. One should discretise the operators and wavefunctions to start the treatment. For analytically defined wavefunctions, the procedure is straightforward, and we can use an equally spaced grid to express it. However, most of the methods make use of non-equidistant points to define the grid (Discrete Variable Representation) gaining the advantage of better sampling of the wavefunction in the regions of interest, and the wavefunction is constructed using Gaussian wave packets. The initial guess needs to be a solution of the electronic and vibrational Hamiltonian, requiring further treatments of the nuclear degrees of freedom to achieve the final time-dependent solution [101].

Once we have the variables discretised, several procedures can be applied. From the historical second order differentiation (SOD) to the modern Fourier transformation methods (i.e. split-operator method) a vast range of possibilities are available to carry out the simulation [100, 101]. One should think about the scalability of the problem with the degrees of freedom. That is, this kind of treatments require a reduced dimensionality to be applied and are limited to molecules with a few atoms.

When the number of degrees of freedom in the system is too large to apply these methods, one can use other kinds of approaches to solve the TDSE. The Multi-configurational Hartree method (MCTDH) [102], which treats the nuclear and electronic degrees of freedom from a quantum perspective using pre-calculated potential energy surfaces (PECs), is one the procedures available to solve the TDSE, but a full range of similar methods exist. It is worth stressing that on-the-fly *ab-initio* calculations can be included in the TDSE solution to dramatically reduce the computational time

required to carry out the simulations. The Multi-configurational Ehrenfest method (MCE) [103] or *ab-initio* multiple spawning (AIMS) [104], which are considered semi-quantum, and surface hopping with arbitrary couplings (SHARC) [105] that presents a classical treatment of the nuclear movement combined with quantum coupling between different potential energy surfaces, represent essential examples of such approaches.

1.8 Overview of thesis

In Ch. 2 we provide a summary and some new developments of the theory of X-ray scattering. In Ch. 3 we look at elastic X-ray scattering from state-selected molecules. In Ch. 4 we present a new computational method for calculating elastic and inelastic X-ray scattering matrix elements. Finally in Chapters 5 and 6 we examine time-resolved X-ray scattering from non-stationary states in the H-atom and the H_2 molecule respectively.

The main theoretical considerations of X-ray scattering are discussed in Ch. 2 but a review of the most important features is included at the beginning of each Chapter, enunciating the points necessary to understand the results presented.

Chapter 2

Theory

2.1 Introduction

In the following Chapter we treat the theory of X-ray scattering starting from a quantized electromagnetic field. We derive the differential cross-section for stationary scattering, and treat the scattering from non-stationary superposition of quantum states, i.e. wavepackets. The treatment is based on the three following sources [77, 83, 106], with novel developments and discussion contained in Secs. 2.6 and 2.7.

2.2 Electromagnetic fields: Classical to Quantized

The electromagnetic field can be described using Maxwell's equations. These expressions explain the effect of the electric, $\vec{E}(\vec{r},t)$, and magnetic fields, $\vec{B}(\vec{r},t)$, on a charge distribution, ρ, and the current vector, $\vec{J}$,

$$\nabla \cdot \vec{E}(\vec{r},t) = \rho/\epsilon_0 \tag{2.1}$$

$$\nabla \cdot \vec{B}(\vec{r},t) = 0 \tag{2.2}$$

$$\nabla \times \vec{E}(\vec{r},t) = -\frac{\partial \vec{B}(\vec{r},t)}{\partial t} \tag{2.3}$$

$$\nabla \times \vec{B}(\vec{r},t) = \mu_0 \vec{J} + \mu_0 \epsilon_0 \frac{\partial \vec{E}(\vec{r},t)}{\partial t}, \tag{2.4}$$

where μ_0 and ϵ_0 are the permeability and permitivity in vacuum. Another important expression related to Maxwell's equations is the Lorentz force

that acts on the particle,

$$\vec{F} = q(\vec{E}(\vec{r},t) + \dot{\vec{r}} \times \vec{B}(\vec{r},t)), \tag{2.5}$$

representing the force acting on a particle of charge q and position $\vec{r}$ (with $\dot{\vec{r}}$ as the velocity) , in the presence of electric and magnetic fields $\vec{E}(\vec{r},t)$ and $\vec{B}(\vec{r},t)$.

The description of the electromagnetic field in terms of vector potential, $\vec{A}(\vec{r},t)$, and scalar potential, $\phi(\vec{r},t)$, simplifies the treatment greatly,

$$\vec{B}(\vec{r},t) = \nabla \times \vec{A}(\vec{r},t) \tag{2.6}$$

$$\nabla^2\phi(\vec{r},t) + \frac{\partial}{\partial t}(\nabla \cdot \vec{A}(\vec{r},t)) = -\rho/\epsilon_0 \tag{2.7}$$

$$\left(\nabla^2\vec{A}(\vec{r},t) - \mu_0\epsilon_0\frac{\partial^2\vec{A}(\vec{r},t)}{\partial t^2}\right) - \nabla\left(\nabla \cdot \vec{A}(\vec{r},t) + \mu_0\epsilon_0\frac{\partial\phi(\vec{r},t)}{\partial t}\right) = -\mu_0\vec{J}, \tag{2.8}$$

this simplification can be extended by using a gauge transformation of the form,

$$\vec{A}(\vec{r},t) \to \vec{A}'(\vec{r},t) = \vec{A}(\vec{r},t) + \Delta\vec{\Lambda} \tag{2.9}$$

$$\Phi(\vec{r},t) \to \Phi'(\vec{r},t) = \Phi(\vec{r},t) - \frac{d\vec{\Lambda}}{dt}, \tag{2.10}$$

where $\Delta\vec{\Lambda}$ is a vectorial parameter with a restricted value.If we decide that,

$$\nabla^2\vec{\Lambda} = -\nabla \cdot \vec{A}(\vec{r},t), \tag{2.11}$$

known as the Coulomb, or transverse gauge. It follows that Maxwell's equations can be rewritten as,

$$\nabla \cdot \vec{A}'(\vec{r},t) = 0 \tag{2.12}$$

$$\nabla^2\phi'(\vec{r},t) = -\rho/\epsilon_0 \tag{2.13}$$

$$\nabla^2\vec{A}'(\vec{r},t) - \mu_0\epsilon_0\frac{\partial^2\vec{A}'(\vec{r},t)}{\partial t} = -\mu_0\vec{J} + \mu_0\epsilon_0\nabla\frac{\partial\phi'(\vec{r},t)}{\partial t}, \tag{2.14}$$

where $\vec{A}(\vec{r},t) = \vec{A}_T(\vec{r},t)$ as $\nabla \cdot \vec{A}(\vec{r},t) = 0$. This condition is fulfilled automatically when the Coulomb gauge is applied and allows a decomposition of the vector potential, $\vec{A}'(\vec{r},t)$, as a sum of normal modes. As $\vec{A}(\vec{r},t)$ is a periodic function which can be constrained to a finite volume, V, we can express it as a sum of normal modes using harmonic functions or plane-waves,

$$\vec{A}(\vec{r},t) = \sum_{\vec{k}} \vec{A}_{\vec{k}}(t) e^{i\vec{k}\vec{r}}, \tag{2.15}$$

where $\vec{k}$ is a wave vector that characterises each wave and $\vec{A}_{\vec{k}}(t)$ can be calculated using the field equation to give a general solution of the form,

$$\vec{A}_{\vec{k}}(t) = \vec{c}_{\vec{k}}(t) + \vec{c}_{-\vec{k}}(t), \tag{2.16}$$

with a dispersion relation,

$$\omega_{\vec{k}} = c\vec{k}. \tag{2.17}$$

From these equations one can derive the orthogonality of the vector $\vec{k}$ with the direction of the propagation of the field, $\vec{k} \cdot \vec{A}(\vec{r},t) = 0$. This relationship leads to the definition of the polarization vectors, $\vec{e}_{\vec{k}}$, which represent the direction of the field and fulfill the orthogonality relation with the wave vector,

$$c_{\vec{k}}(t) = \sum_{\sigma=1}^{2} c_{\vec{k}\sigma}(t)\vec{e}_{\vec{k}\sigma} = \sum_{\sigma} c_{\vec{k}\sigma}(0) e^{-i\omega_{\vec{k}}t}\vec{e}_{\vec{k}\sigma}, \tag{2.18}$$

if we consider that $V \to \infty$.

The previous relationships and their analogues for the expansion of $\vec{E}(\vec{r},t)$ and $\vec{B}(\vec{r},t)$ in plane-waves can be used to redefine the Hamiltonian of the radiation field. Generally it can be written as,

$$H = \frac{1}{2}\int [\epsilon_0 \vec{E}_T^2(\vec{r},t) + \frac{1}{\mu_0}\vec{B}^2(\vec{r},t)] d^3r, \tag{2.19}$$

which can be expressed as,

$$H = \sum_{\sigma=1,2} \sum_{\vec{k}} H_{k\sigma} = \sum_{\sigma=1,2} \sum_{\vec{k}} 2L^3 \epsilon_0 \omega_{\vec{k}} \vec{c}_{\vec{k}\sigma} \vec{c}_{-\vec{k}\sigma} \tag{2.20}$$

where the total radiation Hamiltonian is a sum of different modes with wave vector $\vec{k}$ and σ polarization including the definition of $\vec{A}(\vec{r}, t)$. The canonical operators for position, $\hat{Q}_{\vec{k}\sigma}$, and momenta, $\hat{P}_{\vec{k}\sigma}$, expressed in terms of the field coefficients $\vec{c}_{\vec{k}\sigma}$, can be used to formulate a quantum description of the Hamiltonian, analogous to the classical picture,

$$\hat{H} = \sum_{\vec{k}} \sum_{\sigma=1,2} \hat{H}_{\vec{k}\sigma} = \frac{1}{2}(\hat{P}^2_{\vec{k}\sigma} + \omega^2_{\vec{k}} \hat{Q}_{\vec{k}\sigma}). \tag{2.21}$$

The creation and annihilation operators, $\hat{a}$ and $\hat{a}^\dagger$, which are used to express a change in the field modes are directly related with the canonical formulation of the radiation Hamiltonian,

$$\hat{a}_{\vec{k}\sigma} = \frac{1}{\sqrt{2\hbar\omega_{\vec{k}}}}(\omega_{\vec{k}} \hat{Q}_{\vec{k}\sigma} + \imath \hat{P}_{\vec{k}\sigma}) \tag{2.22}$$

$$\hat{a^\dagger_{\sigma}} k = \frac{1}{\sqrt{2\hbar\omega_{\vec{k}}}}(\omega_{\vec{k}} \hat{Q}^2_{\vec{k}\sigma} - \imath \hat{P}_{\vec{k}\sigma}), \tag{2.23}$$

that directly comes from the solution of the system of coupled differential equations for position and momenta. Each mode of the Hamiltonian may then be described as,

$$\hat{H}_{\vec{k}\sigma} = (\hat{N}_{\vec{k}\sigma} + \frac{1}{2})\hbar\omega_{\vec{k}}, \tag{2.24}$$

where,

$$\hat{N}_{\vec{k}\sigma} = \hat{a}_{\vec{k}\sigma} \hat{a}^\dagger_{\vec{k}\sigma}, \tag{2.25}$$

which preserves the Hermitian character of the operator and is an observable. The sum of different normal modes will form the total radiation Hamiltonian,

$$\hat{H}_R = \sum_{\vec{k}} \sum_{\sigma=1,2} \hbar\omega_{\vec{k}} (\hat{a}^\dagger_{\vec{k}\sigma} \hat{a}_{\vec{k}\sigma} + \frac{1}{2}). \tag{2.26}$$

From this expression we can derive the definition of the vector potential operator, $\hat{A}(\vec{r},t)$, that is analogous to the classical treatment but includes the annihilation and creation operators,

$$\hat{A}(\vec{r},t) = \sum_{\sigma}\sum_{\vec{k}} \sqrt{\frac{\hbar}{2\epsilon_0 L^3 \omega_{\vec{k}}}} \left(\epsilon_\sigma \hat{a}_{\sigma\vec{k}} e^{\imath(\vec{k}\cdot\vec{r}-\omega_{\vec{k}}t)} + \epsilon_\sigma^* \hat{a}^\dagger_{\sigma\vec{k}} e^{-\imath(\vec{k}\cdot\vec{r}-\omega_{\vec{k}}t)} \right). \tag{2.27}$$

This expression will be useful for the description of the interaction of the electromagnetic field and the material system.

The eigenfunctions of the radiation Hamiltonian define the radiation field and are necessary to calculate its interactions. The eigenfunctions form a complete set of eigenvectors which contain information about the normal modes of the electromagnetic field under consideration. Fock states fulfill these premises,

$$\hat{N}_{\vec{k}\sigma}|n_{\vec{k}\sigma}\rangle = n_{\vec{k}\sigma}|n_{\vec{k}\sigma}\rangle \tag{2.28}$$

$$\hat{H}_{\vec{k}\sigma}|n_{\vec{k}\sigma}\rangle = (n_{\vec{k}\sigma} + \frac{1}{2})\hbar\omega_{\vec{k}}|n_{\vec{k}\sigma}\rangle. \tag{2.29}$$

These vectors represent a complete Hilbert space, and can be coherently combined to represent a multi-modal electromagnetic field. The complete eigenvector set will also be an eigenstate of the radiation Hamiltonian, $\hat{H}_R$,

$$\hat{H}_R|\{n_{\vec{k}\sigma}\}\rangle = \sum_{\vec{k}\sigma} \hbar\omega_{\vec{k}}(n_{\vec{k}\sigma} + \frac{1}{2})|\{n_{\vec{k}\sigma}\}\rangle. \tag{2.30}$$

The quantization of the electromagnetic field is important for the current description of scattering from non-stationary states. In the following we will discuss the combination of the expressions developed above with the description of matter to formulate the Hamiltonian for the radiation-matter (light-matter) interaction.

2.3 Interaction Hamiltonian

Once the field Hamiltonian, $\hat{H}_R$, and the vector potential operator, $\hat{A}(\vec{r},t)$, are quantized we can postulate an interaction picture. The influence of the radiation field on a charged particle can be considered as classical,

$$\hat{p} \rightarrow \hat{p} - q\hat{A}(\vec{r},t), \tag{2.31}$$

then, the kinetic part of the Hamiltonian will read,

$$\hat{H}_{kin} = \sum_{i=1}^{N} \frac{1}{2m_i}(\hat{p}_i^2 - 2\hat{p}q_i\hat{A}_i(\vec{r},t) + q_i^2\hat{A}_i^2(\vec{r},t)), \tag{2.32}$$

where N will be the number of particles in the system, m_i the mass of particle i and q_i its charge. As $\hat{p}^2$ only affects the material system and has no field presence we can divide Eq. (2.32) into separate parts for the material system and the interaction terms. Including the basic potential Hamiltonian for each part of the equation we have,

$$\hat{H}_{matter} = \hat{H}_{kin,matter} + \hat{H}_{Coulomb} = \sum_{i=1}^{N} \frac{1}{2m_i}\hat{p}_i^2 + \frac{1}{2}\sum_{i\neq j}^{N} \frac{1}{4\pi\epsilon_0}\frac{q_iq_j}{|\vec{r}_i - \vec{r}_j|} \tag{2.33}$$

$$\hat{H}_{int} = \hat{H}_{kin,int} + \hat{H}_{spin} = -\sum_{i=1}^{N} \frac{q_i}{m_i}(\hat{A}(\vec{r},t)\hat{p} - \mu_i\hat{B}_i(\vec{r},t)) + \sum_{i=1}^{N} \frac{q_i}{2m_i}\hat{A}^2(\vec{r},t), \tag{2.34}$$

where Eq. (2.34) has been reordered to isolate the terms contributing to light absorption or scattering. Separating the terms according to the order of the vector potential operator. Involving only one-mode transitions, the first set of terms will explain those processes which, as in the case of absorption or emission, require resonant interactions between the X-ray and the material system. Conversely, squared field terms will be the key to study processes involving two modal excitations like non-resonant scattering. Based on this, we will name the parts of the interaction Hamiltonian separately,

$$\hat{H}_{int} = \hat{H}_1 + \hat{H}_2, \tag{2.35}$$

where $\hat{H}_1$ contains the terms depending on $\hat{A}(\vec{r},t)$ and $\hat{H}_2$ those with $\hat{A}(\vec{r},t)^2$ dependence.

2.4 Scattering expression

When the energy of the X-ray is sufficiently large, scattering is the predominant process resulting from radiation-matter interaction. Since two photons are involved in the process, this requires the use of a squared field term, represented through the $\hat{A}^2(\vec{r},t)$ operator. Therefore, only $\hat{H}_2$ will be used to represent the interaction Hamiltonian because this gives scattering in first order time-dependent perturbation theory. Using the second part of the interaction Hamiltonian inside the frame of Kramers-Heisenberg formalism, we will calculate the scattering cross-section.

A scattering process involves an initial and a final state of the photons and for the material system. We can calculate the transition probability using Fermi's golden rule. If we define the initial and final states as,

$$|i\rangle = |\Psi_0^{N_{el}}\rangle|N_{EM}\rangle \tag{2.36}$$

$$|f\rangle = |\Psi_f^{N_{el}}\rangle\hat{a}_{\vec{k}\sigma}\hat{a}^{\dagger}_{\vec{k}\sigma}|N_{EM}\rangle, \tag{2.37}$$

where $|\Psi^{N_{el}}\rangle$ represents the material system and $|N_{EM}\rangle$ represents the Fock state of the photon, the amplitude of a transition between $|i\rangle$ and $|f\rangle$ will be,

$$\begin{aligned} S_{fi} &= \lim_{t\to\infty}\langle f|\Psi\rangle = \\ &= -2\pi i\delta(E_f - E_i - \hbar\omega_{if}) \times \left(\langle f|\hat{H}_{int}|i\rangle + \sum_m \frac{\langle f|\hat{H}_{int}|m\rangle\langle m|\hat{H}_{int}|i\rangle}{E_i - E_m + \imath\epsilon} + ...\right), \end{aligned} \tag{2.38}$$

where we have introduced Fermi's golden rule describing the transition amplitude as the projection of the final state on the total wave function at infinite time. The rate for the transition will be the amplitude, S_{fi}, divided by

the period of the transition,

$$\Gamma_{fi} = \frac{\mid S_{fi} \mid^2}{T} = \\ = 2\pi\delta(E_f - E_i - \hbar\omega_{if}) \left| \langle f|\hat{H}_{int}|i\rangle + \sum_m \frac{\langle f|\hat{H}_{int}|m\rangle\langle m|\hat{H}_{int}|i\rangle}{E_i - E_m + \imath\epsilon} + ... \right|^2 . \tag{2.39}$$

The expression above gives the transition probability between $|i\rangle$ and $|f\rangle$ [80]. The transition probability divided by the density of states, $g(E_f)$, and the photon flux for the i^{th} mode, Φ_i, will give us the differential cross section of the process. The density of states in the electromagnetic field can be obtained considering the number of modes in a solid angle differential element $d\Omega$,

$$g(E_f) = \left(\frac{L}{2\pi c}\right)^3 \frac{\omega^2}{\hbar} d\Omega dE, \tag{2.40}$$

where L is the length of the confined volume, c the speed of light, ω the angular frequency and $d\Omega$ the solid angle element, $d\Omega$. The flux of photons, Φ_i, considering that the volume is infinite and $L \to \infty$, is defined by the flux in a transition between continuous states, that involves only one photon,

$$\Phi_i = \frac{cn_i}{L^3}, \tag{2.41}$$

where n_i is the number of photons in the i mode and L^3 is the volume element.

Dividing the transition probability in Eq. (2.39) by the density of states in Eq. (2.40) and the photon flux in Eq. (2.41), gives the scattering differential cross-section as,

$$\frac{d^2\sigma}{d\Omega d\hbar\omega_f} = \left(\frac{\omega_f}{\omega_i}\right) r_0^2 \left|\vec{e}_i \cdot \vec{e}_f\right|^2 \sum_{if} \sum_{jj'} g_B^i \langle i|\hat{L}_j|f\rangle\langle f|\hat{L}_{j'}|i\rangle \delta(E_i - E_f + \hbar\omega), \tag{2.42}$$

where,

$$\hat{L}_j = \sum_i^{N_{el}} e^{\imath\vec{q}\vec{r}_i}, \tag{2.43}$$

where we sum over all electrons in the system, N_{el}. g_B^i is the Boltzmann factor for state i, accounting for the thermal distribution across initial states. The subindexes i, j, f represent the different iterated states, r_0 the Bohr radius and E_i and E_f are the eigenvalues of $|i\rangle$ and $|f\rangle$. As the magnitude of the X-ray-particle interaction is inversely proportional to the mass of the particle, as can be inferred from $\frac{q_i}{2m_i}$ terms in Eq. (2.32), we have neglected the interaction of X-rays with nuclei due to their large mass compared to electrons.

Eq. (2.42) describes a single scattering event, and is thus constrained to the first Born approximation. It also includes the interaction between a photon and a free electron which is initially at rest. This quantity corresponds to the well-known Thomson cross section and is only valid if the electrons are treated non-relativistically,

$$\left(\frac{d\sigma}{d\Omega}\right)_{\text{Th}} = \left(\frac{\omega_f}{\omega_i}\right) r_0^2 \left|\vec{e}_i \cdot \vec{e}_f\right|^2, \tag{2.44}$$

including the definition of the photon-electron interaction inside the scattering equation provides a compact expression for the differential scattering cross section,

$$\frac{d\sigma}{d\Omega d\hbar\omega_f} = \left(\frac{d\sigma}{d\Omega}\right)_{\text{Th}} \sum_{if} \sum_{jj'} g_B^i \langle i|L_j|f\rangle \langle f|L_{j'}|i\rangle \delta(E_i - E_f + \hbar\omega). \tag{2.45}$$

The equation above represents scattering from stationary states and it can be simplified considering $g_B^i \langle i|L_j|f\rangle \langle f|L_{j'}|i\rangle \delta(E_i - E_f + \hbar\omega)$, as the dynamic structure-factor, $s(\vec{q}, \omega)$.

We will later consider scattering from non-stationary quantum superposition of states interacting with coherent radiation.

2.5 Elastic and inelastic non-resonant scattering

The expression for scattering from a set of stationary states provided by Eq. (2.45) shows the complete X-ray scattering differential cross section for an

atom or a molecule. It also allows to isolate terms corresponding to elastic and inelastic scattering as discussed in Ch. 1. If the energy of the X-ray remains unchanged after the interaction, we consider this as an elastic scattering event, simplifying the equation dramatically.

Elastic scattering matrix elements are diagonal, they leave the initial state i intact,

$$L_{if} = \langle i|\hat{L}|f\rangle\delta_{if}. \tag{2.46}$$

eliminating from Eq. (2.45) all contributions due to inelastic processes,

$$\frac{d^2\sigma}{d\Omega\hbar d\omega_f} = \left(\frac{d\sigma}{d\Omega}\right)_{\text{Th}} \left|\langle i|\sum_j^{N_{el}} e^{\imath\vec{q}\vec{r}_j}|i\rangle\right|^2, \tag{2.47}$$

where the squared bracket will represent the so-called elastic form factor , $F(\vec{q})$, which can be shown to be equivalent to a Fourier Transformation of the electron density,

$$F(\vec{q}) = \langle i|\sum_j^{N_{el}} e^{\imath\vec{q}\vec{r}_j}|i\rangle = \int \phi_i(\boldsymbol{r})^*\phi_i(\boldsymbol{r})e^{\imath\vec{q}\boldsymbol{r}}d\boldsymbol{r} = \int d^3r\rho^{(el)}(\vec{r})e^{\imath\vec{q}\vec{r}}, \tag{2.48}$$

Eq. (2.48) is useful to calculate differential scattering cross sections using *ab-initio* methods, as the electron density is directly related to the electronic wave function.

Elastic scattering has been widely exploited to characterise matter. Starting from the total scattering definition introduced in Ch. 1,

$$\frac{dI}{d\Omega} = \left(\frac{dI}{d\Omega}\right)_{\text{Th}} |\langle\Psi_0|\sum_{i,j=1}^{N_{el}} e^{\imath\vec{q}(\vec{r}_i-\vec{r}_j)}|\Psi_0\rangle|, \tag{2.49}$$

the calculation of inelastic scattering can be calculated as a contribution to it. Using the elastic scattering expression in Eq. (2.48), and subtracting it from the value of the total differential cross section in Eq. (2.49 the contribution of inelastic scattering can be obtained,

$$S_{inelastic}(\vec{q}) = I_{total}(\vec{q}) - F_{elastic}(\vec{q}). \tag{2.50}$$

However we aim to isolate the inelastic scattering contributions corresponding to certain transitions in the material system. We will make use of particular cases on Eq. (2.45) of the form,

$$\langle i| \sum_{j}^{N_{el}} e^{i\vec{q}\vec{r}_j} |j\rangle = \int \phi_i(\boldsymbol{r})^* \phi_j(\boldsymbol{r}) e^{i\vec{q}\boldsymbol{r}} d\boldsymbol{r}, \tag{2.51}$$

which considers $i \neq j$. Although the electron density, $\rho^{(el)}(\vec{r})$, cannot be used in this case, inelastic scattering will be related to the Fourier Transformation of the transition between the states ϕ_i and ϕ_j.

2.6 Non-stationary X-ray scattering

Up to this point, we have developed a treatment that considers only stationary states. What happens if we consider a non-stationary superposition of quantum states i.e. a wavepacket, such as excited by a burst of coherent light? How will this interact with a coherent X-ray pulse?

Considering that the time-dependent wave function is perturbed by the X-ray probe at time t', the effect can be approximated using first order time-dependent perturbation theory,

$$|\Phi(t)^{(1)}\rangle = -\frac{\imath}{\hbar} \int_0^t dt' \hat{U}(t,t') O(t') \hat{U}(t,0) |\Phi(0)\rangle, \tag{2.52}$$

where the time dependent operator depends only on the system time independent unperturbed Hamiltonian and the $\vec{r}$ dependence of $\Phi(t)$ its not explicitly shown,

$$\hat{U}(t,t') = e^{-\imath H_M (t-t')/\hbar}, \tag{2.53}$$

and the perturbation is defined as,

$$O(t) = \langle \Psi_{\sigma_s \vec{k}_s} | \hat{H}_{int}(t) | \Psi_{\sigma_0 \vec{k}_0} \rangle. \tag{2.54}$$

Although the simplest way to treat the photon state is to consider a mono-modal Fock construction, the X-ray now should be described as a

multi-modal wavepacket centred at the energy of the beam, k_0. This will define the initial state for the photons as,

$$|\Psi_{\sigma_0\vec{k}_0}\rangle = \sum_{\vec{k}} c_{\vec{k}-\vec{k}_0}|\sigma_0\vec{k}\rangle, \tag{2.55}$$

that can be also be defined as a function of the creation operator $\hat{a}_{\sigma_0\vec{k}}$. After scattering, the final photon state is pure and can also be defined as a creation operator acting in the vacuum state,

$$|\Psi_{\sigma_f\vec{k}_s}\rangle = \hat{a}^{\dagger}_{\sigma_f\vec{k}_s}|vac\rangle. \tag{2.56}$$

The perturbation $O(t)$ is then simplified greatly using the two photon states specified in Eqs. (2.55) and (2.56),

$$\begin{aligned} O(t) = \sum_{\vec{k}} c_{\vec{k}-\vec{k}_0} \sum_j \frac{q_j^2}{2m_j} \sqrt{\frac{\hbar}{\epsilon_0 V\omega_{\vec{k}}}} \sqrt{\frac{\hbar}{\epsilon_0 V\omega_{\vec{k}_s}}} \epsilon_{\sigma_0}\epsilon^*_{\sigma_s} \\ \times e^{\imath(\vec{k}\vec{r}_j-\omega_{\vec{k}}t)} e^{-\imath(\vec{k}_s\vec{r}_j-\omega_{\vec{k}_s}t)}, \end{aligned} \tag{2.57}$$

where the exponential comes directly for the assumption of a multi-modal wavepacket in the initial state . The tractability of the problem will be increased if the previous expression depends on a measurable parameter such as the momentum transfer vector $\vec{q} = \vec{k}_0 - \vec{k}_s$. To introduce it, Eq. (2.57) can be reformulated using the incoming X-ray beam vector, $\vec{k}_0$,

$$e^{i(\vec{k}\vec{r}_j-\omega_{\vec{k}}t)} = e^{\imath(\vec{k}_0\vec{r}_j-\omega_{\vec{k}_0}t)} e^{\imath((\vec{k}-\vec{k}_0)\vec{r}_j-(\omega_{\vec{k}}-\omega_{\vec{k}_0}t)}, \tag{2.58}$$

this factorization allows extracting some of the components from the sum over $\vec{k}$ from the sum, the elements remaining can be seen as an envelope that varies slowly,

$$h(\vec{r}_j, t) = \sum_{\vec{k}} \sqrt{\frac{\omega_{\vec{k}_0}}{\omega_{\vec{k}} + \omega_{\vec{k}_0}}} c_{\vec{k}} e^{\imath(\vec{k}\vec{r}_j-\omega_{\vec{k}}t)}, \tag{2.59}$$

where we have redefined the envelope to be centered at 0, removing the

influence of $\vec{k}_0$ and resulting in a much simpler expression. The perturbation operator can be rewritten then as,

$$\begin{aligned} O(t) = &\frac{\sqrt{2}}{\omega_{\vec{k}_0}}\sqrt{\frac{\hbar}{\epsilon_0 V \omega_{\vec{k}_s}}}\vec{P}\sum_j \frac{q_j^2}{2m_j}E_{\vec{k}_0}h(\vec{r},t) \\ &\times e^{i(\vec{k}_0\vec{r}_j-\omega_{\vec{k}_0}t)}e^{-i(\vec{k}_s\vec{r}_j-\omega_{\vec{k}_s}t)}. \end{aligned} \tag{2.60}$$

where $\vec{P}$ is the polarization vector. To assure finite times in our treatment, we include in Eq. (2.60) Fermi's golden rule, as well as the perturbed wave function and the differential over solid angles,

$$\frac{dS}{d\Omega} = \int d\omega_{\vec{k}_s}\rho(\omega_{\vec{k}_s}) \lim_{t\to\infty}\langle\Psi^{(1)}(t)|\Psi^{(1)}(t)\rangle, \tag{2.61}$$

where $\rho(\omega_{\vec{k}_s})$ represents the density of scattered states. Applying the definition of a perturbed wave function to the above expression, we will get both unperturbed and perturbed operators acting of each side of the bracket,

$$\begin{aligned} \frac{d\sigma}{d\Omega} = &\frac{1}{\hbar^2}\int d\omega_{\vec{k}_s}\rho(\omega_{\vec{k}_s})\int_0^\infty dt''\int_0^\infty dt' \\ &\times\langle\Psi(t'')|\hat{U}(t,t'')^\dagger\hat{O}(t'')^\dagger\hat{O}(t')\hat{U}(t,t')|\Psi(t')\rangle, \end{aligned} \tag{2.62}$$

substituting the operators by their definitions and reordering the equation we will get,

$$\begin{aligned} \frac{d\sigma}{d\Omega} = &\int d\omega_{\vec{k}_s}\frac{\omega_{\vec{k}_s}}{4\pi^3c^3\epsilon_0\hbar\omega_{\vec{k}_0}^2}\vec{P}^2\int_0^\infty dt''\int_0^\infty dt' E_{\vec{k}_0}(t'')E_{\vec{k}_0}(t') \\ &\times e^{-i\omega_{\vec{k}_s}(t''-t')}\langle\Psi(t'')|\hat{L}^\dagger\hat{U}(t'',t')\hat{L}|\Psi(t')\rangle, \end{aligned} \tag{2.63}$$

where we have grouped the envelopes $h(\vec{r},t)$, the field amplitudes $E_{\vec{k}_0}$ and the phases $e^{-i\omega_{\vec{k}_0}t}$ onto $E_{\vec{k}_0}(t)$ functions. The $h(\vec{r},t)$ envelopes can be represented as r-independent functions, $h(t-t_p)$, because they act the same on every point of the system. $\hat{L}$ is again the scattering operator depending on $\vec{q}$, as $q_j^2/2m_j$ is restricted to electrons can be removed out of the sum. If we now make use of the Thomson differential cross section defined previously,

we can eliminate a few terms of the expression written above. Also we can rewrite t as a function of composite variables $t = \frac{t'+t''}{2}$ and $\delta = t'' - t'$,

$$\begin{aligned}\frac{d\sigma}{d\Omega} = \frac{1}{2\pi}\left(\frac{d\sigma}{d\Omega}\right)_{\text{Th}} \int d\omega_{\vec{k}_s} \int_0^\infty dt \int_{-\infty}^\infty d\delta E^*_{\vec{k}_0}(t+\frac{\delta}{2}) E_{\vec{k}_0}(t-\frac{\delta}{2}) \\ \times e^{-\imath\omega_{\vec{k}_s}\delta} \langle \Psi(t+\frac{\delta}{2})|\hat{L}^\dagger \hat{U}(t+\frac{\delta}{2}, t-\frac{\delta}{2})\hat{L}|\Psi(t-\frac{\delta}{2})\rangle,\end{aligned} \tag{2.64}$$

the multiplication of $E^*_{k_0}(t+\frac{\delta}{2})E_{\vec{k}_0}(t-\frac{\delta}{2})$ will represent the initial field we are using in the experiment. Considering a Gaussian profile for the envelope we can consider each of the functions as $e^{-t^2/2\gamma^2}$ reducing the expression to,

$$E^*_{\vec{k}_0}(t+\frac{\delta}{2})E_{\vec{k}_0}(t-\frac{\delta}{2}) = E^2_{\vec{k}_0}|hp(t)|^2\sqrt{hp(\delta)}, \tag{2.65}$$

where,

$$I(t) = E^2_{\vec{k}_0}|hp(t)|^2 \tag{2.66}$$

$$Cp(\delta) = \sqrt{hp(\delta)}. \tag{2.67}$$

With these definitions we can split the integrals into t and δ. Wave functions can be expanded by considering a set of eigenstates of the Hamiltonian forming a coherent superposition (wavepacket) which will be useful to isolate the time contribution from the scattering matrix elements. It is defined as,

$$|\Psi(t)\rangle = \sum c_i e^{-\imath E_i t/\hbar}|\psi_i\rangle, \tag{2.68}$$

and it requires a transformation of time to be included onto the differential scattering expression, $(t+\frac{\delta}{2}, t-\frac{\delta}{2})$. The identity operator, $\mathbb{1} = \sum_k |\psi_k\rangle\langle\psi_k|$, is considered as it will remove the double operator placed between initial and final wave functions,

$$\begin{aligned}\frac{d\sigma}{d\Omega} = \frac{1}{2\pi}\left(\frac{d\sigma}{d\Omega}\right)_{\text{Th}} \int_0^\infty I(t) \sum_{i,j,k} c_i^* c_j e^{-\imath(E_j-E_i)t/\hbar} \\ \int d\omega_{\vec{k}_s} \frac{\omega_{\vec{k}_s}}{\omega_{\vec{k}_0}} \langle\psi_k|\hat{L}|\psi_i\rangle^* \langle\psi_k|\hat{L}|\psi_j\rangle \int d\delta C(\delta) e^{\imath\left(\omega_{\vec{k}_s}-\omega_{\vec{k}_0}+\hbar^{-1}\left(E_k-\frac{E_i+E_j}{2}\right)\delta\right)},\end{aligned} \tag{2.69}$$

in which the sum over k needs to go up to infinity, complicating the treatment. Also, the coherence function Fourier transformation can be interpreted as the power spectrum function F that will depend on the energy of the transitions we are considering.

Following the assumptions made by the Waller-Hartree approximation, we can settle that $\omega_{\vec{k}_s} \approx \omega_{\vec{k}_0}$, that is, the energy of the X-ray does not change during the process. As the initial energy of the X-ray is large enough, this approach is working well even when Compton contributions to the equation are considered. If we introduce this inside our expression, the momentum transfer vector, q, will not depend any more on $\omega_{\vec{k}_s}$ and the matrix elements will be out of the ω integral,

$$\begin{aligned}\frac{d\sigma}{d\Omega} = \frac{1}{2\pi}\left(\frac{d\sigma}{d\Omega}\right)_{\text{Th}} \int_0^\infty I(t) \sum_{i,j,k} c_i^* c_j e^{-\imath(E_j - E_i)t/\hbar} \\ \langle\psi_k|\hat{L}|\psi_i\rangle^* \langle\psi_k|\hat{L}|\psi_j\rangle \int d\omega_{\vec{k}_s} F\left(\omega_{\vec{k}_s} + \frac{1}{\hbar}\left(E_k - \frac{E_i + E_j}{2}\right)\right).\end{aligned} \tag{2.70}$$

2.7 Molecular ultrafast X-ray scattering

The reader might note that thus far we have not considered nuclear degrees of freedom. To do so, we will need to extend Eq. (2.70) to the case where the degrees of freedom include not only the electrons but also the nuclei. We describe the molecular wave function using the Born-Huang expansion,

$$\Psi(\boldsymbol{r}, \boldsymbol{R}, t) = \sum_i \chi_i(\boldsymbol{R}, t)\psi_i(\boldsymbol{r}; \boldsymbol{R}), \tag{2.71}$$

where we should note that $\psi_i(\boldsymbol{r}; \boldsymbol{R})$ is an eigenfunction of the electronic Hamiltonian and only depends parametrically on the nuclear coordinate $\boldsymbol{R}$. This expression can be considered analogous to a Born-Oppenheimer regime as nuclear and electronic degrees of freedom are separated but a non-adiabatic picture can be included in this case. $\chi_i(\boldsymbol{R}, t)$ are the nuclear eigenfunctions and they consider all vibrational and rotational eigenstates of the system.

If we start from the expression of the differential cross section,

$$\frac{d\sigma}{d\Omega} = \frac{1}{2\pi}\left(\frac{d\sigma}{d\Omega}\right)_{\text{Th}} \int_0^\infty I(t) \int \frac{\omega_{\vec{k}_s}}{\omega_{\vec{k}_0}} \int_{-\infty}^\infty C(\delta) e^{-\imath(\omega_{\vec{k}_s} - \omega_{\vec{k}_0})\delta} \Lambda(t,\delta) d\delta d\omega_{\vec{k}_s} dt, \tag{2.72}$$

where we use the coherence function $C(\delta)$ and Waller-Hartree approximation. We define a new quantity that involves both electrons and nuclei in the scattering integrals, called the scattering probability and it is represented by $\Lambda(\delta, t)$. This scattering probability is defined as,

$$\Lambda(\delta,t) = \langle \Psi(\boldsymbol{r},\boldsymbol{R},t) | e^{i\hat{H}_M \frac{\delta}{2\hbar}} \hat{L}^\dagger e^{-\imath \hat{H}_M \frac{\delta}{2\hbar}} \hat{L} e^{\imath \hat{H}_M \frac{\delta}{\hbar}} | \Psi(\boldsymbol{r},\boldsymbol{R},t) \rangle. \tag{2.73}$$

The calculation of $\Lambda(\delta, t)$ will depend on how accurate we want the treatment of the nuclear degrees of freedom. If we expand our wave functions the treatment will require the incorporation of the identity operator,

$$\mathbb{1} = \sum_k |k\rangle\langle k|, \tag{2.74}$$

which only includes the electronic states. A full treatment would include coupled rotational and vibrational eigenfunctions. Inserting it in Eq. (2.73),

$$\Lambda(\delta,t) = \sum_k \langle \Psi(\boldsymbol{r},\boldsymbol{R},t) | e^{\imath \hat{H}_M \frac{\delta}{2\hbar}} | \psi_k \rangle \langle \psi_k | \hat{L}^\dagger e^{-\imath \hat{H}_M \frac{\delta}{\hbar}} | \psi_f \rangle \langle \psi_f | \hat{L} | \psi_i \rangle \langle \psi_i | e^{\imath \hat{H}_M \frac{\delta}{2\hbar}} | \Psi(\boldsymbol{r},\boldsymbol{R},t) \rangle, \tag{2.75}$$

where we have one identity operator for each Hamiltonian to obtain a solvable form. The exponential Hamiltonian terms acting on the eigenstates yield exponents with the corresponding eigenvalues,

$$\Lambda(\delta,t) = e^{-\imath E_{fik}(\vec{r})\delta/\hbar} \langle \Psi(\boldsymbol{r},\boldsymbol{R},t) | \psi_k \rangle \langle \psi_k | \hat{L}^\dagger | \psi_f \rangle \langle \psi_f | \hat{L} | \psi_i \rangle \langle \psi_i | \Psi(\boldsymbol{r},\boldsymbol{R},t) \rangle \tag{2.76}$$

where the the frequency term is,

$$E_{fik}(\boldsymbol{R}) = \hbar\omega_{fik}(\boldsymbol{R}) = E_f(\boldsymbol{R}) - \frac{E_k(\boldsymbol{R}) + E_i(\boldsymbol{R})}{2}. \tag{2.77}$$

Furthermore, in Eq. (2.76) we have the nuclear wave functions,

$$|\chi_k(\boldsymbol{R},t)\rangle = \langle\psi_k|\Psi(\boldsymbol{r},\boldsymbol{R},t)\rangle \tag{2.78}$$

and the scattering matrix elements,

$$\langle\psi_f|\hat{L}|\psi_i\rangle = L_{fi}(\boldsymbol{R}), \tag{2.79}$$

Gathering the various parts we get,

$$\Lambda(t,\delta,\omega_{fij}) = \langle\chi_f(\boldsymbol{R},t)|e^{-\imath\omega_{ifk}(\boldsymbol{R})\delta}L_{ki}L^*_{kf}|\chi_i(\boldsymbol{R},t)\rangle, \tag{2.80}$$

transforming the differential cross section as follows,

$$\begin{aligned}\frac{d\sigma}{d\Omega} = \frac{1}{2\pi}\left(\frac{d\sigma}{d\Omega}\right)_{\text{Th}}\sum_{ifk}\int_0^\infty\int_{-\infty}^\infty I(t)\chi_i(\boldsymbol{R},t)^*\chi_f(\boldsymbol{R},t)dt \\ \int\frac{\omega_{\vec{k}_s}}{\omega_{\vec{k}_0}}L^*_{fk}L_{fk}\int_{-\infty}^\infty C(\delta)e^{-\imath(\omega_{\vec{k}_s}-\omega_{\vec{k}_0}+\omega_{ifk}(\boldsymbol{R}))\delta}d\delta d\omega_{\vec{k}_s}d\boldsymbol{R}.\end{aligned} \tag{2.81}$$

We will now expand the treatment of the X-ray coherence function, $C(\delta)$. The Fourier transform of the coherence function is equal to the power spectral density, as we stated previously,

$$F(\omega_{\vec{k}_s}-\omega_{\vec{k}_0}+\omega_{fji}(\boldsymbol{r})) = \frac{1}{2\pi}\int_{-\infty}^\infty C(\delta)e^{-\imath(\omega_{\vec{k}_s}-\omega_{\vec{k}_0}+\omega_{fji}(\boldsymbol{r}))\delta}d\delta, \tag{2.82}$$

the frequency of the incident photon and the scattered one is approximately the same, $\omega_{\vec{k}_s} \approx \omega_{\vec{k}_0}$ according to the Waller-Hartree approximation applied before. Therefore, the differential cross section is redefined then as,

$$\begin{aligned}\frac{d\sigma}{d\Omega} = \left(\frac{d\sigma}{d\Omega}\right)_{\text{Th}}\sum_{ijf}\int_0^\infty\int_{-\infty}^\infty I(t)\chi_i(\boldsymbol{R},t)^*\chi_j(\boldsymbol{R},t)dt \\ \times L^*_{fi}L_{fj}\int_{\omega_0-\Delta\omega}^{\omega_0+\Delta\omega}F(\omega_{\vec{k}_s}-\omega_{\vec{k}_0}+\omega_{fji}(\vec{r}))d\omega_{\vec{k}_s}d\boldsymbol{R},\end{aligned} \tag{2.83}$$

where instead of using discrete frequencies we have approximated the deviation of $\omega_{\vec{k}_0}$ by using a much smaller quantity that we call $\Delta\omega$. We can

collect the final (frequency) integral in W_{fij}. This integral, W_{fij}, will account for the number of photons in the range $\omega_{\vec{k}_0} \pm \Delta\omega$. We thus obtain Eq. (2.83) in the form,

$$\frac{d\sigma}{d\Omega} = \left(\frac{d\sigma}{d\Omega}\right)_{\text{Th}} \sum_{ijf} \int_0^\infty \int_{-\infty}^\infty I(t)\chi_i(\boldsymbol{R},t)^*\chi_j(\boldsymbol{R},t)dt \times L_{fi}^* L_{fj} W_{ijf}(\Delta\omega,\boldsymbol{R})d\boldsymbol{R}. \tag{2.84}$$

Only the $\boldsymbol{R}$ values in which the probability to find the nuclei is not zero will produce a non-zero result in the scattering signal. Also, the coherence of the X-ray pulse will affect the scattering through $W_{ijf}(\Delta\omega)$.

2.8 Electron scattering formalism

Fast electrons with short de Broglie wavelength scatter from matter much in the same manner as X-rays. Using the notation introduced by Bethe *et al.*[107] that is nicely expounded by Inokuti in his review *Inelastic collisions of fast charged particles* [108], one can relate the expressions obtained for X-ray scattering to electron scattering. The differential cross-section for an electron in the first Born approximation will be,

$$\frac{d\sigma_n}{d\Omega} = \left(\frac{M}{2\pi\hbar^2}\right)^2 \left(\frac{\vec{k}}{\vec{k}_0}\right) \left| \int e^{\imath\vec{q}\vec{r}} u_n(\vec{r}_1,...,\vec{r}_z) V_{u_0}(\vec{r}_1,...,\vec{r}_z) d\vec{r}_1 ... d\vec{r}_z \right|^2 d\omega, \tag{2.85}$$

where M is the reduced mass of the colliding system, $\vec{r}$ is the position of each particle, $\vec{k}_0$ represents the wavevector of the particle before and $\vec{k}$ after the collision. We denote u_n as the eigenfunctions of the electrons, with V_{u_0} the Coulomb (electrostatic) potential.

Integrating over $\vec{r}$, as Bethe did [107], results in a situation similar to the one represented by Eq. (2.45),

$$\frac{d\sigma}{d\Omega} = \left(\frac{d\sigma}{d\Omega}\right)_{Ru} |s(\vec{q},\omega)|^2, \tag{2.86}$$

where Thomson cross-section, $\left(\frac{d\sigma}{d\Omega}\right)_{\text{Th}}$, is replaced by Rutherford cross-section, $\left(\frac{d\sigma}{d\Omega}\right)_{\text{Ru}}$, since we now consider electron-electron scattering. It is defined as,

$$\left(\frac{d\sigma}{d\Omega}\right)_{Ru} = 2\pi\left(\frac{ze^2}{mv^2}\right)Q^{-1}d(lnQ) = 4\pi\left(\frac{Me^2z}{\hbar^2}\right)^2\left(\frac{\vec{k}}{\vec{k}_0}\right)\vec{k}^{-2}\vec{q}^{-4}d\vec{q}^2, \tag{2.87}$$

where z represents the atomic charge, e the electron charge, m the electron mass, v the velocity and Q the kinetic energy of the electron. The structure factor including the $\hat{L}$ operator is equivalent to the one included in Eq. (2.45), considering initial and final states for the scattering process.

Oscillator strengths are usually used to calculate electron scattering. The optical oscillator strength is related to the probability of transition between two different states, and directly influenced by the dipole transition moment between them. To emphasize this, general oscillator strengths are used, given by,

$$f_n(\vec{q}) = (E_n/R_\infty)(\vec{q}a_0)^{-2}|s(\vec{q},\omega)|^2, \tag{2.88}$$

where we have redefined the differential cross-section using the oscillator strengths. In Eq. (2.88) we have included the Bohr radius, a_0, the transition energy, E_n, and the Rydberg constant, R_∞, as well as the structure factor, $s(\vec{q},r)$. To establish the relationship between this value and the optical oscillator strength we can use the limit of $f_n(\vec{q})$ when $\vec{q}$ tends to 0,

$$\lim_{\vec{q}\to 0} f_n(\vec{q}) = f_n, \tag{2.89}$$

where we have included f_n as,

$$f_n = (E_n/R_\infty)M_n^2, \tag{2.90}$$

which is the formalism of the optical oscillator strength, with M_n as the dipole transition moment. In this thesis, the direct analogy between electron and X-ray scattering is particularly exploited in Ch. 4, where we examine inelastic X-ray scattering (IXS) cross-sections and we use experimental data

from both, IXS and electron energy loss spectroscopy (EELS) to validate our calculations.

Chapter 3

X-ray scattering from state-selected molecules

3.1 Introduction

High intensity sources allow the study of new molecular properties. Recent experiments on diatomic molecules such as H_2 and I_2 [31, 109–111], suggest that spatial alignment can be used to characterize rotational and vibrational states of the system when using X-ray scattering [14, 32, 112]. Also, experimental methods to prepare molecules in specific quantum states makes it possible to generate highly anisotropic samples with a large fraction of identical molecules [113–117]. Specifically, the objective of this chapter is to describe the characterization of rotational and vibrational states in CS_2 molecule using elastic X-ray scattering. The importance of alignment is highlighted in X-ray scattering experiments and its relationship with the rotational degrees of freedom is shown [1, 2].

We will use the Born-Oppenheimer approximation to account for vibrational and rotational states. Nuclear degrees of freedom will be treated within the same approach employed in the calculation of pure electronic elastic X-ray scattering [84]. We will explain the theoretical and computational approaches necessary to calculate nuclear degrees of freedom, as well as their inclusion in the X-ray scattering formalism.

A series of *ab-initio* methods and basis sets are benchmarked to demonstrate their influence on the convergence of the X-ray scattering matrix elements. The overall impact accounting for the electronic wavefunction as

compared to IAM, is also discussed.

3.2 Theory

3.2.1 X-ray scattering

The elastic X-ray scattering double differential cross-section reads,

$$\frac{d^2\sigma}{d\Omega d\hbar\omega} = \left(\frac{d\sigma}{d\Omega}\right)_{\text{Th}} \left| \langle \psi_\alpha | \sum_i^{N_{el}} e^{i\vec{q}\vec{r}_i} | \psi_\alpha \rangle \right|^2, \tag{3.1}$$

where we have applied the Waller-Hartree approximation [118] and limited the treatment to the elastic scattering case, considering only matrix elements of the form, $L_{\alpha\alpha}$. The intensity measured on the detector will be proportional to the square of these elements,

$$I(\boldsymbol{q}) \propto |L_{\alpha\alpha}|^2. \tag{3.2}$$

The wavefunction, ψ_α, is usually defined as purely electronic, eliminating any rotational or vibrational influence in the X-ray scattering signal. The simplest approach for calculating the scattering will assume a fixed geometry for the molecule, and calculate the rotationally averaged signal corresponding to the electronic wavefunction or even the independent atom model. However, when molecules are aligned or state-selected, the description should account for the alignment and/or include vibrational and rotational wavefunctions. Using the Born-Oppenheimer approximation, one can express the wavefunction as a product of electronic, vibrational and rotational wavefunctions, in first approximation ignores any coupling between the different components,

$$\psi_\alpha = \Psi^{rot}_{JKM}(\Omega)\Psi^{vib}_{\nu}(\boldsymbol{R})\Psi^{elec}(\boldsymbol{r};\boldsymbol{R},\Omega) \tag{3.3}$$

where $\boldsymbol{r}$ are the electronic coordinates, $\boldsymbol{R}$ the nuclear coordinates and Ω the

angular components. The different terms have been separated considering that the electronic wavefunction, $\Psi^{elec}(\boldsymbol{r};\boldsymbol{R},\Omega)$, only depends parametrically on the internuclear distance $\boldsymbol{R}$ and Ω, which represents the *Euler angles*, (θ,ϕ,χ), that describe the angular components of the rotational wavefunction as represented in Fig. 3.2.

As the scattering operator, $\hat{L} = \sum_i^{N_{el}} e^{\imath\vec{q}\vec{r}_i}$, is a one-electron operator, the influence of nuclear degrees of freedom can be added incoherently to the scattering form-factors. The calculation of the scattering cross-section depends only on the electronic wavefunction, $\Psi_{elec}(\boldsymbol{r};\boldsymbol{R},\Omega)$. The elastic scattering contribution will be then calculated using the electron density, $\rho(\boldsymbol{r};\boldsymbol{R},\Omega)$, as follows,

$$f(\vec{q};\boldsymbol{R},\Omega) = \int \rho(\vec{r};\boldsymbol{R},\Omega)e^{\imath\vec{q}\vec{r}}d\vec{r}, \tag{3.4}$$

where $f(\vec{q};\boldsymbol{R},\Omega)$ is the scattering form-factor. The characterisation of nuclear degrees of freedom will require an incoherent averaging over the vibrational and rotational wavefunctions,

$$\overline{I}(q) = \int_\Omega \int_R |\Psi_\nu^{vib}|^2 |\Psi_{JKM}^{rot}|^2 I(\vec{q};\boldsymbol{R},\Omega), \tag{3.5}$$

where $\overline{I}(\vec{q})$ is the averaged intensity, which includes the influence of the vibrational and rotational states in the molecule.

The calculation of rotational and vibrational wavefunctions is explained below as well as the parametrization of the electronic wavefunction in terms of $\boldsymbol{R}$ and Ω.

3.2.2 Rotational wavefunctions

A rotational wavefunction, Ψ_{JKM}^{rot}, will depend fundamentally on the molecular symmetry. As its name indicates, it will represent the fixed-body rotations of the molecule around different axes, each mode of rotation characterized by one of three principal quantum numbers J, K and L. The classification of molecules depending on their moments of inertia will determine the shape of their wavefunctions and the values J, K, L quantum numbers

can take. The molecules will be divided in three main groups, depending on their symmetry: spherical, symmetric and asymmetric tops (see Fig. 3.1).

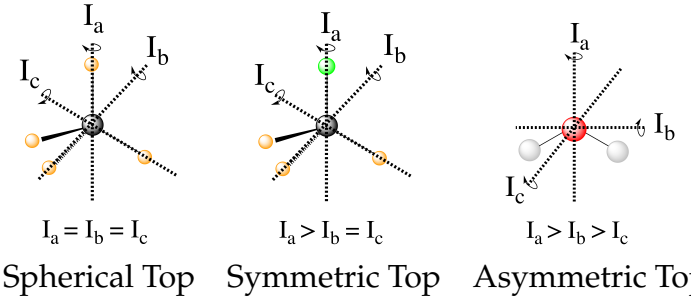

FIGURE 3.1: Representation of the different types of molecules depending on their rotational symmetry, determined by he relative size of the different moments of inertia, I_n. The spherical tops are characterized by $I_a = I_b = I_c$, the symmetric tops by two identical moments of inertia, subdivided into oblate symmetric tops (disc-shaped), $I_a = I_b > I_c$, and prolate symmetric tops (cylindrical) , $I_a > I_b = I_c$, and finally asymmetric tops have $I_a > I_b > I_c$.

To calculate rotational wavefunctions we should solve the Hamiltonian for the rotational states. It is expressed in terms of the moments of inertia in the molecule,

$$\hat{H}_{rot} = \hbar^{-2}(A_e J_a^2 + B_e J_b^2 + C_e J_c^2), \tag{3.6}$$

where A_e, B_e and C_e are the rotational constants of the molecule and J_a, J_b and J_c are the principal inertial axes of the equilibrium configuration. In the calculation of rotational Hamiltonian, the relationships between moments of inertia are crucial to obtain expressions for their wavefunctions.

Spherical and symmetric top molecules

Spherical and symmetric top molecules form the group with the highest symmetry. While spherical molecules belong to high-symmetry groups such as T_d and O_h, all diatomic molecules and any linear system with 3-fold or higher order rotational axis are symmetric tops. Rotational wavefunctions, $\Psi^{rot}_{JKM}(\theta, \phi, \chi)$, for these systems are described by a linear combination of spherical harmonics. To calculate them from a qualitative point

of view, one should apply the rigid rotor approximation, that is, disregard vibrational-coupling terms and centrifugal distortion. The rotational Hamiltonian for a spherical or symmetric top molecule, based on Eq. (3.6), will be,

$$\hbar^{-2}[A_e\hat{J}_a^2 + B_e(\hat{J}_b^2 + \hat{J}_c^2)]\phi_{rot}(\theta,\phi,\chi) = E_{rot}\Psi_{JKM}^{rot}(\theta,\phi,\chi). \tag{3.7}$$

Selecting the a axis parallel to z and substituting the J_a, J_b and J_c operators by $\hat{J}^2$ and $\hat{J}_z$ in Eq. (3.7) yields,

$$\hbar^{-2}[B_e\hat{J}^2 + (A_e - B_e)\hat{J}_z^2]\phi_{rot}(\theta,\phi,\chi) = E_{rot}\Psi_{JKM}^{rot}(\theta,\phi,\chi), \tag{3.8}$$

where E_{rot} is the rotational energy and we have considered the case of an prolate top molecule, meaning that the highest rotational constant is the one along the molecular plane and the other two are smaller and equal, or, $A_e > B_e = C_e$. The energy resultant from the application of this Hamiltonian will follow the rules of a rigid rotor,

$$E_{rot} = B_eJ(J+1) + (A_e - B_e)k^2, \tag{3.9}$$

where k is the eigenvalue of the $\hat{J}_z$ operator and J the eigenvalue of $\hat{J}^2$. Using the rotation matrices and eigenvalues of the operators we can obtain the representation of the wavefunction for a prolate symmetric top,

$$\begin{aligned}\Psi_{JKM}^{rot}(\theta,\phi,\chi) &= [(2J+1)/(8\pi^2)]^{1/2}[D_{MK}^{(J)}(\theta,\phi,\chi)]^* \\ &= (-1)^{M-K}[(2J+1)/(8\pi^2)]^{1/2}[D_{-M-K}^{(J)}(\theta,\phi,\chi)],\end{aligned} \tag{3.10}$$

where $D_{MK}^{(J)}$ are the rotation matrices and J, K and M the rotational quantum numbers, with $|K|$ and $|M|$ having allowed values $\leq J$. The equation can be rewritten as a function of the Euler angles (θ,ϕ,χ),

$$\begin{aligned}\Psi_{JKM}^{rot}(\theta,\phi,\chi) &= X_{KM}^{J}e^{\imath m\phi}e^{\imath k\chi} \\ &\times\left[\sum_{\sigma}(-1)^{\sigma}\frac{\cos(\frac{\theta}{2})^{2J+K-M-2\sigma} - \sin(\frac{\theta}{2})^{M-K+2\sigma}}{\sigma!(J-M-\sigma)!(M-K+\sigma)!(J-K-\sigma)!}\right]\end{aligned} \tag{3.11}$$

where X^J_{KM} is a normalization constant with the form,

$$X^J_{KM} = [(J+M)!(J-M)!(J+K)!(J-K)!(2J+1)/(8\pi^2)]^{1/2}. \quad (3.12)$$

This equation is only valid if the center of mass of the molecule is placed in the origin of the coordinate system and the principal rotational axis is set up along the z direction. Other conventions can be used and they depend on the orientation of the coordinate system and the molecular symmetry (III^r).

If we follow the convention exposed above, all prolate, oblate and spherical top molecules will be sharing the same wavefunctions, although the constants used will share different relationships.

Asymmetric top molecules

Asymmetric top molecules have three different moments of inertia. They constitute the largest group, as most of the molecules do not have sufficient symmetry to be a spherical or symmetric top. The asymmetric rotational wavefunctions cannot be calculated as a combination of spherical harmonics, requiring the diagonalization of the Hamiltonian and subsequent calculation of its eigenvalues. The final result will encompass several symmetric top wavefunctions.

In table 3.1 we have calculated the first wavefunctions for an asymmetric case. To evaluate this case we need a linear combination of symmetric top wavefunctions ($|JKM\rangle$),

$$\Psi^{rot}_{JKM}(\theta,\phi,\chi) = a|JKM\rangle + b|J'K'M'\rangle. \quad (3.13)$$

To obtain the eigenvalues of the rotational Hamiltonian we diagonalize it expressed in the $|JKM\rangle$ basis,

$$\hat{H}_{\text{rot}} = \hbar^{-2}\Big[[(B_e+C_e)/2]\hat{J}^2 + [A_e - (B_e+C_e)/2]\hat{J}_z^2 + [(B_e-C_e)/4][(\hat{J}^+_M)^2 + (\hat{J}^-_M)^2]\Big]. \quad (3.14)$$

J	Wavefunction
0	$E^+ = (\frac{1}{8\pi^2})^{1/2}$
1	$\|1,1,O^+\rangle = [\|1,1\rangle + \|1,-1\rangle] / \sqrt{2}$
	$\|1,1,O^-\rangle = [\|1,1\rangle - \|1,-1\rangle] / \sqrt{2}$
	$\|1,0,E^+\rangle = \|1,0\rangle$
2	$\|2,2,E^-\rangle = [\|2,2\rangle - \|2,-2\rangle] / \sqrt{2}$
	$\|2,1,O^+\rangle = [\|2,1\rangle + \|2,-1\rangle] / \sqrt{2}$
	$\|2,1,O^-\rangle = [\|2,1\rangle - \|2,-1\rangle] / \sqrt{2}$
	$\Phi^+_{\text{rot}}(2,0,E^+)$ = $[c^-\|2,0\rangle + c^+\|2,2\rangle] / \sqrt{2}$
	$\Phi^-_{\text{rot}}(2,0,E^+)$ = $[c^-\|2,0\rangle - c^+\|2,2\rangle] / \sqrt{2}$
$c\pm$	$\pm\frac{2\sqrt{\text{Ae}^2-\text{Ce}(\text{Ae}+\text{Be})-\text{AeBe}+\text{Be}^2+\text{Ce}^2-2\text{Ae}+\text{Be}+\text{Ce}}}{\sqrt{3}(\text{Be}-\text{Ce})}$

TABLE 3.1: Asymmetric top wavefunctions for the three first J values and all K. The nomenclature excludes M, since the equations are independent of M. $E, O, ^+$ and $^-$ depend on whether K is odd or even and the positive or negative linear combination of $|J,K,M\rangle$. The $J = 0$ and $J = 1$ cases are nearly trivial, but calculation of $J = 2$ requires diagonalization of the rotational Hamiltonian matrix.

For each J we will have $(2J + 1)$ states in K and M, the basis need to be built as $\pm K$ linear combinations to be eigenfunctions of the operators presented in H_{rot}. We can classify them by the symbols O^+, O^-, E^+ and E^- depending on the value of K (even or odd) and the sign of the linear combination ($+$ or $-$). The resultant basis functions can be directly diagonal elements of the Hamiltonian and therefore eigenvectors of it. In case we have off-diagonal elements we need to proceed with the diagonalisation of the system, obtaining linear combination of basis as rotational wavefunctions.

Rotational matrix and Euler angles

Rotations are related with a change in the frame constituted by the Euler angles (see Fig. 3.2). To change the laboratory frame, (x, y, z), into the Euler

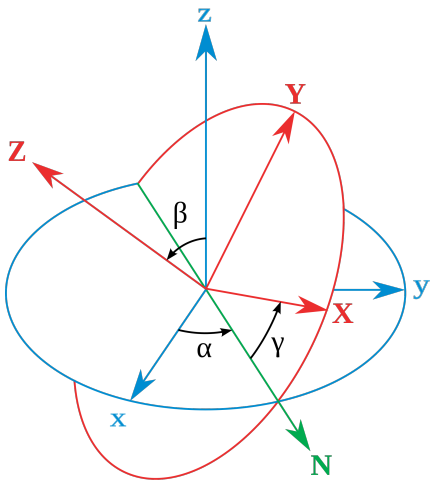

FIGURE 3.2: Definition of the rotational Euler angles (α, β, γ). The two frames are related by the rotation matrix

angles system, (ξ, η, ζ), we should apply a rotational matrix of the form,

$$\begin{pmatrix} x_i \\ y_i \\ z_i \end{pmatrix} = \begin{pmatrix} \lambda_{x\xi} & \lambda_{x\eta} & \lambda_{x\zeta} \\ \lambda_{y\xi} & \lambda_{y\eta} & \lambda_{y\zeta} \\ \lambda_{z\xi} & \lambda_{z\eta} & \lambda_{z\zeta} \end{pmatrix} \begin{pmatrix} \xi_i \\ \eta_i \\ \zeta_i \end{pmatrix}, \tag{3.15}$$

which will be define in terms of the angles between both coordinate systems as expressed in Fig. 3.2,

$$\begin{aligned} \lambda_{i1} &= \begin{pmatrix} \cos\alpha\cos\beta\cos\gamma - \sin\beta\sin\gamma \\ -\cos\alpha\cos\beta\sin\gamma - \sin\beta\cos\gamma \\ \sin\alpha\cos\beta \end{pmatrix} \\ \lambda_{i2} &= \begin{pmatrix} \cos\alpha\sin\beta\cos\gamma + \cos\beta\sin\gamma \\ -\cos\alpha\sin\beta\sin\gamma + \cos\beta\cos\gamma \\ \sin\alpha\sin\beta \end{pmatrix} \\ \lambda_{i3} &= \begin{pmatrix} -\sin\alpha\cos\gamma \\ \sin\alpha\sin\gamma \\ \cos\alpha \end{pmatrix}, \end{aligned} \tag{3.16}$$

where (α, β, γ) are the Euler angles specified in Fig. 3.2. Since the rotation matrix λ is unitary, inverse rotations are given by the transpose of the matrix. The rotation matrix, $D^J_{M,K}(\theta, \phi, \chi)$, has been defined in Eq. (3.10). Its general interpretation relies in the transformation of an eigenstate $|JM\rangle$ to $|JK\rangle$. It can be performed using the relationship,

$$\mathbf{R}(\theta, \phi, \chi)|JM\rangle = \sum_K D^J_{MK}(\theta, \phi, \chi)|JK\rangle. \tag{3.17}$$

The rotation matrix then considers the internal rotations of the wavefunction to express all projections necessary to consider every single quantum number, J, K, M [119].

3.2.3 Vibrational wavefunctions

In the following we will show how vibrational wavefunctions are calculated and their inclusion on the total wavefunction. For simplicity we will restrict our treatment to the simple harmonic oscillator approximation. If one considers a fixed frame for the molecule, the nuclei movements related with vibrational displacement can be expressed as,

$$\Delta\alpha_i = (\alpha_i - \alpha_i^{eq}) \tag{3.18}$$

where α can represent any of the coordinates, x, y or z and eq refers to the equilibrium position. One can use this system of coordinates to obtain the vibrational Hamiltonian for the molecule.

Considering that the vibrational energy is defined as,

$$E_{vib} = \frac{1}{2}\sum_{i=1}^{3N} m_i \Delta\alpha_i + V_N(\Delta\alpha_i), \tag{3.19}$$

where the first term represents the kinetic energy part and the second one is the potential energy, V_N, and expanding the potential energy using a *Taylor's*

series expansion using a the set of vibrational displacements as $\{u_i....u_N\}$,

$$V_N = \frac{1}{2}\sum_{i,j=1}^{3N} k_{ij}u_i u_j + \frac{1}{6}\sum_{i,j,k=1}^{3N} k_{ijk}u_i u_j u_k + \frac{1}{24}\sum_{i,j,k,l=1}^{3N} k_{ij}u_i u_j u_k u_l, \qquad (3.20)$$

which can be approximated to the first term if we consider a harmonic oscillator approach. Presently, vibrational wavefunctions are approximated considering that each active normal mode can be treated as an harmonic oscillator. This approximation is only valid if we consider states with low values of the vibrational quantum number ν to avoid regions of anharmonicity in the potential energy surface.

A molecule presents $3N-6$ vibrational degrees of freedom ($3N-5$ if linear) where N is the number of atoms. We need to build then $3N-6$ wavefunctions and calculate the product between them to obtain the total vibrational wavefunction,

$$\Psi_{\nu}^{vib}(\boldsymbol{Q}) = \prod_{i}^{3N-6} \Psi_{\nu_i}^{\boldsymbol{Q}}(\boldsymbol{Q}_i). \qquad (3.21)$$

The equation for a harmonic oscillator can be expressed as follows,

$$\Psi_{\nu_i}(\boldsymbol{Q}_i) = N_{\nu_i} H_{\nu_i}(\gamma_i^{1/2}\boldsymbol{Q}_i) e^{-\gamma_i \boldsymbol{Q}_i^2/2}, \qquad (3.22)$$

where $\boldsymbol{Q}_i$ is the normal mode coordinate, $\gamma_i = m_i\omega_i$ with m_i being the reduced mass and ω_i the frequency of vibration. The normalization constant is defined as,

$$N_{\nu_i} = \gamma_i^{1/4}/(\pi^{1/2}2_i^{\nu}\nu_i!)^{1/2}, \qquad (3.23)$$

and $H_{\nu_i}(\gamma_i^{1/2}\boldsymbol{Q}_i)$ are the Hermite polynomials.

The harmonic oscillator approach can be extended using anharmonic terms. However, in this Chapter we focus on low-lying vibrational states to ensure that the harmonic approximation is valid.

3.2.4 Centrosymmetry and Friedel's law

The scattering signals usually show centrosymmetric patterns. The molecular scattering signals reflect an increased symmetry by adding an inversion center. This property, exhibited as well in the characterization of crystalline structures, relates to the reflection plane in the molecule, perpendicular to the X-ray beam direction.

If the X-ray beam is pointed in the z direction, $\vec{k}_0 = (0, 0, z)$, two $\vec{q}$ vectors in opposite positions of the detector will vary only in the z component. The condition to fulfill centrosymmetry will be,

$$\vec{q} = (q_x, q_y, q_z) \tag{3.24}$$

$$\vec{q}' = (-q_x, -q_y, q_z) \tag{3.25}$$

$$|F(\vec{q})|^2 = |F(\vec{q}')|^2. \tag{3.26}$$

Friedel's law can be applied only to real-valued functions such as the electron density, that is, $F(\vec{q}) = F^*(-\vec{q})$. The Fourier transformation of the electron density relates x and y directions but not z requiring a symmetry relationship between z components to produce the center of inversion.

The phenomenon can also be seen as a direct relationship between the z components of any two $\vec{q}$ vectors. If a perpendicular reflection plane exists on the molecule, $qz = -qz$ over all space, it will produce centrosymmetric images on the detector.

3.3 Computational details

3.3.1 Effect of basis size in scattering calculations

We have examined the dependence of scattering signal with basis set size in two polyatomic molecules: NH_3 and BF_3. These two molecules have a similar chemical formula but their symmetries are completely different. *Ab-initio* results are obtained within a restricted Hartree-Fock procedure (RHF) without relativistic corrections, while IAM results use HF tabulated factors

including these effects [85, 120, 121]. We evaluate the absolute percent difference or the relative error, $|\%\Delta\tilde{I}(q)|$, for rotationally averaged scattering,

$$\%\Delta\tilde{I}(q) = 100 \times \frac{\tilde{I}_{\text{method}}(q) - \tilde{I}_{\text{ref}}(q)}{\tilde{I}_{\text{ref}}(q)}, \tag{3.27}$$

where $\tilde{I}_{\text{ref}}(q)$ is the reference value taken as the scattering from the HF/aug-cc-PVQZ wavefunction. Figs. 3.3a and 3.3b show the convergence of our calculations with respect to a reference value calculated using a aug-cc-PVQZ Dunning basis. Although we use here Hartree-Fock calculations, this can be understood as a valid comparison when multiconfigurational methods are considered.

Both molecular geometries have been optimised at the HF/aug-cc-pVQZ level using Molpro [122] ($R_{\text{BF}} = 2.444\ a_0$ and $R_{\text{NH}} = 1.886\ a_0$). The absolute percent difference is shown in Fig. 3.3. The differences are not uniform across q, despite that we consider rotationally averaged signals, but rather display significant variation. The maximum errors (differences) can thus be systematically large for specific directions in the scattering signal, particularly when anisotropic samples are considered, e.g. molecular crystals or aligned molecules, even though mean errors are small. It is important to note the poor performance achieved when STO-3G basis are used in Fig. 3.3. STO-3G is worse than the level of theory used to calculate IAM (HF/6-31G). Therefore, the calculation of elastic X-ray scattering using STO-3G calculated wavefunctions is far from the results achieved when larger basis sets are considered. When other basis sets are used to calculate the *ab-initio* electronic wavefunction, the difference between *ab-initio* elastic X-ray scattering and IAM can be attributed to the failure of the latter to account for the redistribution of valence electrons due to chemical bonding i.e. it mainly relates to the valence electrons. The discrepancies between the NH_3 and BF_3 calculated differences bring to light that molecules with a greater number of hydrogen atoms have a propensity to suffer larger errors when the IAM is applied. As a direct consequence of the IAM definition, the larger the number of core electrons in the atom, the better the description of the molecular scattering. An extreme example of this is the H-atom, since its single

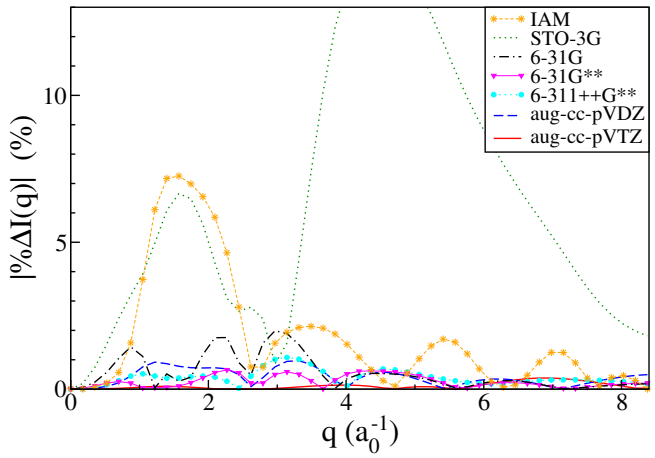

(A) BF_3

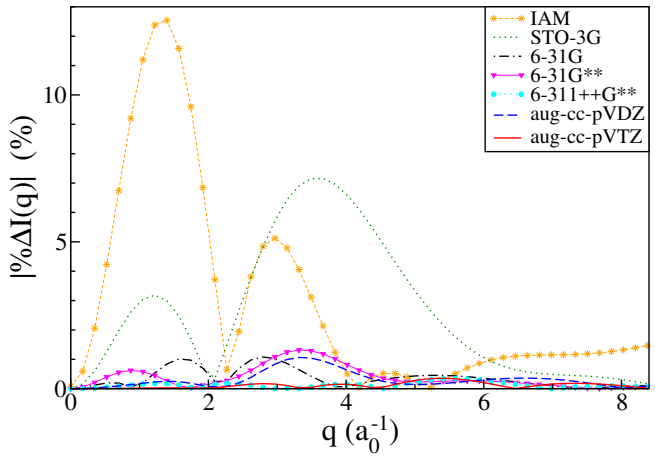

(B) NH_3

FIGURE 3.3: Convergence of the calculated scattering as a function of the basis used for the *ab initio* electronic wavefunction, shown as percent error (see Eq. (3.27)). The comparison is made for molecules BF_3 and NH_3 in the HF/aug-cc-pVQZ ground state optimised geometry, and the scattering signal has been rotationally averaged. The truncated IAM curve in Fig. 3.3a reaches smoothly an error of 15% at approximately $q = 4.4\ a_0$.

1s electron serves as both core and valence shell, resulting in a significant distortion to the electron density in the presence of molecular binding, for instance in H_2 [1, 123].

In Table 3.2 one can see the comparison of different methods and basis sets on these two molecules, using as the reference value the calculations performed using the largest basis set, aug-cc-PVQZ. The maximum and mean errors are calculated as,

$$\langle |\%\Delta\tilde{I}(q)| \rangle = \frac{1}{q_{max} - q_{min}} \int_{q_{min}}^{q_{max}} |\%\Delta\tilde{I}(\vec{q})| \, d\vec{q} \tag{3.28}$$

with the integration interval $[q_{min}, q_{max}] = [0, 8.3]$ a.u. .

In Table 3.2 we can see how poor is the performance of the smallest basis set, STO-3G, as expected. Table 3.2 provides the energy difference, $\triangle E = |E - E_{\text{ref}}|$, of the *ab-initio* calculation with each basis relative the HF/aug-cc-pVQZ reference. If we use $\triangle E$ as a proxy for the convergence of the *ab initio* calculations, we see a clear correlation between $\triangle E$ and the accuracy of the scattering. In BF_3 it correctly identifies the best and the poorest performers, with an unexplained out-performance by the 6-31G** calculation. In NH_3, $\triangle E$, correctly ranks the mean scattering error except for a swapping around of 6-31G and 6-31G**, which rank sixth and fifth in terms of energy, but fifth and sixth in terms of mean scattering convergence. The convergence table also shows the time required for each scattering calculation relative to the largest basis. Although IAM calculations are extremely fast in comparison with *ab-initio*, they only yield qualitative results. Also, it is important to note that the summation and interpolation cannot be compared with an iterative methodology such as the Fourier transforms required in the case of *ab-initio* wavefunctions.

The *ab-initio* scattering calculations essentially scale as the number of terms that have to be evaluated, which in turn depend on the size of the basis used to represent the electronic wavefunction. Table 3.2 shows the number of primitive Gaussian functions per calculation, N_{g}, and more importantly, the number of non-zero unique Gaussian products, N_{gp}. The computational effort to calculate the scattering scales linearly with the number of

METHOD	Error (%)		$\triangle E$	N_g	N_{gp}	Speed
	Mean	Max		($\times 10^3$)		up
BF_3				(E_h)		
IAM	1.75	7.3	-	-		41k
STO-3G	6.36	15	4.69	1.0	10	68
6-31G	0.54	2.0	0.27	1.4	21	31
6-31G**	0.26	0.7	0.16	1.8	32	20
6-311++G**	0.39	1.1	0.07	2.3	51	13
aug-cc-pVDZ	0.41	1.0	0.13	4.3	105	6
aug-cc-pVTZ	0.11	0.4	0.02	8.1	259	3
aug-cc-pVQZ	0	0	0	14	655	1
NH_3				($10^{-1} \times E_h$)		
IAM	2.94	13	-	-		16k
STO-3G	2.54	7.2	7.73	0.1	1.5	173
6-31G	0.35	1.1	0.62	0.2	3	87
6-31G**	0.38	1.3	0.29	0.2	6	43
6-311++G**	0.12	0.3	0.10	0.3	10	26
aug-cc-pVDZ	0.31	1.1	0.20	0.6	19	14
aug-cc-pVTZ	0.11	0.4	0.04	1.2	74	4
aug-cc-pVQZ	0	0	0	2.2	260	1

TABLE 3.2: Convergence and computational requirements for scattering from HF electronic wavefunctions calculated using various basis sets in molecules BF_3 (top) and NH_3 (bottom). The errors are calculated using Eq. (3.27), with the mean (average) error calculated using Eq. (3.28). The energy difference to the reference, $\triangle E = |E - E_{\text{ref}}|$, is used as a proxy for the *ab-initio* convergence. The table also lists the total number of Gaussian primitives, N_g, the number of unique non-zero Gaussian products, N_{gp}, and the relative speed-up of each calculation. The calculations with the aug-cc-pVQZ basis set are used as reference. Note that the ** and ++ basis sets are equivalent to * and + for molecules without hydrogen atoms, such as BF_3.

unique non-zero Gaussian products, N_{gp}, rather than the actual number of Gaussian primitives, N_{g}. For BF_3, $N_{\mathrm{gp}} \approx N_{\mathrm{g}}^{1.38}$, and for NH_3 $N_{\mathrm{gp}} \approx N_{\mathrm{g}}^{1.58}$.

The time required to run the scattering codes can be reduced by using a cutoff value for the Gaussian products or a parallel version of the code. A cutoff of 1×10^{-7} produces the same results as those shown in table 3.2 but the computational time is reduced by a half. Since the Fourier transform calculations scale linearly, we can reduce the computational time in a sixth by parallelising the code in different threads, even more if several cores are used (i.e. MPI parallelization model).

3.4 Results

In the following we calculate the state-selective elastic scattering patterns in CS_2 molecule. Also we will explore the symmetry of the scattering signals obtained and their relationship with the molecular geometry. In each case, the images are shown as detector polar plots, that is, representing the signal variance with spherical angles θ and ϕ. The angles take values between $0 \leq \phi \leq 2\pi$ for the polar angle and $0 \leq \theta \leq \pi$ for the radial angle. The $|\boldsymbol{q}|$ vector dependence is implicit with θ as it depends on its value through the formula $q = 2k_0 \sin\theta/2$. As shown before in Fig. 1.10, the θ and ϕ angles account for the deflection and projection angles of k_i and k_0.

3.4.1 Symmetry and centrosymmetry

Before starting the vibrational and rotational treatment, it is important to remark on the effect of symmetry on the scattering signal. The symmetry of a molecule relative to the X-ray beam is reflected directly in the scattering image. As has been explained before, Friedel's law also applies to gas-phase scattering from aligned molecules, providing the perpendicular plane of symmetry respect to the incoming X-ray direction. Centrosymmetry is produced as a direct consequence of this rule, being characteristic in those molecules with an odd-numbered rotational axis, which is then doubled. In molecules such as BF_3 and the cyclopentadienil anion, $C_5H_5^-$, the existence

of a molecular plane of symmetry produces 6-fold and 10-fold symmetry axis in the scattering pattern (see Fig. 3.4). To establish a general rule one can say that any molecule belonging to a D_{xh} group of symmetry will produce centrosymmetric images.

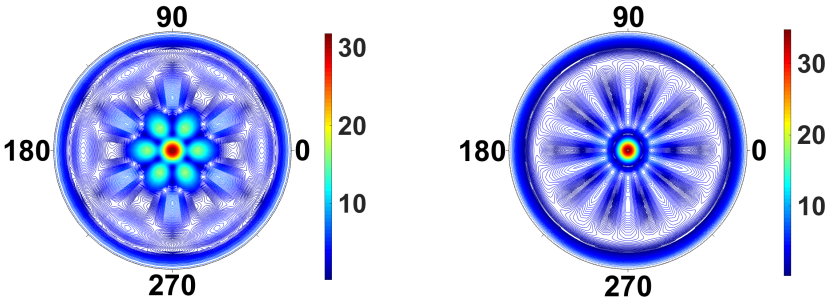

(a) (b)

FIGURE 3.4: Scattering images for (a) BF_3 (D_{3h} point group) and (b) $C_5H_5^-$ (D_{5h} point group). The planar molecules are perpendicular to the incoming X-ray and the resulting diffraction image thus doubles the molecular rotational symmetry axis due to centrosymmetry. The value of $q_{\max}$ is 15.8 $Å^{-1}$.

In contrast, Fig. 3.5 shows the scattering image for NF_3, a strongly-scattering ammonia analogue with C_{3v} point group symmetry. The additional interference due to the out-of-plane nitrogen atom diminishes the centrosymmetry in the image, but the fundamental C_3 axis remains. Proceeding to a molecule with no discernible symmetry, 1,3-cyclohexadiene (C_1 point group), there is a corresponding absence of symmetry in the scattering image. Note, however, that some remnant of '*not-quite*' centrosymmetry remains even in this image. This simply reflects the approximate degree of mirror symmetry perpendicular to the incoming X-ray.

3.4.2 Molecular scattering images

In this section we discuss the elastic scattering images for CS_2 molecule. In many instances, difference images are shown to emphasize the changes in the scattering pattern upon excitation to a specific state. These difference images are calculated by subtracting a reference image from the excited state

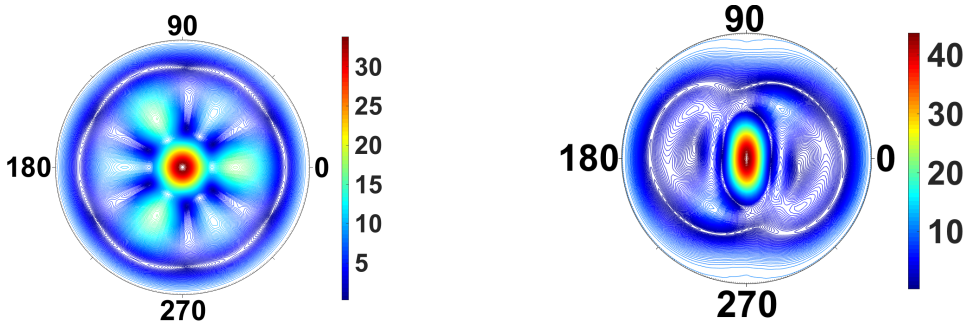

(a) (b)

FIGURE 3.5: Scattering images for (a) NF_3 (C_{3v} point group) and (b) 1,3-cyclohexadiene (C_1 point group). The main plane of the molecules is aligned perpendicular to the incoming X-ray. The absence of a mirror plane orthogonal to the incoming X-rays removes or diminishes centrosymmetry in the images. The value of $q_{\max}$ is 15.8 Å^{-1}.

scattering image, with the subtraction done between images *sans* the absolute square. The molecular scattering images present features that have been discussed in the theory section.

CS_2 vibrational states

The vibrational wavefunctions are expressed as a combination of different normal modes. To establish the analytical treatment of vibrations, one should consider the relationship between the modes and the anharmonicity of them, however, in order to maintain the simplicity and tractability of the problem we have limited our procedure to an harmonic approximation with each of the normal modes described using an harmonic oscillator while the total vibrational wavefunction is the multiplication of those.

To obtain the different normal modes Q, one must know the vibrational frequencies, calculated by solving the Hessian using analytical or numerical methods. In this case we have used CAS$(10,8)$-SCF/6-311G* with an analytical calculation of the Hessian to obtain the frequencies. The electronic structure calculations give us a reasonable degree of accuracy as can be seen in the comparison of calculated frequencies and reference values in Table

3.3, with the calculated vibrational frequencies in CS_2 within 3% of the reference values ones from NIST [124].

Exp. (cm^{-1})	Calc. (cm^{-1})	$\triangle$ (%)	Mode
1535	1491	2.9	Symmetric
658	652	1.0	Asymmetric
397	399	0.6	Bending†

TABLE 3.3: Comparison between experimental [124] and calculated frequencies for CS_2 in the electronic ground state. The frequencies have been calculated using the analytical Hessian at the CAS$(10,8)$-SCF/6-311G* level of theory. The results are within 3% from experiments. †Note that the bending mode is doubly degenerate.

It is important to note that a molecule with heavy atoms, such as sulfur, does not display large-amplitude vibrational motion in the low-lying vibrational states considered here. In Fig. 3.6 scattering images for the different vibrational states in CS_2 are shown. In each image, the vibrational wavefunction has one quantum of excitation in a different vibrational mode. The symmetric, Fig. 3.6(a), and asymmetric, Fig. 3.6(b), stretches give rise to overall similar changes in the scattering pattern, but the asymmetric stretch has additional interferences rings due to the broken symmetry in the $C-S$ bond lengths. Likewise, the two bending modes generate very similar scattering patterns. The difference here are due to the bending mode in Fig. 3.6(c) being oriented perpendicular to the incoming X-ray (in-plane), while it is directed toward the incoming X-ray (out-of-plane) in Fig. 3.6(d). Whether these two modes can be distinguished is therefore dependent on the degree of orientation of the molecule. As discussed above, the vibrational motions in CS_2 have small amplitudes. In terms of the symmetric stretch and the bending modes, one can essentially consider these vibrations as small displacements of the central C atom relative the two nearly-stationary S atoms. The changes in the scattering pattern due to vibrational state are therefore only on the order of 1% or less.

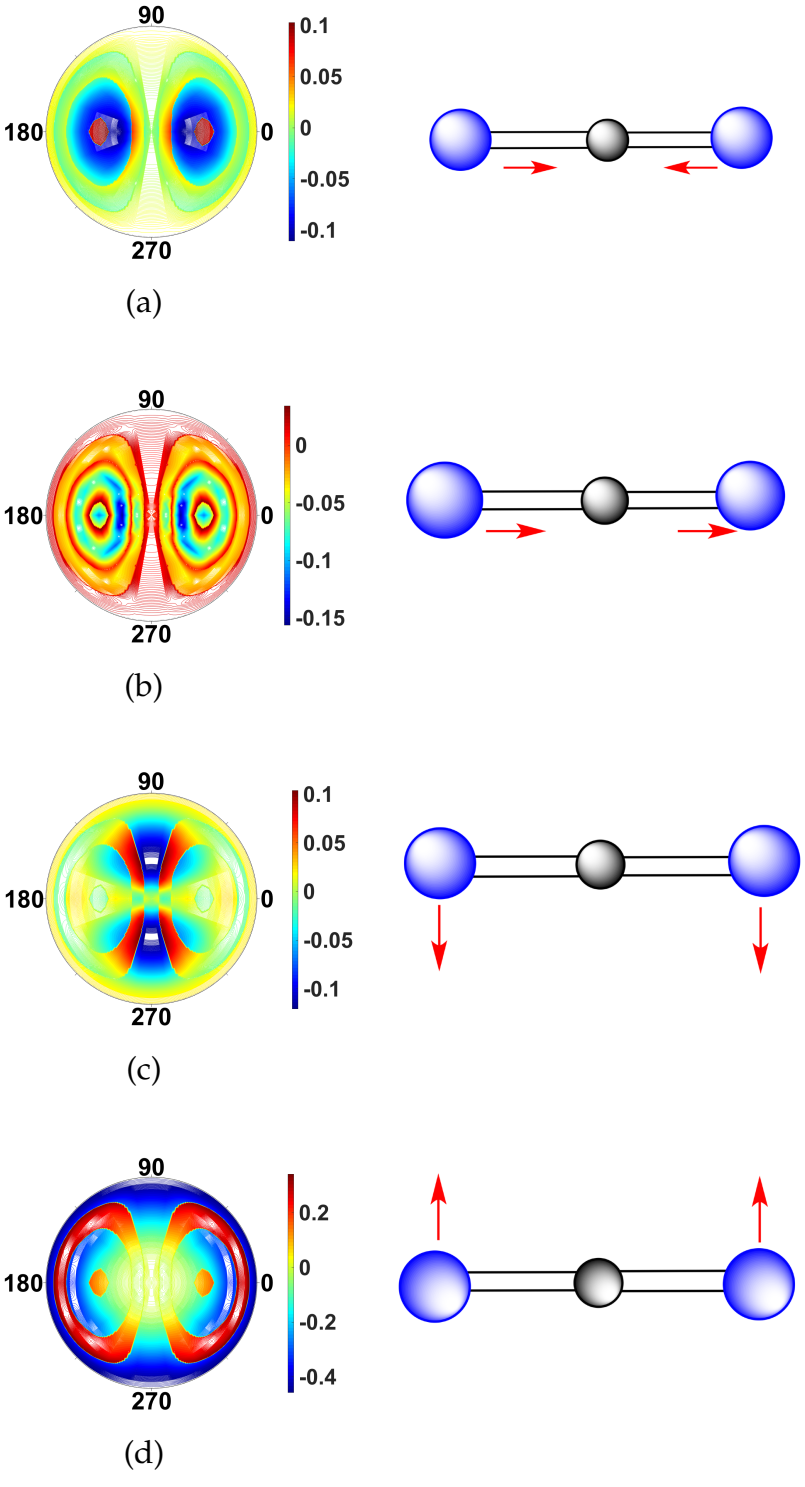

FIGURE 3.6: Difference scattering images for each of the normal vibrational modes of CS_2. The vibrational states are specified as $|\nu_1\nu_2\nu_3\nu_4\rangle_{\text{vib}}$, with the order of vibrational quantum numbers corresponding to descending energy (see Table 3.3). The following vibrational states are considered: (a) Symmetric stretch $|1000\rangle_{\text{vib}}$, (b) asymmetric stretch $|0100\rangle_{\text{vib}}$, (c) first bending mode $|0010\rangle_{\text{vib}}$, and (d) second bending mode $|0001\rangle_{\text{vib}}$. The vibrational ground state $|0000\rangle_{\text{vib}}$ is taken as reference, and the value of q_{max} is 5.3 Å^{-1} in each image.

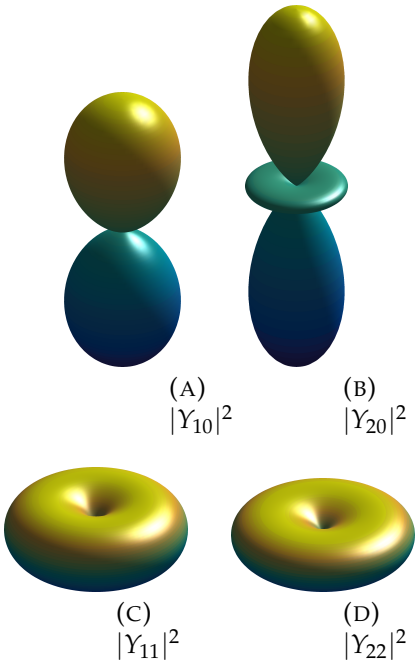

FIGURE 3.7: Square-amplitude of the spherical harmonics, $|Y_{JM}(\theta,\phi)|^2$. The distance from the origin corresponds to the value of $|Y_{JM}(\theta,\phi)|^2$ in each direction - the colour and lighting are for aesthetic purposes only. The angle θ is defined relative the z-axis, which coincides with a C_∞ principal rotation axis, and the origin is a point of inversion.

CS_2 rotations

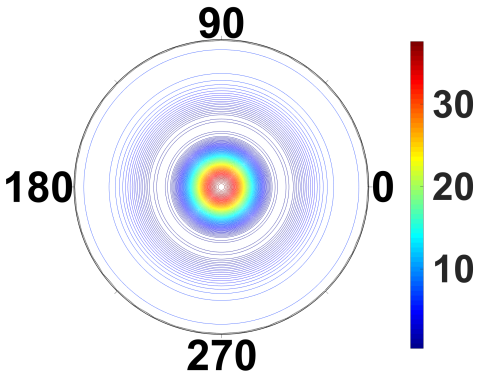

FIGURE 3.8: Rotational averaged image for the ground state in CS_2. As all the directions are treated in the same way and averaged, the resultant differential cross section is concentric. The excitation of different rotational states will break this spherical behaviour and it will highlight the preferred rotations on this state. This image will be used as the reference for future characterisations.

In the following we examine the scattering signal for CS_2 rotational levels. In Fig. 3.8 we have included the ground state rotational state. One can see how all the directions are equally probable, removing the influence of the incoming X-ray beam direction. The scattering from the rotational ground state will be used as the reference value in the following calculations. All rotational states are obtained using the rigid rotor approximation and they will be considered using *ab-initio* X-ray scattering. As we are treating a linear molecule, it is a symmetric top molecule, with the K quantum number always zero. The rigid rotor approximation works well on this case as the centrifugal distortion will not produce a significant change in the final signal. To study the different features on the rotational fine structure, we have exposed along this lines several permutations of J and M quantum numbers, relating the scattering images obtained with the spherical harmonic representation (see Fig. 3.7).

Difference images shown in Fig. 3.9 are calculated using again the ground rotational state, $J = 0$ $M = 0$, as reference. Analyzing the calculated results, one can see that the change in the signal is strong when a

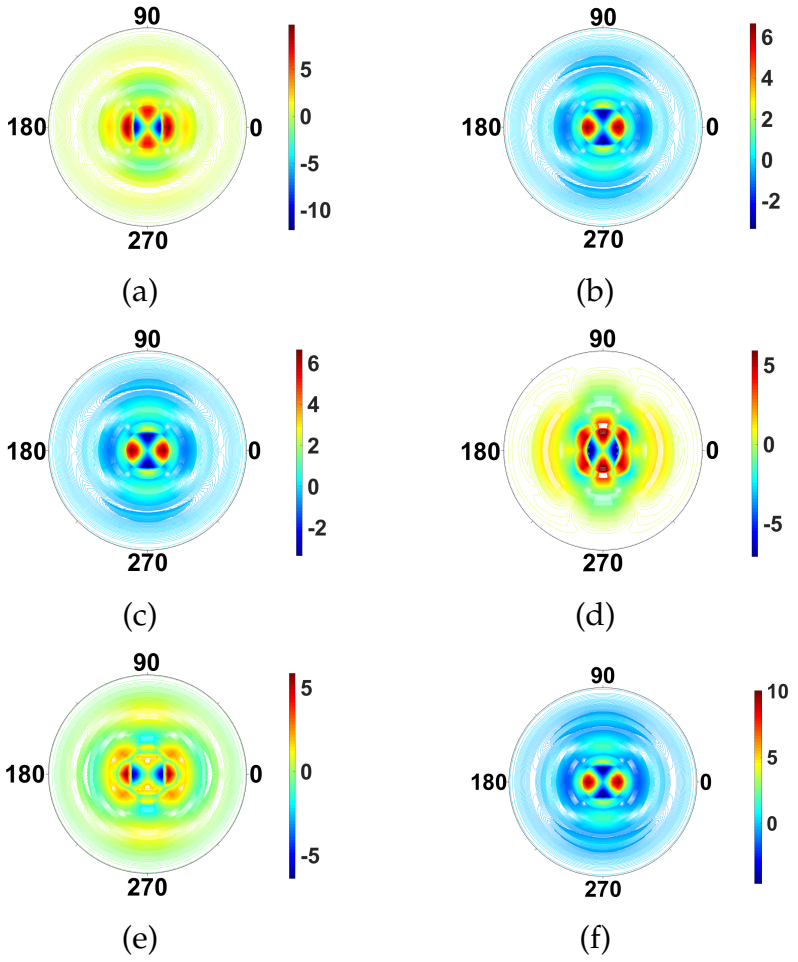

FIGURE 3.9: Difference scattering images for rotational states in CS_2, with the ground rotational state $|000\rangle_{\text{rot}}$ taken as reference. The following rotational states $|JKM\rangle_{\text{rot}}$ are considered: (a) $|100\rangle_{\text{rot}}$, (b) $|101\rangle_{\text{rot}}$, (c) $|10\,{-1}\rangle_{\text{rot}}$, (d) $|200\rangle_{\text{rot}}$, (e) $|201\rangle_{\text{rot}}$ and (f) $|202\rangle_{\text{rot}}$. For the linear CS_2 molecule, with $K = 0$ by definition, the images essentially reflect the shape of the spherical harmonics, with each of the rotational states leaving a strong signature in the scattering. The value of q_{max} is 5.3 Å^{-1} throughout.

rotational level is excited from the ground state. Also, we can see dumb-bell and disc shapes when different values of M are considered, relating them to the spherical harmonics shape. Examining the individual images in Fig. 3.9, we see that the images fall into several categories of similarity. Figs. 3.9(a), 3.9(d), and 3.9(e), are quite similar. They correspond to scattering from dumb-bell or p-orbital type shapes of the rotational wavefunction, with 3.9(d) the most elongated in real space and 3.9((a) the least. The scattering images in Fig. 3.9(b), 3.9(c), and 3.9(f), on the other hand, correspond to doughnut-like shapes, with 3.9(f) the flattest in real space and 3.9(b) and 3.9(c) identical since the difference between them is a phase-factor in the wavefunction which does not affect the scattering.

CS_2 rotational, vibrational, and electronic states

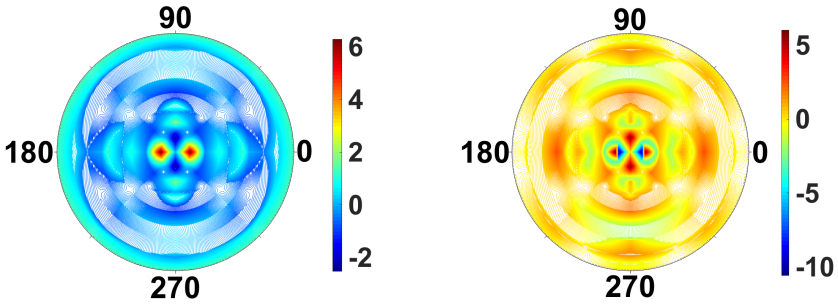

(a) (b)

FIGURE 3.10: Difference scattering images for CS_2 in the electronic ground state for combined rotational-vibrational molecular states (a) $|101\rangle_{\text{rot}}|1111\rangle_{\text{vib}}$, and (b) $|100\rangle_{\text{rot}}|1111\rangle_{\text{vib}}$. The reference scattering image corresponds to the overall ground state ($|000\rangle_{\text{rot}}|0000\rangle_{\text{vib}}$). The shape of the scattering pattern is similar in the two examples, but with inverted intensity. The value of q_{max}=5.3 Å^{-1}.

We move on to simultaneously considering both rotational and vibrational states. Fig. 3.10 shows difference images for the $|101\rangle_{\text{rot}}|1111\rangle_{\text{vib}}$ and $|100\rangle_{\text{rot}}|1111\rangle_{\text{vib}}$ states. The trends observed when considering each type of motion separately, as in previous sections, are preserved. The rotational

states lead to strong, order of magnitude, changes in specific scattering directions (translating into specific pixels on the detector), while the vibrational states leave much weaker signatures on the order of $< 1\%$, which is unsurprising given that only small harmonic oscillations around the equilibrium geometry are considered. If larger amplitude motion were included, the changes in molecular geometry would indeed leave a very strong signature in the scattering and eventually dominate all other contributions.

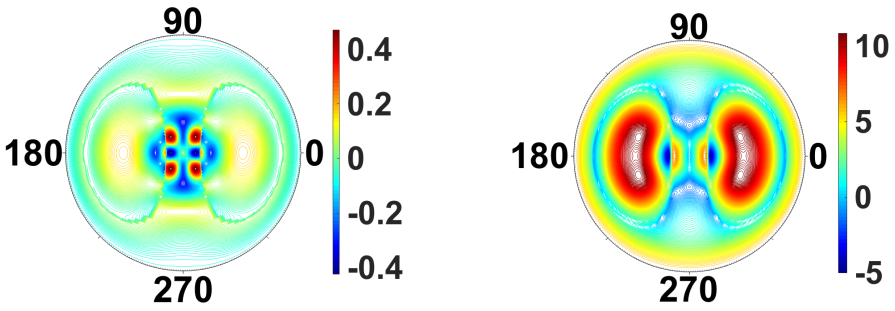

(a) (b)

FIGURE 3.11: Difference scattering images for CS_2 in the optically bright excited electronic $|B\rangle$ state and the electronic ground state $|X\rangle$ in (a) the ground state geometry, i.e. vertical excitation, and (b) the B state equilibrium geometry. The image (b) emphasizes the effect of molecular geometry on the scattering images. The value of $q_{\max}$=5.3 Å^{-1}, and the incoming X-ray is perpendicular to the plane of the molecule in both cases.

As the total molecular wavefunction is discussed in this section, we also consider changes in the electronic state of the molecule. In Fig. 3.11(a) the changes in scattering pattern due to a vertical excitation from the CS_2 ground X state to the bright excited B state are shown. The redistribution of the electrons in the molecule leads to a distinct change in the scattering pattern, not quite on the same order as the effect of rotations, but significantly stronger than the effect of small equilibrium vibrations. It is important to point out, however, that since the equilibrium geometry of the electronic B state is different from the ground X state, nuclear motion necessarily ensues upon excitation, and these large-amplitude vibrations have a strong effect on the diffraction pattern. It is therefore generally non-trivial to separate the

contributions from electronic redistribution and nuclear motion. As an illustration, Fig. 3.11(b) shows the scattering from the molecule in the electronic B state at the B-state equilibrium geometry, rather than the ground state geometry. The change in geometry gives a very large change in the scattering, and overwhelms the effect of rotation and equilibrium vibrations.

3.5 Conclusions

X-ray diffraction considering specific electronic, vibrational and rotational states have been examined in CS_2. The fingerprint of nuclear excited wavefunctions has been shown to be part of elastic X-ray scattering signals. While the excitation of isolated vibrational modes in CS_2 does not produce a dramatic change in the elastic X-ray scattering ($\sim$ 1%), in combination with rotational or electronic excitation it results in a huge effect on the X-ray scattering intensity. The characterisation of rotational states using elastic X-ray scattering has shown that a strong change in the scattering signal is produced when several rotational excitations are considered in CS_2 molecules. In turn, the excitation of low-lying vibrational states in CS_2 produces a small change in the detector image. Electronic states also affect the scattering, with effects comparable to those of rotations in the presence of significant orientation or alignment. However, in most situations electronic excitation leads to changes in the nuclear geometry [125, 126], since the potential energy surfaces associated with different electronic states are rarely parallel. This leads to very strong changes in the scattering, associated with the change in molecular geometry. An interesting point is that the greater the redistribution of electrons during vertical excitation of the molecule, and hence stronger signature of the electronic state, the greater is the effect on the nuclear motion, which itself bears an even stronger signature.

Regarding the *ab-initio* X-ray diffraction method, benchmark calculations for ground and excited states have been done in BF_3 and NH_3 molecules. Also, the X-ray signal for different basis sets and methods has been calculated leading to significant differences when independent atom model (IAM) is used to predict the scattering signal. The quality of the

wavefunction has been proven to be a proxy in the evaluation of elastic scattering matrix elements proving that *ab-initio* X-ray scattering is a good alternative to IAM when quantitative results are required. This remains true even when full rotational averaging is considered, which otherwise has a tendency to smother differences. An extensive explanation of our computational method is given in Ch. 4, where we explain all the characteristic of *ab-initio* X-ray elastic and inelastic scattering.

Chapter 4

Ab-initio inelastic X-ray scattering

4.1 Introduction

This chapter outlines the calculation of inelastic X-ray scattering (IXS) in bound-to-bound transitions using *ab-initio* methods. Non-resonant inelastic scattering, also known as the Compton effect, can be useful to explain processes such as valence electron excitations [28], dispersion of phonons or time-dependent electron dynamics [77]. One of the main advantages of inelastic X-ray scattering is the possibility to access optically forbidden transitions, allowing the characterisation of atomic and molecular electronic structure and dynamics via synchrotron measurements [27, 29, 109, 127–133].

High intensity and short duration pulses generated by XFELs enable *time-resolved* X-ray scattering [9, 21, 22, 31, 64, 134], and thus ultrafast imaging of photochemical dynamics [135]. Structural determination in these experiments is provided via elastic scattering but the question is how inelastic scattering contributes to the general picture. The importance of inelastic scattering matrix elements have been postulated in the propagation of atomic [13, 24] and molecular wave packets [26, 31]. For this reason, we are aiming to calculate here IXS matrix elements using computational tools which will be applied later to an atomic and molecular characterisation of wave packets using time-resolved X-ray scattering.

4.2 Theory

In the following we will describe in detail the calculation of X-ray inelastic scattering elements. Starting from the definition of the differential X-ray scattering cross-section we will develop the theory necessary to include an *ab-initio* wave function within the light-matter interaction picture.

4.2.1 X-ray scattering

The total double differential cross section for X-ray scattering is [77],

$$\frac{d^2\sigma}{d\Omega\,\hbar d\omega_f} = \left(\frac{d\sigma}{d\Omega}\right)_{\text{Th}} s(\vec{q},\omega'), \tag{4.1}$$

where $\left(\frac{d\sigma}{d\Omega}\right)_{\text{Th}}$ is the Thomson cross-section and $s(\vec{q},\omega')$ the *dynamic structure factor* defined in Sec. 2.4. The *dynamic structure factor*, $s(\vec{q},\omega')$, describes the material response,

$$s_{\beta\alpha}(\vec{q},\omega') = \sum_{\beta} \left|\langle\Psi_\beta|\hat{L}|\Psi_\alpha\rangle\right|^2 \delta(E_\beta - E_\alpha - \hbar\omega'), \tag{4.2}$$

where $|\Psi_\beta\rangle$ and $|\Psi_\alpha\rangle$ are the final and initial states, $\omega' = \omega_0 - \omega_1$, and $\hat{L}$ is the scattering operator,

$$\hat{L} = \sum_{j=1}^{N_{el}} e^{i\vec{q}\vec{r}_j}, \tag{4.3}$$

with the sum running over all N_{el} electrons. The momentum transfer vector, $\vec{q} = \vec{k}_0 - \vec{k}_1$, is defined as the difference between the incident and the scattered wave vectors, with $\vec{k}_0 = \vec{k}_1 + \omega'/c$, and $\hbar\omega' = E_\beta - E_\alpha$ the transition energy, which often is negligible compared to the energy of hard X-rays [118]. Eq. (4.2) implicitly assumes that the X-ray energy is tuned away from the absorption edges, which would otherwise force us to account not just for the terms that are square in vector potential, but also for the linear $\hat{p}\hat{A}$ terms.

Isolating elements with $\alpha \neq \beta$, allows us to calculate inelastic X-ray scattering contributions. The electronic density approach proposed by Northey

et al. [84] is not applicable here since we are looking at transitions between different electronic states. This requires a reformulation of the *ab-initio* X-ray scattering method.

4.2.2 Scattering matrix elements

Non-resonant IXS matrix elements correspond to transitions between different electronic states via the scattering operator, $\hat{L}$. Since excited electronic states are considered, multiconfigurational electronic stucture methods are necessary to calculate the electronic wavefunctions. Such methods are more accurate than single-determinant representations, and account for electron correlation better [136]. In multiconfigurational *ab-initio* electronic structure theory the valence electrons are distributed over molecular orbitals in an active space which consists of multiple electron configurations represented by Slater determinants. An electronic state $|\Psi_\alpha\rangle$ can be expanded as,

$$|\Psi_\alpha\rangle = \sum_{i=1}^{N_{\text{conf}}} c_{\alpha,i} \, |\Phi_{\text{SD}}^{\alpha,i}\rangle, \tag{4.4}$$

where $c_{\alpha,i}$ are the configuration interaction coefficients for the α state and $|\Phi_{\text{SD}}^{\alpha,i}\rangle$ is the Slater determinant combination for each i configuration.

The importance of each configuration for a particular electronic state is given by the associated interaction coefficient which also expresses the occupancy of the corresponding orbitals. Each Slater determinant results from the anti-symmetrization of the Hartree product, Φ_H, which can be represented by,

$$|\Phi_{\text{SD}}^{\alpha,i}\rangle = (N_{el}!)^{-1/2} \sum_{n=1}^{N_{el}!} (-1)^{p_n} \mathcal{P}_n \Phi_H^i, \tag{4.5}$$

where N_{el} is the number of electrons, P_n is the pair-wise permutation operator and ϕ_H the Hartree product defined as,

$$\Phi_H = \prod_j^{N_{el}} \chi_j^i(\vec{s}_j)\phi_j(\vec{r}_j), \tag{4.6}$$

where $\chi_j^i(\vec{s}_j)$ are the spin functions and $\phi_j(\vec{r}_j)$ the spatial orbitals. The scattering matrix elements $L_{\beta\alpha}$ between the electronic states β and α are thus given by,

$$\langle \Psi_\beta | \hat{L} | \Psi_\alpha \rangle = \sum_{ii'} c^*_{\beta,i}\, c_{\alpha,i'}\, \langle \Phi^{\beta,i}_{\mathrm{SD}} |\, \hat{L}\, | \Phi^{\alpha,i'}_{\mathrm{SD}} \rangle, \tag{4.7}$$

where we have used the definition in Eq. (4.4) and the scattering operator $\hat{L}$ from Eq. (4.3). In highly symmetric systems (e.g. centrosymmetric systems such as single atoms [136] or diatomic molecules [28]), an effective approach for solving Eq. (4.7) is to expand the $\hat{L}$ operator using the Wigner-Eckart theorem but we do not follow this here. One advantage of our current treatment is that it gives the full physical value of the matrix element straight away.

The evaluation of a Slater product can be worked out using the Slater-Condon rules. We need to consider two cases. The first case occurs if the two Slater determinants are identical,

$$\langle \Phi^{\alpha,i}_{\mathrm{SD}} |\, \hat{L}\, | \Phi^{\alpha,i}_{\mathrm{SD}} \rangle = \sum_{j=1}^{N_{\mathrm{MO}}} b_j\, \langle \phi^i_j |\, \hat{L}\, | \phi^i_j \rangle. \tag{4.8}$$

In the final line of Eq. (4.8), $b_j \in 0, 1, 2$ is the occupancy number for each spatial orbital in the Slater determinant when running the summation over *all* unique spatial orbitals, not just those included in that specific determinant. The second case occurs if the two Slater determinants differ by a single spin orbital when arranged in maximum coincidence,

$$\langle \Phi^{\beta,i}_{SD} |\, \hat{L}\, | \Phi^{\alpha,i'}_{SD} \rangle = \langle \chi^i_N |\, \hat{l}\, | \chi^{i'}_N \rangle = \begin{cases} \langle \phi^i_N |\, \hat{l}\, | \phi^{i'}_N \rangle \\ 0 \end{cases} \tag{4.9}$$

which is nonzero when the spins of χ^i_N and $\chi^{i'}_N$ are parallel, but vanishes via $\langle \downarrow \mid \uparrow \rangle = 0$ otherwise since $\langle \alpha | \beta \rangle = \delta_{\alpha\beta}$ for spins. Finally, if the two Slater determinants differ by more than one spin orbital, the result is always zero.

The Slater-Condon rules assure that a difference of more than one spin-orbital between the elements of the product will grant a zero result to the

integral. In practice, it means that double excitation will have no contribution to the scattering signal and only those permutations involving one electron will be considered in our calculation. Additionally, the spin overlaps should be non-zero, limiting the treatment to singlet-singlet or triplet-triplet transitions.

4.2.3 Evaluation of matrix elements

The next step in our treatment is the evaluation of matrix elements using *ab-initio* wave functions. Taking into account the Slater-Condon rules in Eqs. (4.8) and (4.9), we can exclude elements that differ by more than one spin-orbital. The spatial orbitals are given as combinations of Gaussian functions of the form,

$$\phi_j(\mathbf{r}) = \sum_{k=1}^{N_{\mathrm{BF}}} \mathcal{M}_k^j G_k(\vec{r}), \tag{4.10}$$

where $\mathcal{M}_k^j$ are the molecular orbital expansion coefficients. The total number of basis functions $G_k(\vec{r})$ is N_{BF}, with $j \in N_{\mathrm{MO}} = N_{\mathrm{BF}}$. Each basis function $G_k(\vec{r})$, in turn, is a contraction of Gaussian-type orbitals (GTOs), $g_s(\vec{r})$, such that,

$$G_k(\vec{r}) = \sum_{s=1}^{\mathrm{n}_k} \mu_s^k g_s^k(\vec{r}), \tag{4.11}$$

where μ_s^k are the basis set contraction coefficients for the primitive GTOs. A Cartesian Gaussian-type orbital centered at coordinates $\vec{r}_s = (x_s, y_s, z_s)$ has the form,

$$g_s(\vec{r}) = \mathcal{N}_s (x - x_s)^{l_s} (y - y_s)^{m_s} (z - z_s)^{n_s} e^{-\gamma_s (\vec{r} - \vec{r}_s)^2}, \tag{4.12}$$

with exponent γ_s, Cartesian orbital angular momentum $L_s = l_s + m_s + n_s$, and normalisation constant $\mathcal{N}_s$,

$$\mathcal{N}_s = \left(\frac{2}{\pi}\right)^{3/4} \frac{2^{(l_s+m_s+n_s)}\ \gamma_s^{(2l_s+2m_s+2n_s+3)/4}}{\left[(2l_s-1)!!(2m_s-1)!!(2n_s-1)!!\right]^{1/2}}, \tag{4.13}$$

where !! denotes the double factorial. A double factorial or semi-factorial is a generalization of the usual factorial ! that represents the product of all elements from one up to some non-negative integer n that have the same parity (i.e. odd or even numbers). The usage of Cartesian GTOs is convenient in the present context, but there is of course a direct mapping between Cartesian and spherical Gaussians [137]. If spherical Gaussians are used, the mathematics of the analytic Fourier transform takes a different form [138]. It should be noted that spherical Gaussians are much more convenient for centrosymmetric systems where an expansion of the $\hat{L}$ operator in partial waves using the Wigner-Eckart theorem is appropriate (see Sec. 5.2.2).

The one-electron bracket can then be evaluated as,

$$\langle \phi_a | \, \hat{l} \, | \phi_b \rangle = \sum_{k_1,k_2}^{N_{\mathrm{BF}}} \mathcal{M}_{k_1}^{a} \mathcal{M}_{k_2}^{b} \sum_{s_1,s_2}^{\mathfrak{n}_{k_1},\mathfrak{n}_{k_2}} \mu_{s_1}^{k_1} \mu_{s_2}^{k_2} \, K_{s_1 s_2}^{k_1 k_2} \, \mathcal{F}_{\vec{r}}[g_{s_1 s_2}^{k_1 k_2}(\vec{r})](\vec{q}),$$

where we use the Gaussian product theorem [139] to rewrite the product $g_{s_1}^{k_1}(\mathbf{r}) g_{s_2}^{k_2}(\vec{r})$ as,

$$g_{s_1}^{k_1}(\vec{r}) g_{s_2}^{k_2}(\vec{r}) = K_{s_1 s_2}^{k_1 k_2} \, g_{s_1 s_2}^{k_1 k_2}(\vec{r}), \tag{4.14}$$

where $K_{s_1 s_2}^{k_1 k_2} = \exp[-\gamma_{s_1}^{k_1} \gamma_{s_2}^{k_2} (\vec{r}_{s_1}^{k_1} - \vec{r}_{s_2}^{k_2})^2 / (\gamma_{s_1}^{k_1} + \gamma_{s_2}^{k_2})]$ is the pre-factor and $g_{s_1 s_2}^{k_1 k_2}(\mathbf{r})$ is a new Gaussian centered at $\vec{r}_{s_1 s_2}^{k_1 k_2} = (\gamma_{s_1}^{k_1} \vec{r}_{s_1}^{k_1} + \gamma_{s_2}^{k_2} \vec{r}_{s_2}^{k_2}) / (\gamma_{s_1}^{k_1} + \gamma_{s_2}^{k_2})$ with exponent $\gamma_{s_1 s_2}^{k_1 k_2} = \gamma_{s_1}^{k_1} + \gamma_{s_2}^{k_2}$. Since the Cartesian coordinates (x, y, z) are linearly independent and each Gaussian function can be written as a product of x, y and z components,

$$g_{s_1 s_2}^{k_1 k_2}(\vec{r}) = \prod_{r'=x,y,z} g_{s_1 s_2}^{k_1 k_2}(r'), \tag{4.15}$$

the problem is reduced to the solution of one-dimensional Fourier transforms,

$$\mathcal{F}_x \left[g_{s_1 s_2}^{k_1 k_2}(x) \right] (q). \tag{4.16}$$

To calculate the Fourier transform of one-dimensional Gaussians we can express them as,

$$g(x; l) = x^l e^{-\gamma x^2}, \tag{4.17}$$

where l is the angular momentum in the Cartesian representation. The Fourier transform of these terms can be determined analytically using the recursive formula from Ref. [84],

$$\mathcal{F}_x[xf(x)](q) = -\imath\frac{d}{dq}\mathcal{F}_x[f(x)](q) \tag{4.18}$$

which leads to a general expression for Eq. (4.16) of the form,

$$\mathcal{F}_x[g(x;l)](q) = \frac{\imath^l\sqrt{\pi}e^{-q^2/4\gamma}}{2^l\gamma^{(2l+1)/2}}\sum_{p=0}^{l/2}(-1)^p\frac{l!\gamma^p q^{l-2p}}{(l-2p)!p!}. \tag{4.19}$$

Reference [84] provides a table of solutions. The calculation of the Fourier Transformations can also be done numerically using Fast Fourier Transformation (FFT) [84].

4.3 Computational details

In the following we will explain the main features associated with the practical calculation of IXS matrix elements using computational procedures. The analysis of *ab-initio* results and the calculation of matrix elements is carried out using a code developed by myself called *Ab-Initio X-ray Diffraction: Elastic and Inelastic* (AIXRDEI). The main assumptions made in this code are collected in the theory (Sec. 4.2) and *ab-initio* sections (Sec. 4.3.1) , but a few additional points will be discussed below.

4.3.1 Electronic structure calculations

As mentioned earlier in this thesis, multiconfigurational methods are required to describe excited states in atoms or molecules. We have chosen complete active space self-consistent field (CASSCF), described in Sec. 1.7.2, as our reference procedure. As we are treating small systems, large active spaces are chosen, without any frozen orbitals. State-averaged calculations are used throughout this chapter, allowing us to consider different electronic

states in an even-handed manner. Symmetry is applied whenever applicable, which makes it possible to isolate angular momentum components, and thus enabling e.g. monopole decomposition.

We also use multireference configuration interaction (MRCI) in a few instances in order to establish an upper limit on the accuracy. The theory is analogous to CASSCF but uses reference Slater determinants calculated through a perturbation theory scheme or specified by the user. The results are usually better in terms of the energy since dynamic correlation is better accounted for. However, in some cases the lack of symmetry in the state-averaged MRCI calculations, produces worse results than CASSCF.

The IXS calculations require that both CASSCF and MRCI use configuration state functions (CSFs) instead of unmatched Slater determinants. The reason is technical; usage of spin-weighted Slater determinants will produce a zero result in average as both possible spin contributions are expressed with opposite signs. The output from the electronic structure calculations when using CSFs, on other hand, expresses the spin populations as branches with merely statistical meaning in terms of spin quantum numbers, producing a non-zero result when average is done.

To calculate IXS matrix elements, a permutation over different configurations is done. Applying Slater-Condon rules, the possible products between states are reduced to the instances where only one spin-orbital differs between determinants. The pseudo-code expression thus reads,

$$\langle \Psi_\beta | \hat{L} | \Psi_\alpha \rangle = \left| \sum_{i,j}^{N_{CI}} v_{\beta,i}^{CI} v_{\alpha,j}^{CI} \langle \Phi_{\mathrm{SD}}^{\beta,i} | \, \hat{L} \, | \Phi_{\mathrm{SD}}^{\alpha,j} \rangle \right|^2 , \tag{4.20}$$

where v_α^{CI} are the CI-vectors of length N_{CI}. One can take these coefficients and the associated configuration directly from the multiconfigurational calculation. All *ab-initio* electronic structure calculations are carried out using the MOLPRO software package [122].

4.3.2 The X-ray scattering code

The code reads the output from the electronic structure calculations (presently the code only interfaces MOLPRO [122]), and iterates over all orbitals and configurations to calculate the required Fourier transforms. One can choose what matrix elements to calculated by selecting the two states involved,

$$L(1,2) \rightarrow \sum_{i,j}^{N_{CI}} v_{1,i}^{CI} v_{2,j}^{CI} \mathcal{F}\left[\langle \phi_1 | \hat{L} | \phi_2 \rangle\right](q), \tag{4.21}$$

which is analogous to Eq. (4.20). The code outputs by default the (dynamic) structure-factors calculated using Eq. (4.2) but as electron scattering is sometimes also considered, the output can also be provided in the form of generalized oscillator strengths (GOSs). The calculation of GOSs is explained in Ref. [136]. They are given by,

$$G(q, \omega_n - \omega_0) = \frac{2(\omega_n - \omega_0)}{q^2} |s(q, \omega_n - \omega_0)| \tag{4.22}$$

where Eq. (4.22) includes implicit rotational average, calculated using the amplitude of dynamic structure form factors(i.e. without the associated phase). The energy resolution is not averaged though, isolating particular transitions.

4.3.3 Geometric considerations

The momentum transfer vector, $\vec{q}$, is calculated using Ref. [80]. Setting the incident X-ray vector, $\vec{k}_0$, parallel to the $\hat{z}$-direction,

$$\vec{k}_0 = k_0 \begin{pmatrix} 0 \\ 0 \\ 1 \end{pmatrix} \tag{4.23}$$

$$\vec{k}_1 = k_1 \begin{pmatrix} \sin(\theta)\cos(\phi) \\ \sin(\theta)\sin(\phi) \\ \cos(\theta) \end{pmatrix} \tag{4.24}$$

$$\vec{q} = \begin{pmatrix} -k_1 \sin(\theta)\cos(\phi) \\ -k_1 \sin(\theta)\sin(\phi) \\ (k_0 - k_1)\cos(\theta) \end{pmatrix}, \tag{4.25}$$

where $\vec{k}_1$ represents the scattered X-ray beam. In the case of the elastic scattering, the k_0 and k_1 wavevectors have identical length as no energy transfer is involved. Albeit negligible in magnitude when compared to the X-ray energy, inelastic X-ray scattering produces a change in the energy of the X-ray,

$$\omega_f = \omega_i - \frac{\Delta E_{trans}}{\hbar}, \tag{4.26}$$

where ΔE_{trans} corresponds to the energy involved in the transition and $\hbar$ is Planck's constant.

As molecules are not usually aligned with respect to the incoming X-ray, we should introduce the so called *incoherent rotational average* to account for the anisotropy of molecular orientations. It reads,

$$\langle S(q,\omega')\rangle^2 = \int_\Omega |S(\vec{q}(\theta,\phi,\gamma),\omega')|^2 \sin^2\theta d\theta d\phi d\chi, \tag{4.27}$$

where θ, ϕ and γ are the so-called *Euler angles* with $d\Omega = d\theta d\phi d\gamma$, and q is the momentum transfer vector. The integration of scattering structure-factors over all directions produces an isotropic signal which only depends on $q = |\vec{q}|$.

4.4 Results

4.4.1 Single-electron atoms

We begin by validating our methods for single-electron atoms where the solution is known analytically, as discussed in Sec. 5.2.2. Specifically we examine the inelastic scattering for H and He^+. The *ab-initio* electronic wave functions are calculated at the CASSCF(3,1) level, using the Dunning d-aug-cc-PV5Z basis. The diffuse augmented family of Dunning basis sets allows a better description of the diffuse orbitals. Hydrogen-like atoms present

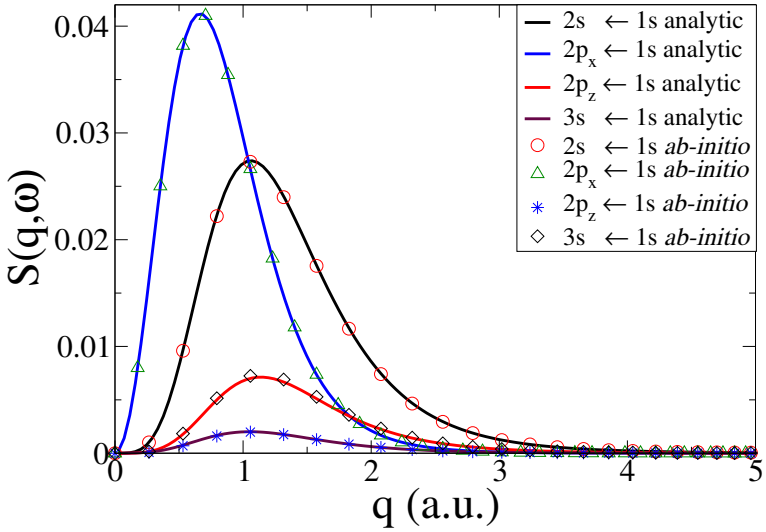

(A) H

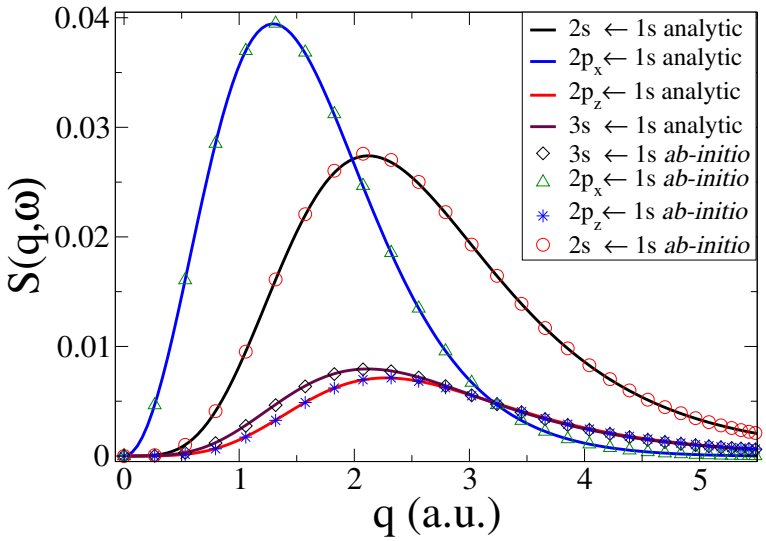

(B) He^+

FIGURE 4.1: Comparison between numerical *ab-initio* calculations, using our approach, and analytical results for (a) the H neutral atom, and (b) the He^+ cation. The dynamic structure factor, $S(q, \omega)$, is shown for the transitions $2s \leftarrow 1s$, $2p_x(2p_y) \leftarrow 1s$, $2p_z \leftarrow 1s$, and $3s \leftarrow 1s$.

Rydberg-like behaviour when the principal quantum number n is greater than one, requiring a good description of the diffuse parts of electron wavefunctions. Results obtained with more common basis sets, although they

agree well in terms of the energy, show poor agreement in the $s(\vec{q},\omega)$ for small values of q, emphasizing the importance of a correct description of the wavefunction at large r. Transition energies for the levels under consideration, $(2s, 2p, 3s) \leftarrow 1s$, are within $< 0.1\%$ of the experimental [140] and analytical results. As can be seen from Fig. 4.1, the *ab-initio* results agree extremely well with the analytical solutions. Comparing the He^+ states in Fig. 4.1b with the H states in Fig. 4.1a, the more compact wavefunction density in He^+ results in a shifting of the maximum values of the matrix elements towards larger q. It reflects the inverse relationship between real space, r, and reciprocal space, q. The agreement between *ab-initio* and analytic results demonstrates the accuracy of our calculation for sufficiently accurate *ab-initio* electronic wavefunctions.

4.4.2 Two-electron atoms

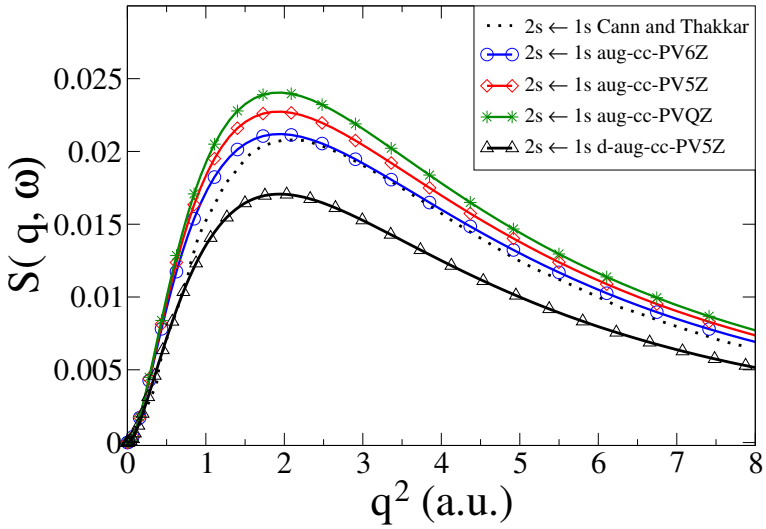

FIGURE 4.2: Calculated dynamic structure factor, $S(q,\omega)$, in He for the $^1S_0\,(1s2s) \leftarrow {}^1S_0\,(1s^2)$ transition compared to results from Cann and Thakkar [141]. The numerical calculations are performed with CASSCF(2,10) and four Dunning basis sets (aug-cc-PVQZ, aug-cc-PV5Z, aug-cc-PV6Z, and d-aug-cc-PV5Z).

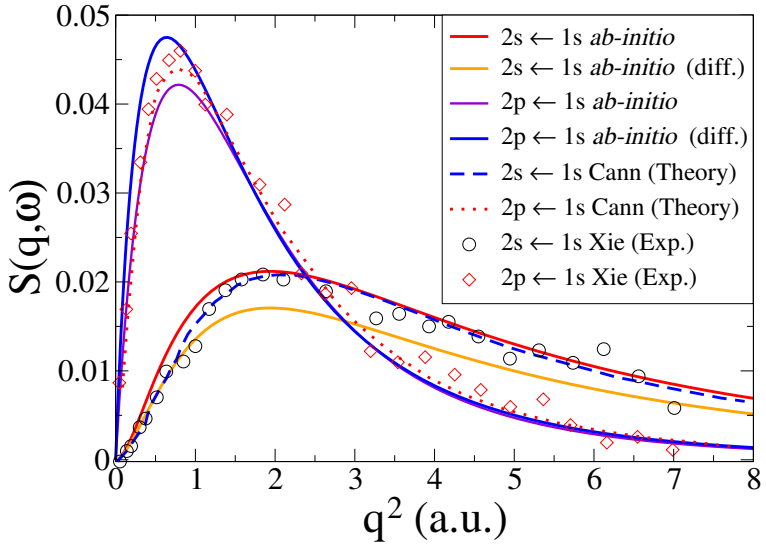

FIGURE 4.3: Calculated dynamic structure factor, $S(q,\omega)$, in He for the ${}^1S_0\,(1s2s) \leftarrow {}^1S_0\,(1s^2)$ and ${}^1P_1\,(1s2p) \leftarrow {}^1S_0\,(1s^2)$ transitions compared to theory by Cann and Thakkar [141] and experiments by Xie *et al.* [131]. The *ab-initio* calculations are done at the CASSCF(2,10)/aug-cc-PV6Z and the CASSCF(2,10)/d-aug-cc-PV5Z levels, with the d-aug results identified by the label "(diff.)".

We now consider the neutral He atom, a two-electron system. The electronic states of He are well known from the literature. The energy convergence for CASSCF(2,10) *ab-initio* calculations with four different Dunning basis sets is shown in Table 4.1 for the two excited states ${}^1S_0\,(1s2s)$ and ${}^1P_1\,(1s2p)$. The corresponding dynamic structure factor for the ${}^1S_0\,(1s2s \leftarrow {}^1S_0\,(1s^2)$ transition from the ground state is shown in Fig. 4.2 together with reference calculations using explicitly correlated wave functions by Cann and Thakkar [141].

Ab-initio calculations are performed using symmetry cards for states with $l \neq 0$, which allows the isolation of specific angular momentum components. The IXS code benefits from symmetry specifications as they make possible to split the results into different monopole contributions.

As discussed above, good agreement is found between our results and the reference values. Maximum convergence is reached when the larger

He	$^1S_0(1s2s)$		$^1P_1(1s2p)$	
	E (eV)	ΔE (%)	E (eV)	ΔE (%)
Exp. [140]	20.615	–	21.218	–
PVQZ	20.793	0.8	23.943	12.8
PV5Z	20.748	0.6	23.078	8.8
PV6Z	20.684	0.3	22.667	6.8
d-PV5Z	20.000	3.0	20.680	2.5

TABLE 4.1: The energies E for the $^1S_0\,(1s2s)$ and $^1P_1\,(1s2p)$ states in He calculated at the CASSCF(2,10) level with Dunning basis sets: aug-cc-PVQZ, aug-cc-PV5Z, aug-cc-PV6Z, and d-aug-cc-PV5Z. The percentage error, ΔE, compared to experimental values from NIST [140] is also given.

basis set is used, establishing a direct relationship between the level of theory employed in the *ab-initio* calculations and the accuracy of the inelastic matrix elements. The same behaviour has been shown recently for elastic scattering contributions [1, 2]. The result might improve if a higher number of determinants is used or a higher level of *ab-initio* theory is used, using for instance full-CI methods. The main discrepancies occur at lower values of q, suggesting that it is the tail of the wave function which is the most difficult to converge. Even though the description can be improved, the results are good overall and the energy convergence shows excellent agreement with experimental values as shown in Table 4.1.

The next step is to consider other transitions in He. In Fig. 4.3 we compare our dynamic structure factors for the two transitions $^1S_0\,(1s2s) \leftarrow {}^1S_0\,(1s^2)$ and $^1P_1\,(1s2p) \leftarrow {}^1S_0\,(1s^2)$ to experimental results by Xie *et al.* [131] and reference calculations by Cann and Thakkar [141]. In reference [141] $s(q,\omega)$ is calculated using a highly accurate wavefunction, obtained using a sophisticated R-matrix procedure. In particular, R-matrix theory uses exact Coulomb functions for the long-range single-electron tail of the wavefunction. For this reason, the reference results agree better with the experimental ones at $q < 2$ a.u.. Nevertheless, our results show a very good agreement

with both experimental and computational reference values. As expected, the inclusion of diffuse basis functions in the electronic *ab-initio* wavefunction calculation yields better results at small q when treating the $^1P_1$ transition. Energy convergences are shown in Table 4.1. The differences between our result and the references could come from the angular momenta definition we have used. To isolate different contributions using *ab-initio* is difficult even when using symmetry cards, making a careful inspection of the *ab-initio* results necessary to assign various components of the transition.

4.4.3 Multi-electron atoms

Below we treat Ne, C and Na atoms. As has been mentioned before, some of the inelastic scattering reference data is provided by electron energy-loss spectroscopy (EELS) studies. Data from EELS is generally provided in terms of generalised oscillator strenghts (GOSs) and in order to match tabulated data, our results for C and Na are given in terms of GOSs rather than dynamic structure factor as before. Oscillator strengths are dimensionless quantities that express the probability of absorption or emission between two levels in an atom or molecule. When the momentum transfer vector is zero, generalized oscillator strengths are equivalent to the oscillator strength, providing an alternative route for characterising the oscillator strengths for optical dipole transitions.

Ne

Inelastic scattering in Ne atom can be studied experimentally using two main techniques, *Inelastic X-ray Scattering* (IXS) [29] and *Electron Loss Spectroscopy* (EELS) [142]. Since Ne is a noble gas atom the probability of transitions is low. We consider the main valence excitations from the stable closed-shell np^6 ground state and we compare our results with reference results, both theoretical [136, 143] and experimental [29, 142].

As we are considering $2p^5 3s, 2p^5 3p \leftarrow 2p^6$ transitions, the total angular momentum can be decomposed into several components, $l = 0, 1, 2....$ Likewise, the matrix elements can show be partitioned into monopole, dipole

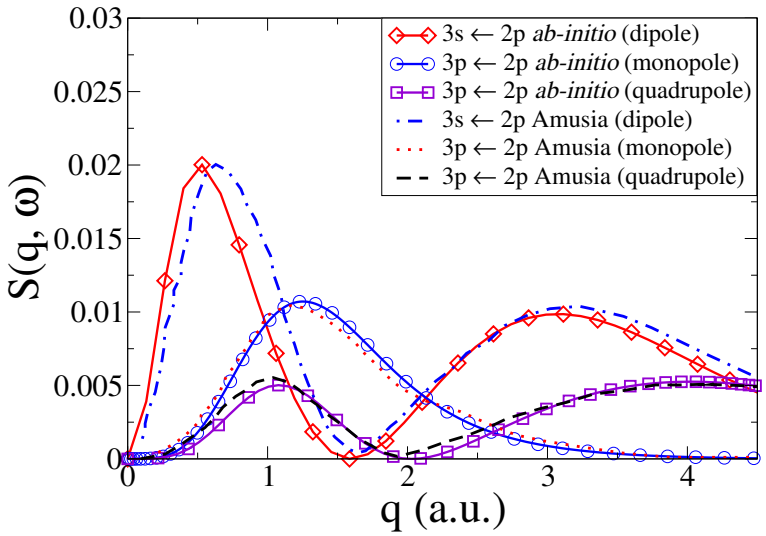

FIGURE 4.4: The dynamic structure factor, $S(q,\omega)$, in Ne for the $3s \leftarrow 2p$ dipolar and $3p \leftarrow 2p$ monopolar and quadrupolar transitions compared to results by Amusia *et al.* [136].

and quadrupole contributions. We have performed a CASSCF(9,10)/aug-cc-PVTZ calculation to isolate each of these transitions. Symmetry cards are necessary for this purpose, isolating three different angular momentum components. The energies obtained for each of the processes studied are collected in Table 4.2 showing an excellent agreement with experimental reference values.

In Fig. 4.4 we compare our results with those obtained using random-phase with exchange (RPAE) calculations by Amusia *et al.* [136] for the monopole and quadrupole $3p \leftarrow 2p$ and the dipole $3s \leftarrow 2p$ transitions. Note that the cross sections have been rotationally averaged. Overall, the agreement is very good, with the only notable discrepancy occurring for the dipole $3s \leftarrow 2p$ transition, where the low-q peak in our calculations is marginally shifted to lower values of q compared to Amusia *et al.* [136], although the height and width of the peak agree almost perfectly. The Amusia *et al.* calculations [136] have been compared to the recent IXS experiments by Zhu *et al.* [29], and the agreement for the monopole $2p^5 3p[1/2]_0$, the dipole $2p^5 3s[1/2]_1$, and the quadrupole $2p^5 3p[5/2,3/2]_2$ were found to be quite good, which carries over to our present calculations.

Ne	E_{exp} (eV)	E_{calc} (eV)	ΔE (%)
$2s2p^5 3s\ [1/2]_1$	16.715	16.554	1.0
$2s2p^5 3p\ [1/2]_0$	18.555	18.290	1.4
$2s2p^5 3p\ [3/2]_2$	18.704	18.720	0.1

TABLE 4.2: The energies E_{calc} for excited states in Ne atom calculated using CASSCF(9,10)/aug-cc-PVTZ. The percentage error, ΔE, relative experimental values E_{exp} from NIST [140] is also given.

C and Na

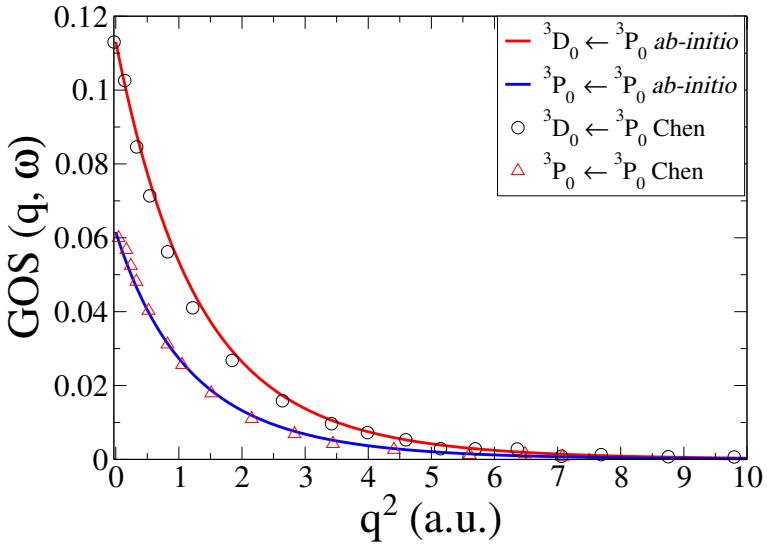

FIGURE 4.5: The generalized oscillator strengths, $GOS(q,\omega)$, in C for the two transitions ${}^3P_0\,(2s2p^3) \leftarrow {}^3P_0\,(2s^22p^2)$ and ${}^3D_0\,(2s2p^3) \leftarrow {}^3P_0\,(2s^22p^2)$. The current *ab-initio* calculations using CASSCF(5,6)/aug-cc-PVTZ are compared to RPAE calculations by Chen and Msezane [144].

Next we consider two open-shell atoms, C and Na. In this case, the electronic configuration of these systems allows to interpret how inner-shell transitions and different multiplicities can be studied using our method. Energy convergence is good considering that we treat excitations that involve a reordering of the atomic inner electrons. Electron correlation will play an important role in this case, due to the fact that unpaired electrons suffer a

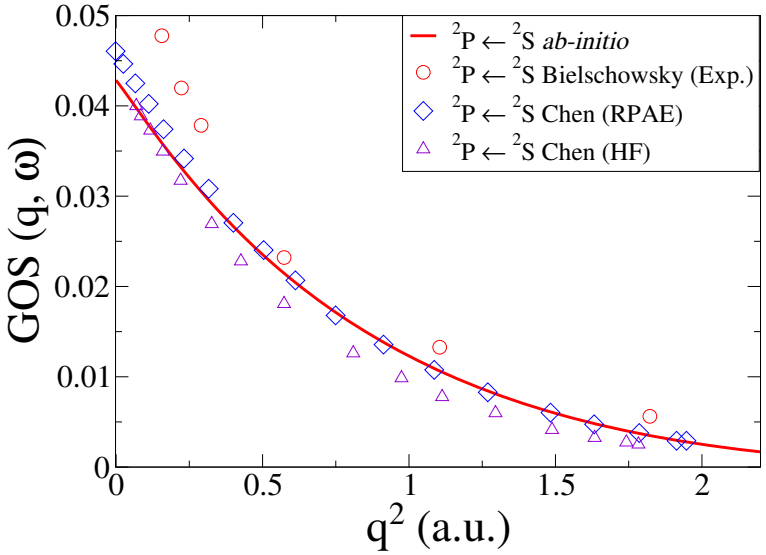

FIGURE 4.6: The generalized oscillator strength, $GOS(q,\omega)$, in Na for the $^2P\,([He]2s^22p^53s^2) \leftarrow {}^2S\,([He]2s^22p^63s)$ transition. The *ab-initio* calculations using CASSCF(9,11)/aug-cc-PVQZ are compared to experiments by Bielschowsky [145] and theory by Chen and Msezane [144].

bigger dynamic correlation than closed-shell electrons, requiring corrections by procedures such as CASPT2. Calculations are done at the CASSCF/aug-cc-PVTZ level and the energy convergence is shown in Table 4.3.

The IXS cross sections for the transitions from the ground state of the C atom to the first two inner-shell excited states, i.e. $^3P\,([He]2s2p^3) \leftarrow {}^3P\,([He]2s^22p^2)$ and $^3D\,([He]2s2p^3) \leftarrow {}^3P\,([He]2s^22p^2)$, are shown in Fig. 4.5. Our *ab-initio* calculations agree well with the RPAE calculations by Chen and Msezane [144], also included in Fig. 4.5. For $q^2 \rightarrow 0$ the GOSs should converge to the optical oscillator strength of the transitions. In our calculations these values are 0.0615 and 0.1130, respectively, which agrees reasonably well with the experimental values of 0.0634 and 0.0718 [146], as well as previous theory [144].

In Na, we have performed the *ab-initio* calculations at the CASSCF(9,11)/aug-cc-PVQZ level of theory. We consider an inner shell excitation from the doublet ground state, i.e. the $^2P\,([He]2s^22p^53s^2) \leftarrow {}^2S\,([He]2s^22p^63s)$ transition, which has a very low oscillator strength

Atom [state]	E_{exp} (eV)	E_{calc} (eV)	ΔE (%)
C $[2s2p^3\,{}^3P]$	9.330[140]	9.576	2.6
C $[2s2p^3\,{}^3D]$	7.946[140]	7.410	6.7
Na $[2p^5 3s^2\,{}^2P]$	31.200[145]	31.489	0.9

TABLE 4.3: The energies E_{calc} for excited states in atoms C and Na calculated at the CASSCF/aug-cc-PVTZ level of theory (see text for details). The percentage error, ΔE, compared to experimental values E_{exp} from NIST [140] and Bielschowsky *et al.* [145] is also given.

compared to outer electron excitations. The cross sections, shown in Fig. 4.6 compare well to previous theory at the HF and RPAE level [144] and EELS experiments by Bielschowsky *et al.* [145].

4.4.4 Molecules

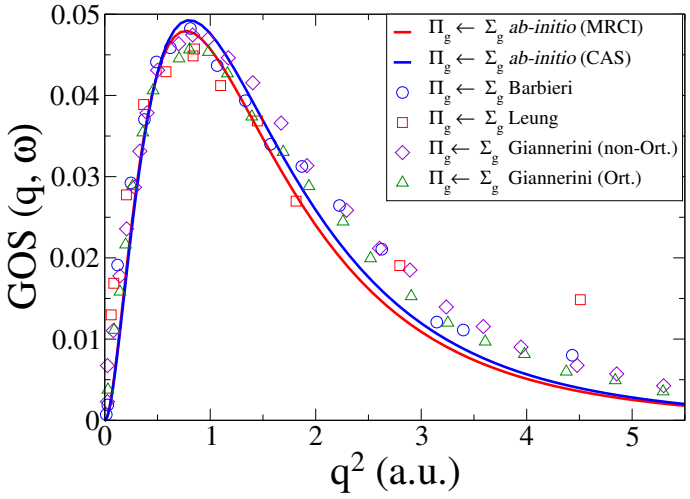

FIGURE 4.7: The generalized oscillator strength, $GOS(q,\omega)$, for the $a\,{}^1\Pi_g \leftarrow X\,{}^1\Sigma_g^+$ transition in N_2. Our CASSCF and MRCI *ab-initio* results are compared to experimental results from Leung *et al.* [147] and Barbieri *et al.* [148], and to calculations by Giannerini *et al.* [149].

The most important case we are treating in this chapter will correspond to the calculation of inelastic X-ray scattering cross sections in molecules.

N_2	E (eV)	ΔE (%)
Exp. [147]	9.300	–
CASSCF(14,12)	9.332	0.3
MRCI(14,10)	9.700	4.3

TABLE 4.4: The energy E for the $a\,^1\Pi_g$ state in N_2, corresponding to the transition energy from the $X\,^1\Sigma_g^+$ ground state. The experimental result is taken from Leung *et al.*[147]. *Ab-initio* CASSCF(14,12) and MRCI(14,10) results are shown, using the Dunning Rydberg-adapted aug-cc-PVCTZ basis. The percentage error, ΔE, compared to the experimental value is also given.

We have considered the nitrogen molecule, N_2, which has a great importance as one of the main components of our atmosphere. We concentrate on the Lyman-Birge-Hopfield band, which is probed by dipole forbidden transitions at 9.3 eV. Previous studies have been done using the quadrupole transition, $a\,^1\Pi_g \leftarrow X\,^1\Sigma_g^+$, which is unavailable to standard spectroscopic measurements.

Chung and Ling [150] started the studies on this band in the 1970s with their work using wavefunctions obtained using Hartree-Fock methods, followed by the Tamm-Dancoff approximation (TDA) and random-phase approximation (RPA) calculations by Szabo and Ostlund [139]. Several other theoretical approaches have been applied through the years trying to account for the inelastic scattering behaviour of this transition [149, 151] which has also been studied extensively experimentally [129, 130, 147, 148, 152].

A detailed analysis of TD-DFT theory and experiments in Ref. [130], shows further that the $a\,^1\Pi_g \leftarrow X\,^1\Sigma_g^+$ transition occurs in a region where there are additional contributions from the octupolar $w\,^1\Delta_u \leftarrow X\,^1\Sigma_g^+$ transition in the experimental signal, although in the following we focus on the transition to the $a\,^1\Pi_g$ state.

The energy for the transition obtained using SA-CASSCF(14,12)/aug-cc-PVCTZ is within 0.3 % of the experimental [147] value. Table 4.4 shows the experimental and theoretical energies E for the $a\,^1\Pi_g$ state in N_2, as well as the percentage error, ΔE, compared to experimental values from Leung

[147]. Also included are the results for a MRCI(14,10)/aug-cc-PVCTZ calculation, which in principle should perform better than CASSCF, but due to convergence problems had to be run at lower symmetry which adversely affected the energy convergence.

The generalized oscillator strength, $GOS(q, \omega)$, that we have calculated is in good agreement with the experimental results from Leung *et al.* [147] and Barbieri *et al.* [148], shown in Fig. 4.7, as well as recent theoretical calculations by Giannerini [149]. The MRCI results provide a slightly lower scattering cross section, but the difference is small. The experimental EELS signal differs from the IXS signal at large values of q. Bradley *et al.* [129] have identified deviations from first Born approximation scattering in the EELS signal at high q by comparison to IXS, along the lines of similar observations in Ne discussed earlier. As electrons are charged particles, several interactions can occur when it scatter from the system, however, the treatment is reduced to a single event. The effect of multiple scattering events is even larger when large values of q are considered and for this reason our calculated cross sections show a small deviation at large values q when compared to experimental cross-sections. The difference between our results and the experimental cross-sections can also be due to additional contributions from the $w\,^1\Delta_u$ state in the Lyman-Birge-Hopfield band [130].

4.4.5 Computational times and scaling with basis sets

We examine briefly the scaling properties of the IXS code with respect to the basis sets used to calculate the *ab-initio* electronic wavefunction. As mentioned in Sec. 4.2 the Gaussian products are Fourier transformed to calculate the X-ray scattering structure-factor, $s(\vec{q}, \omega)$. The number of Gaussian products will be directly related to the size of basis sets as shown in Table 4.5.

Table 4.5 shows the accuracy given by each basis set in the calculation of *ab-initio* electronic wavefunctions using the $^1S_0\,(2s) \leftarrow^1 S_0\,(1s)$ transition energy. The accuracy of the wavefunction will be the critical parameter in order to obtain reliable IXS matrix elements, as shown in Sec. 4.4. The scalability with the number of Gaussian products, N_{gp}. The number of Gaussians

H	$^1S_0\,(2s) \leftarrow^1 S_0\,(1s)$ IXS			
	ΔE (%)	N_g	N_{gp}	Speed-up
PVDZ	1	15	900	23
PVQZ	0.5	74	2.3×10^4	14
PV5Z	0.2	140	8×10^4	3
d-PV5Z	0.2	175	1.3×10^5	2.3
PV6Z	0.1	194	1.5×10^5	1.3
d-PV6Z	0	229	2×10^5	1

TABLE 4.5: Speed-up for the IXS matrix element of the transition $^1S_0\,(2s) \leftarrow^1 S_0\,(1s)$ state in H atom calculated at the CASSCF(1,3) level with Pople and Dunning basis sets: 3-21G, 6-311G, aug-cc-PVDZ, aug-cc-PVQZ, aug-cc-PV5Z, d-aug-cc-PV5Z, aug-cc-PV6Z, d-aug-cc-PV6Z. The energy percentage error, ΔE, compared to larger basis set (d-aug-cc-PV6Z) is also given. We show the number of Gaussians (N_g) used to calculate the *ab-initio* electronic wavefunctions and the number of Gaussian products (N_{gp}) used in the calculation of IXS matrix elements. The speed-up is calculated with respect to the amount of time necessary to obtain the IXS matrix elements with the largest basis set (d-aug-cc-PV6Z)

.

will determine not only the accuracy of the wavefunction but also the time required to calculate the IXS matrix elements. The speed-up is calculated for several basis sets, showing a compromise between accuracy and computer resources. The results are presented for a single-electron atom but the general trend is the same for multi-electron atoms and molecules.

In table 4.6 we have compared the integrated IXS matrix elements for the ${}^1S_0\,(2s) \leftarrow {}^1\,S_0\,(1s)$ transition in H atom, calculated using different basis sets. To benchmark the calculation we have used the analytical result given by the treatment explained in Sec. 5.2.2. The trend is clear, the number of Gaussian functions used to obtain the *ab-initio* electronic wavefunction has a direct influence in the goodness of the results. Nevertheless, in the case of Rydberg-like states the inclusion of extra-diffuse basis sets allows a better description of the IXS matrix elements, as can be seen for instance when we use diffuse Dunning basis sets, d-aug-cc-PV5Z and d-aug-cc-PV6Z, in the present calculation.

4.5 Conclusions

In this Chapter we have shown how the IXS cross-sections can be calculated using multiconfigurational *ab-initio* wavefunctions in atoms and molecules. The agreement of our results with experimental and theoretical reference values is excellent, validating our theoretical procedure and computer code for calculating IXS matrix elements. Via calculations in a wide range of atomic and molecular systems, we have demonstrated how the vast range of *ab-initio* possibilities can be treated and adapted to the scattering problem. From R-matrix [129, 130, 136] to time-dependent DFT [151] calculations, we have compared our results with other methods, showing a great agreement with them in terms of energies and quality of scattering matrix elements. Also, we have introduced the deep analogies between X-ray and electron scattering to reproduce experimental obervations from both electron (EELS) and X-ray (IXS) scattering. In terms of the range systems studied, different number of electrons, multiplicities and angular momenta considered using

H	$^1S_0\,(2s) \leftarrow^1 S_0\,(1s)$ IXS			
	I	N_g	N_{gp}	$\%\Delta I$
Analytical	0.3419	–	–	–
PVDZ	0.0404	15	900	18.3
PVQZ	0.0360	74	2.3×10^4	5.3
PV5Z	0.3471	140	8×10^4	1.4
PV6Z	0.3434	194	1.5×10^5	0.6
d-PV5Z	0.3402	175	1.3×10^5	0.5
d-PV6Z	0.3421	229	2×10^5	0.4

TABLE 4.6: Comparison of the integrated IXS matrix element for the $^1S_0\,(2s) \leftarrow^1 S_0\,(1s)$ transition in H atom calculated at the CASSCF(1,3) level with Dunning basis sets: aug-cc-PVDZ, aug-cc-PVQZ, aug-cc-PV5Z, d-aug-cc-PV5Z, aug-cc-PV6Z, d-aug-cc-PV6Z. The quality of the IXS matrix elements is benchmarked against analytical results given by the approximation made in Sec. 5.2.2. $\%\Delta I$ shows the percentage difference between the numerical and the analytical data.

.

our approach, providing insight into on how these features influence calculated results and how we can exploit the *ab-initio* electronic structure software to obtain the best results.

Importantly, we have demonstrated that the quality of IXS matrix elements directly relates to the quality of the wavefunction. For instance, an accurate calculation of the diffuse parts of the wavefunction (i.e. at large values of r) is important for the calculation of X-ray scattering matrix elements, in particular at low q. For this reason, highly accurate wavefunction calculations such as the R-matrix method produce reliable IXS matrix elements. Nevertheless, the accuracy achieved by our code and the *ab-initio* electronic wavefunctions calculated is comparable to methods such as RPAE [136] or the usage of explicitly correlated wavefunctions [141].

In later chapters we will study phenomena such as the non-adiabatic transfer population or the nuclear dynamics; the ability of our method to explain all the possible features in a molecular description will allow us to expand the treatment even to the spin-orbit coupling limit. The link between IXS and EELS also suggests that the code developed here could be useful for detailed analysis of ultrafast electron diffraction (UED) data, as long as the nuclear-scattering contribution is included in the elastic terms [153]. Future extensions of this work would be to include the effect of nuclear motion in the IXS signal, as we have recently done for elastic scattering [1, 2], and to consider Compton ionization by the inclusion of continuum states either via multichannel quantum defect formalism [154–156] or a Dyson orbital approach [157]. We also aim to examine in greater detail the mapping of the wavefunction in momentum space made possible by inelastic measurements.

Chapter 5

Hydrogen atom wavepacket dynamics

5.1 Introduction

The higher intensity and short X-ray pulse duration achieved by new sources of X-rays such as XFELs permit time-resolved X-ray studies in atoms and molecules [64, 158, 159]. In this chapter we will study the time evolution of an electronic wavepacket in an H-atom using X-ray scattering. The H-atom is excited into a coherent superposition of electronic states, i.e. a wavepacket, using a pump electromagnetic pulse. The subsequent time-evolution of this excited wavepacket is probed using non-resonant X-ray scattering.

The evolution of electronic wavepackets in hydrogen atoms using X-ray scattering has been studied widely from a theoretical perspective [11–13, 23, 24]. The purpose of this Chapter is to test the theory and methodology developed in Sec. 2.6 using analytical hydrogen wavefunctions. The calculations are carried out along the lines of the pioneering work of Dixit, Vendrell and Santra in Ref. [24] with a special interest on the influence of IXS in the general time-resolved X-ray scattering picture.

5.2 Theory

5.2.1 Time-resolved X-ray Scattering

The main theory of time-resolved scattering has been discussed in Sec. 2.6. A coherent superposition of states is excited using an optical pulse and then is probed using X-ray scattering at different delay times. To calculate the time-dependent differential scattering cross-section we use Eq. (2.70). It reads,

$$\begin{aligned}\frac{d\sigma}{d\Omega} = \frac{1}{2\pi}\left(\frac{d\sigma}{d\Omega}\right)_{\text{Th}} \int_0^\infty I(t) \sum_{ijf} c_i^* c_j e^{-\imath(E_j-E_i)t/\hbar} \\ \langle\psi_i|\hat{L}|\psi_f\rangle^* \langle\psi_f|\hat{L}|\psi_j\rangle \int d\omega_{\vec{k}_s} F\left(\omega_{\vec{k}_s} + \frac{1}{\hbar}\left(E_f - \frac{E_i+E_j}{2}\right)\right),\end{aligned} \tag{5.1}$$

where we have expressed the atomic wavefunction as a coherent superposition of states, i.e. a wavepacket,

$$|\Psi(\boldsymbol{r},t)\rangle = \sum_i c_i e^{\imath E_i t/\hbar} |\psi_i(\boldsymbol{r})\rangle. \tag{5.2}$$

The implementation of Eq. (5.1) requires the integration of the power spectrum function, $F\left(\omega_{\vec{k}_s} + \frac{1}{\hbar}\left(E_k - \frac{E_i+E_j}{2}\right)\right)$, which can be done using the procedure explained in Sec. 2.7, yielding,

$$W_{fij}(\Delta\omega) = \int_{\omega_0-\Delta\omega}^{\omega_0+\Delta\omega} F(\omega_s \pm \omega_{fij}) d\omega_s, \tag{5.3}$$

which follows directly from the Waller-Hartree approximation applied to Eq. (5.1). Previous studies [23, 24, 160] set the power spectrum value as a constant. However, when the Waller-Hartree approximation is applied, we establish that a discrete number of photons are taking part in the scattering process. This is the reason to consider that only the photons in the vicinity of ω_{k_0} are scattered by the system. Consequently the value of $\Delta\omega$ will set the level of energy interval and the detection range.

Inserting Eq. (5.3) into Eq. (5.1) yields,

$$\frac{d\sigma}{d\Omega} = \frac{1}{2\pi}\left(\frac{d\sigma}{d\Omega}\right)_{\mathrm{Th}} \int_0^\infty \sum_{ijf} c_i^* c_j e^{-\imath(E_j-E_i)t/\hbar} \int_{-\infty}^{\infty} I(t)dt \times L_{fi}^* L_{fj} W_{ijf}(\Delta\omega) d\omega_{k_s}, \tag{5.4}$$

where f goes to infinity, and i and j are the wave packet indexes. The scattering matrix elements, L_{if} and L_{fj}, take the form $\langle i|\hat{L}|f\rangle$, where $\hat{L}$ is the scattering operator.

5.2.2 Scattering matrix elements

The calculation of scattering matrix elements, $L_{\alpha\beta}$, using *ab-initio* electronic wavefunctions has been discussed in detail in Ch. 4. However, as studying the H atom, the calculation of the scattering matrix elements can be done analytically. The scattering matrix elements, $L_{\alpha\beta}$, are defined as,

$$L_{\alpha\beta} = \langle \psi_\alpha(\boldsymbol{r})|\hat{L}|\psi_\beta(\boldsymbol{r})\rangle \tag{5.5}$$

where $\psi_\alpha(\boldsymbol{r})$ and $\psi_\beta(\boldsymbol{r})$ are the two wavefunctions involved in the scattering event. We can divide any wavefunction in radial, $R_{nl}(\boldsymbol{r})$ and angular parts, $Y_{lm}(\theta,\phi)$,

$$\psi_{nlm}(\boldsymbol{r}) = R_{nl}(\boldsymbol{r})Y_{lm}(\theta,\phi) \tag{5.6}$$

where $Y_{lm}(\theta,\phi)$ are spherical harmonics that depend on the quantum numbers l and m while n is the principal quantum number. The radial wavefunctions for the H-atom are known analytically. They read,

$$R_{nl}(r) = \sqrt{\frac{(n-l-1)!}{2n[(n+l)!]}}\left(\frac{2Z}{na_0}\right)^{l+3/2} r^l e^{-\frac{Zr}{na_0}} L_{n-l-1}^{2l+1}\left(\frac{2Zr}{na_0}\right), \tag{5.7}$$

where Z is the charge of the nuclei, 1 in the case of H, r is the radial distance, a_0 is the Bohr radius and L_{n-l-1}^{2l+1} are the Legendre polynomials. The $\hat{L}$ operator from Eq. (5.4), defined as $\hat{L} = \sum_j e^{-\imath\vec{q}\vec{r}_j}$, can be expanded in partial

waves using the Wigner-Eckart theorem,

$$e^{-\imath\vec{q}\vec{r}} = 4\pi \sum_{l=1}^{\infty} \sum_{m=-l}^{m=l} \imath Y_{lm}^{*}(\theta,\phi) B_l(\vec{q}r) Y_{lm}(\theta_{\vec{q}},\phi_{\vec{q}}) \tag{5.8}$$

where $\theta_{\vec{q}}$ and $\phi_{\vec{q}}$ define the position of the momentum transfer vector $\vec{q}$ in the laboratory frame and B_l is the spherical Bessel function of the product $\vec{q}\vec{r}$,

$$B_l(\vec{q}\vec{r}) = 2^l (\vec{q}\vec{r})^l \sum_{k=0}^{\infty} \frac{(-1)^k (k+l)!}{k!(2k+2l+1)!} (\vec{q}\vec{r})^{2k}. \tag{5.9}$$

Inserting Eqs. (5.14) and (5.8) in Eq. (5.4) yields,

$$\begin{aligned} L_{\alpha\beta}(\vec{q}) = 4\pi Y_{l_{\vec{q}} m_{\vec{q}}}(\theta_{\vec{q}},\phi_{\vec{q}}) \sum_{k=0}^{N_{el}} \sum_{l=|l_\alpha - l_\beta|}^{|l_\alpha + l_\beta|} \int_0^{\infty} R_{n_\alpha l_\alpha}(\vec{r}_k) B_l(\vec{q}\vec{r}_k) R_{n_\beta l_\beta}(\vec{r}_k) d\vec{r}_k \\ \int\int Y_{l_\alpha m_\alpha}(\theta,\phi) Y_{l_\beta m_\beta}(\theta,\phi) Y_{lm}(\theta,\phi) \sin\theta d\theta d\phi, \end{aligned} \tag{5.10}$$

where the integral over $\vec{r}$ is the so-called *Bessel transformation*. The integration over spherical harmonics is performed using the Wigner-Eckart theorem and its relationship with Clebsch-Gordan coefficients,

$$\begin{aligned} &\int\int Y_{l_\alpha m_\alpha}(\theta,\phi) Y_{l_\beta m_\beta}(\theta,\phi) Y_{lm}(\theta,\phi) d\theta d\phi = \\ &= \sqrt{\frac{(2l_\alpha+1)(2l_\beta+1)}{4\pi(2l+1)}} \langle l_\alpha l_\beta 00 | l_\alpha l_\beta l 0\rangle \langle l_\alpha l_\beta m_\alpha m_\beta | l_\alpha l_\beta l m\rangle. \end{aligned} \tag{5.11}$$

5.3 Results

5.3.1 The $3d_0$-$4f_0$ wavepacket

In the following we discuss the results obtained when the time-evolution of a two-level wavepacket is measured in H atom using X-ray scattering. We have chosen the $3d_0$ and $4f_0$ electronic states of H to construct the wavepacket (see Fig. 5.1) in order to compare to Ref. [24]. The population of the $3d$ and $4f$ states is considered equal for simplicity and the bandwidth

of the X-ray pulse, represented by $W_{ijk}(\Delta\omega)$ from Eq. (5.4), is chosen to be small enough to couple states up to $n = 11$. The scattering patterns are shown using polar detector images as a function of θ (radial detection coordinate) and ϕ (angular detection coordinate) angles with $q_{max} = 3.5$. The evolution of the system will be probed at a range of different time windows, $(t - \tau)$, by the X-ray pulse. In Eq. (5.4) the intensity of the X-ray, $I(t)$, will be centered at each different pump-probe delay, τ. The envelope of the X-ray pulse, E, is represented by using a Gaussian function of the form,

$$E(t - \tau) = E_0 e^{\frac{(t-\tau)}{\gamma^2}}, \tag{5.12}$$

where E_0 is the amplitude of the pulse, t the time, τ the pump-probe time delay and γ the width of the envelope. The intensity of the pulse, $I(t)$, will be proportional to the square of the pulse envelope, E, in Eq. (5.12), $I(t) \propto (E(t - \tau))^2$. In this simulation we set $E_0^2 = 10^{14}$ W/cm^2 and $\gamma = 1$ fs.

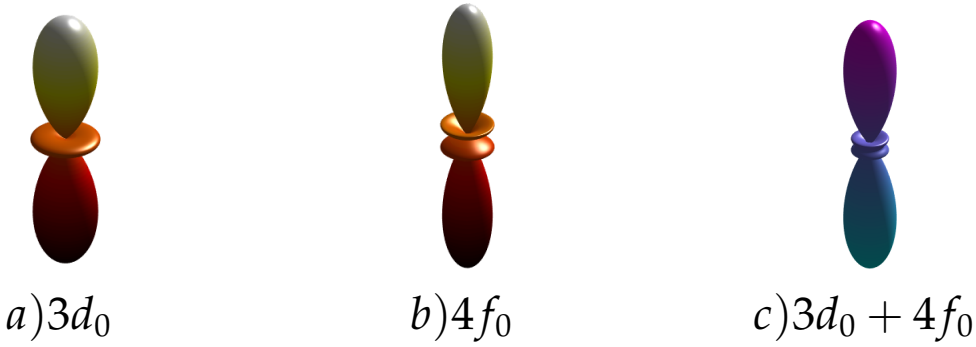

FIGURE 5.1: Representation of the shape of the electronic wavefunction. We show the isosurface of the real valued part for a) $3d_0$ ($R_{32}Y_{20}$), b) $4f_0$ ($R_{43}Y_{30}$) and c) the coherent superposition of the two. The cutoff for the isosurface is 1.0.

The first situation considered in our calculations is the one expressed by Eq. (5.4). An infinite number of states are included via the identity operator, $\mathbb{1} = \sum_f |f\rangle\langle f|$, coupling all possible levels in the atom with the non-stationary wavepacket formed by the coherent superposition of $3d_0$ and $4f_0$ electronic states.

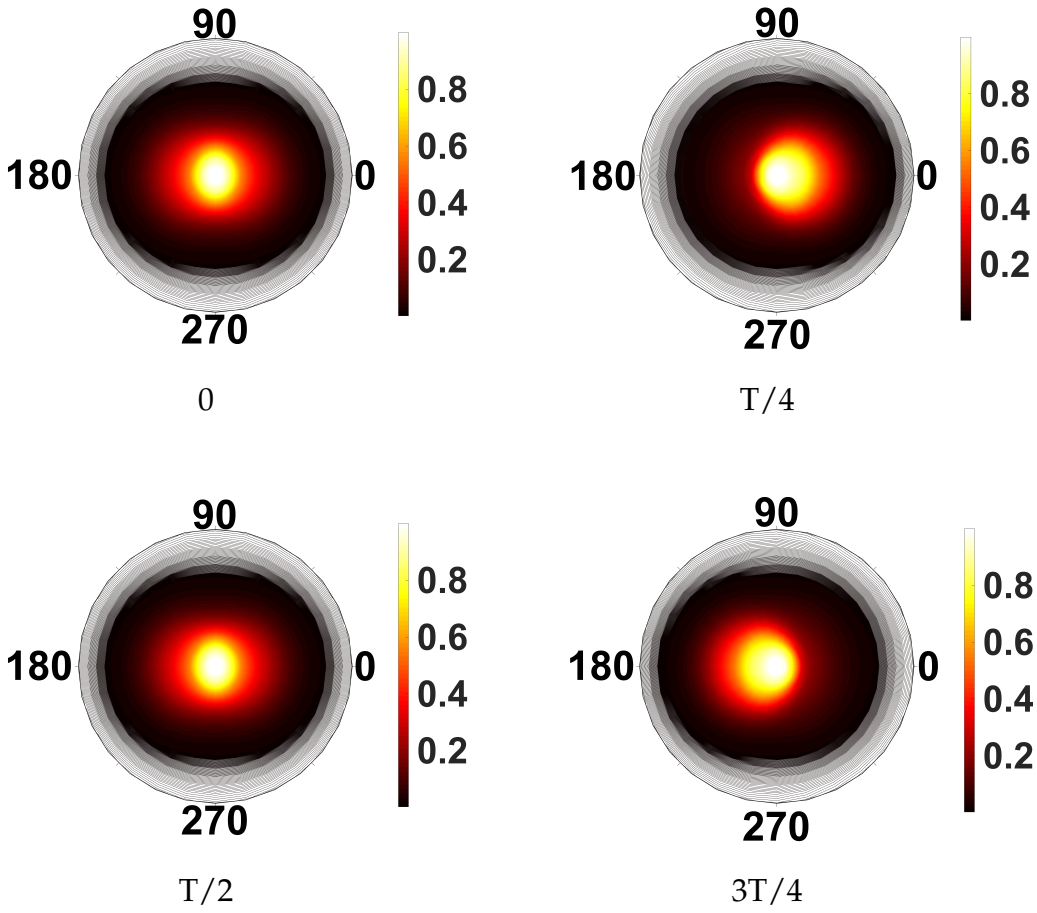

FIGURE 5.2: X-ray scattering signals for the wavepacket corresponding to the coherent superposition of $3d_0$ and $4f_0$ electronic states in H atom. The scattering patterns are represent at different pump-probe delay times 0, $T/4$, $T/2$, $3T/4$ where T is the period of the electronic wavepacket, $T = 2\pi/\Delta E = 6.27$ fs. The X-ray is chosen to be parallel to y direction and q_{max}=3.5 a.u. in all four figures.

Fig. 5.2 shows the evolution of the X-ray scattering signal at different pump-probe delay times. The period, T, is calculated using the energy difference $\Delta E = E_4 - E_3$,

$$T = \frac{2\pi}{\Delta E} = 6.27 \text{ fs}. \tag{5.13}$$

The time-dependent scattering patterns in Fig. 5.2 match the expected non-stationary wavepacket behaviour, representing almost perfectly the shape of the electronic charge distribution in the wavepacket. Our calculation agrees perfectly with the calculated scattering patterns in Ref. [24]. This demonstrates that the inclusion of IXS terms, $L_{\alpha\beta}$, in the general time-dependent X-ray scattering formula produces the correct physical behaviour of the wavepacket.

When only the influence of the electron density is considered to calculate the scattering pattern, i.e. elastic scattering , the time-dependent behaviour is not reflected in the final signal. Eq. (5.4) is simplified to a great extent when only the elastic scattering terms i.e $L_{\alpha\alpha}$, are considered. It yields,

$$\frac{d\sigma}{d\Omega} = \frac{1}{2\pi}\left(\frac{d\sigma}{d\Omega}\right)_{\text{Th}} \int_0^\infty \int_{-\infty}^\infty \sum_i c_i^2 I(t) L_{ii}^2 dt. \tag{5.14}$$

In Fig. 5.3 we show the result of Eq. (5.4) applied to the coherent superposition of $3d_0$ and $4f_0$ states. The wavepacket oscillations are not reflected in the scattering pattern as the elastic scattering elements do not contain any time-dependent information. This behaviour only appears when atomic systems are considered; as discussed in Ch. 6, the nuclear wavepackets in molecules contain time-dependent information that is not removed when the elastic approximation is applied.

5.3.2 The $3d_1$-$4f_3$ wavepacket

The second case that we consider is the scattering pattern from a coherent superposition of $3d_1$ and $4f_3$ hydrogen atom states. The wavepacket is analogous to the one employed in Sec. 5.3.1, only the m quantum numbers are changed. The shape of the spherical harmonics forming the wavepacket is different (see Fig. 5.4), resulting in a change in the scattering patterns. The

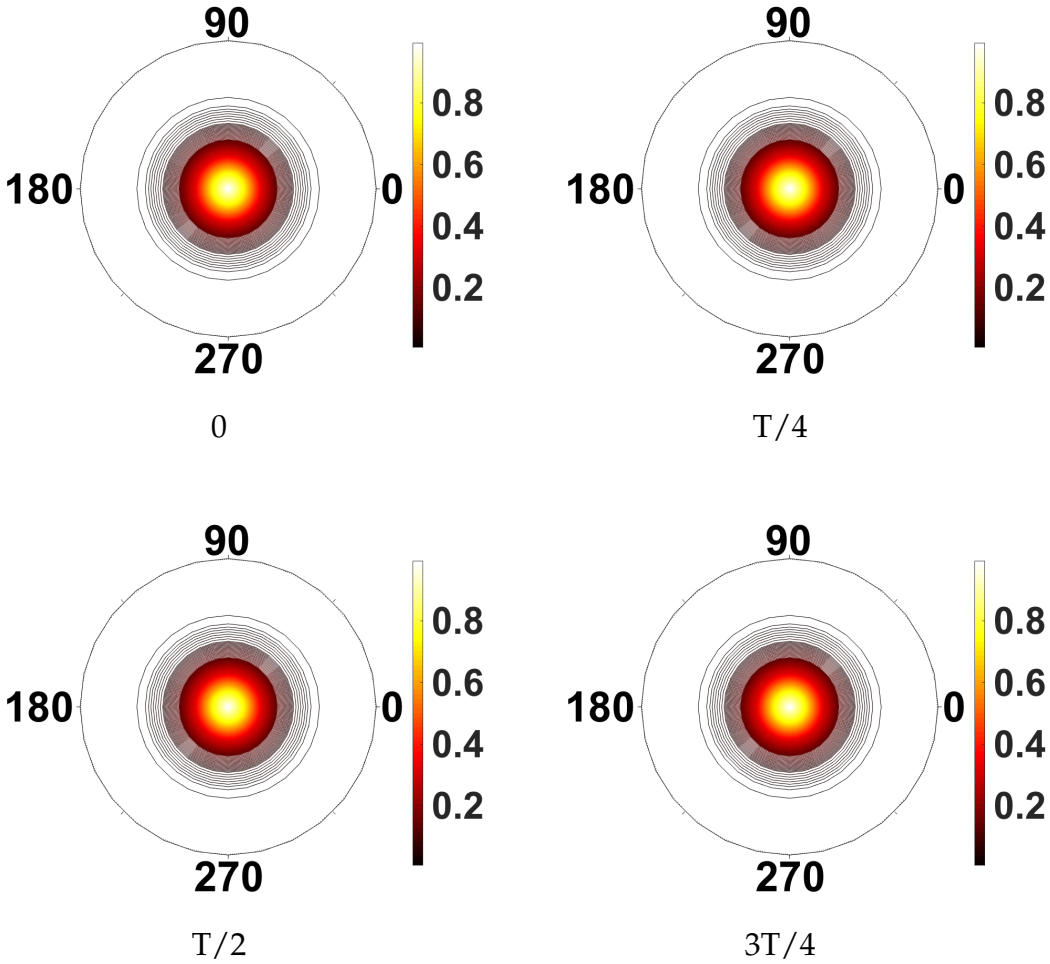

FIGURE 5.3: Elastic X-ray scattering signals for the wavepacket corresponding to the coherent superposition of $3d_0$ and $4f_0$ electronic states in H atom. The scattering patterns are represent at different pump-probe delay times 0, $T/4$, $T/2$, $3T/4$ where T is the period of the electronic wavepacket, $T = 2\pi/\Delta E = 6.27$ fs. The X-ray is chosen to be parallel to y direction and q_{max}=3.5 a.u. in all four figures.

X-ray pulse specifications are the same as the ones employed in Sec. 5.3.1, as we are treating an analogous wavepacket in terms of energy. The period of the wavepacket also remains the same, $T = 6.27$ fs, since the energy in a hydrogen atom only depends on the principal quantum number n.

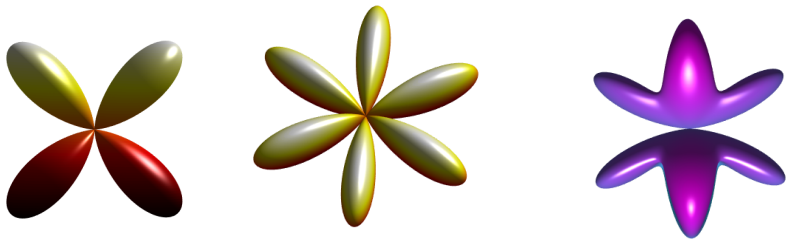

$a)3d_1$ $b)4f_3$ $c)3d_1 + 4f_3$

FIGURE 5.4: Representation of the shape of the electronic wavefunction. We show the isosurface of the real valued part for a) $3d_1$ ($R_{32}Y_{21}$), b) $4f_0$ ($R_{43}Y_{33}$) and c) the coherent superposition of the two. The cutoff for the isosurface is 1.0.

In Fig. 5.5 we show the scattering patterns of the coherent superposition of $3d_1$ and $4f_3$ electronic states in hydrogen at different pump-probe delay times. The oscillations of the wavepacket are reflected in the X-ray scattering signal, and the geometry of the spherical harmonics produces recognizable signatures in the scattering patterns (see Fig. 5.4). The scattering pattern at half the period, $T/2$, is not equal to the scattering at T as a direct consequence of the symmetry in the wavepacket, different from the $3d_0/4f_0$ superposition of states.

5.4 Conclusions

We have calculated time-resolved X-ray scattering in two H-atom electronic wavepackets. The wavepackets are formed by a coherent superposition of $3d$ and $4f$ electronic states, taking different values of m in each of the cases considered. The aim was to test the calculation of the time-dependent X-ray scattering patterns described by Eq. (5.4) and compare to the calculations of

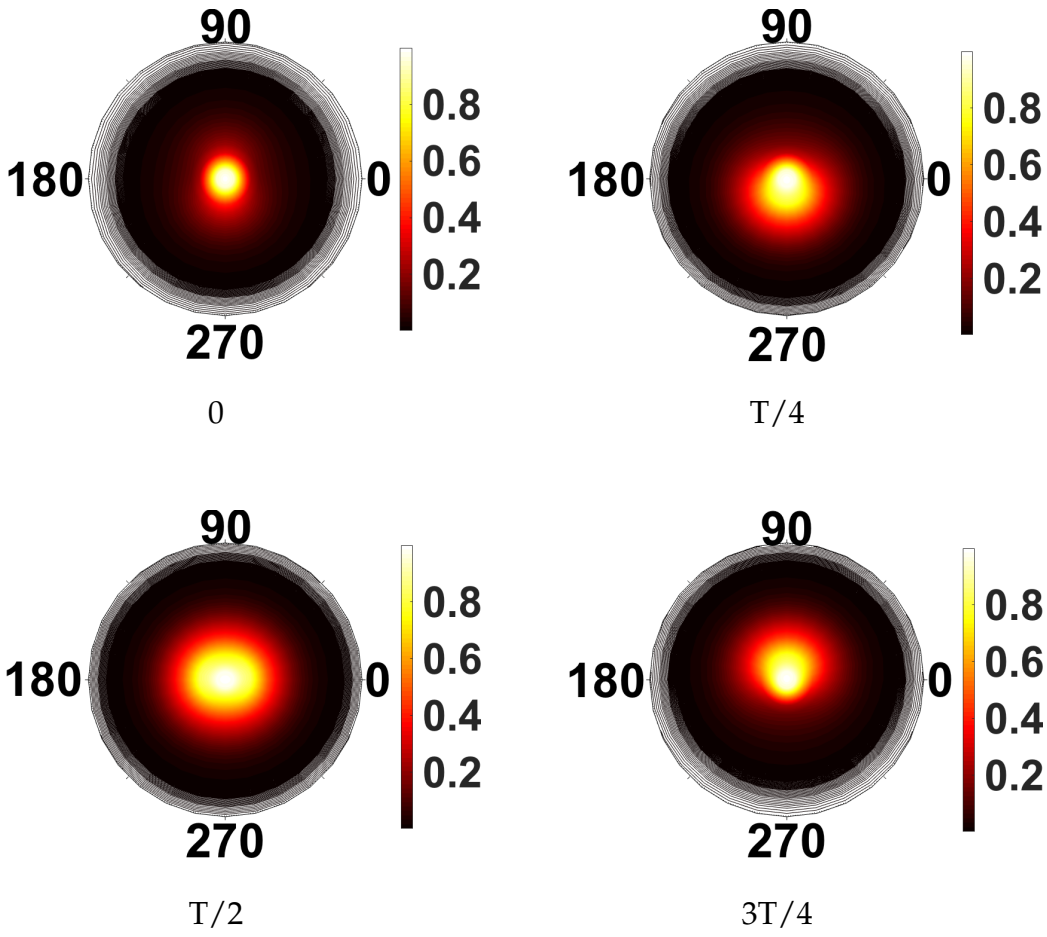

FIGURE 5.5: X-ray scattering signals for the wavepacket corresponding to the coherent superposition of $3d_1$ and $4f_3$ electronic states in H atom. The scattering patterns are represent at different pump-probe delay times 0, $T/4$, $T/2$, $3T/4$ where T is the period of the electronic wavepacket, $T = 2\pi/\Delta E = 6.27$ fs. The X-ray is chosen to be parallel to y direction and q_{max}=3.5 a.u. in all four figures.

Dixit *et al.* [24] and Simmermacher *et al.* [13]. Our calculated results agree very well with the calculated scattering patterns in Ref. [24], validating the quantum electrodynamics (QED) description developed in Sec. 2.7.

The oscillations of the wavepackets and their periods are reflected in the scattering patterns obtained using Eq. (5.4), showing a direct relationship between the X-ray scattering and the physical behaviour of the system. This demonstrates the importance of IXS in time-resolved X-ray scattering, since the elastic scattering terms do not produce any time-dependent signal and the IXS terms carry all temporal information (see Figs. 5.2 and 5.3).

The analytical H case, validated against Ref. [24], serves as a starting point in the study of time-resolved X-ray scattering. More complex atoms with larger number of electrons (and molecules) can be studied using the developed theory and the tool of *ab-initio* X-ray scattering presented in Ch. 4. We will see in the next Chapter that, in the molecular case, the consideration of non-stationary nuclear wavepackets diminishes these effects, although the inclusion of IXS in the scattering picture is still necessary (see discussion in Ch. 6).

Chapter 6

H_2 dynamics

6.1 Introduction

New X-ray sources such as X-ray Free-Electron Lasers, with higher intensity and shorter pulse duration than synchrotrons make it possible to study molecular dynamics using time-resolved X-ray scattering. An increasing number of experimental realisations of ultrafast scattering are emerging, both using X-rays [9, 21, 22] and the analogous ultrafast electron scattering (UED) technique [14, 34, 112]. So far, the experiments have been interpreted under the assumption that the scattering is purely elastic. As proposed by Cao and Wilson [23] and several other theoretical groups [13, 24, 26, 31], the dynamical behaviour of the system may require that inelastic scattering is included in the time-resolved X-ray picture, as demonstrated to dramatic effect for electronic wavepackets in hydrogen atoms (see discussion in Ch. 5 and Ref. [24]). In the following we apply the molecular time-dependent X-ray formalism developed in Ch. 2, which implicitly includes IXS.

The simulations are carried out using calculated *ab-initio* electronic wavefunctions in H_2. We consider a pump-probe scheme in which the time-evolution of an excited wavepacket is probed at different times by an X-ray pulse. The computational methods applied will be described in detail. We carry out quantum dynamics simulations to describe the evolution of the electronic and nuclear states of the molecule in time. The scattering signal is calculated using our *ab-initio* scattering code as described in Ch. 4 and the theory derived in Ch. 2.

6.2 Theory

6.2.1 Molecular time-dependent X-ray scattering

The treatment of molecular ultrafast X-ray scattering has been discussed in detail in Sec. 2.7. The time-dependent molecular wavefunction is expanded in nuclear and electronic parts using the Born-Huang expansion,

$$\Psi(\boldsymbol{r}, \boldsymbol{R}, t) = \sum_i \chi_i(\boldsymbol{R}, t)\psi_i(\boldsymbol{r}; \boldsymbol{R}), \tag{6.1}$$

where $\psi_i(\boldsymbol{r}; \boldsymbol{R})$ are the electronic wavefunctions and $\chi_i(\boldsymbol{R}, t)$ represent the nuclear wavefunctions. The electronic eigenfunctions depend only parametrically on the nuclear coordinate $\boldsymbol{R}$. In the present treatment we do not consider the rotational motion.

Inserting the expression for the time-dependent molecular wavefunction from Eq. (6.1) into the time-resolved X-ray scattering formalism yields,

$$\begin{aligned}\frac{d\sigma}{d\Omega} = \left(\frac{d\sigma}{d\Omega}\right)_{\text{Th}} \sum_{ijf} \int_0^\infty \int_{-\infty}^\infty I(t)\chi_i(\boldsymbol{R}, t)^* \chi_j(\boldsymbol{R}, t) dt \\ \times L_{fi}^* L_{fj} W_{ijf}(\Delta\omega) d\omega_{\boldsymbol{k}_s} d\boldsymbol{R},\end{aligned} \tag{6.2}$$

which is the expression for the molecular time-resolved differential-cross section developed in Sec. 2.7 (see Eq. (2.84)). We recall that scattering is a two-photon process, in which scattered photons produce $f \leftarrow i$ and $f \rightarrow j$ transitions. The nature of the process requires the consideration of an infinite range of f states as a direct consequence of the inclusion of electronic identity operator, $\mathbb{1} = \sum_f^\infty |f\rangle\langle f|$. The identity operator is *only* constructed in terms of electronic wavefunctions here, although it can include also vibrational and rotational states. Further details in the development of Eq. (6.2) are given in Sec. 2.7.

6.2.2 Molecular Hamiltonian: adiabatic and diabatic representations

In the following we discuss the representation of the electronic wavefunctions used in this Chapter. The Hamiltonian terms in the laboratory frame can be combined as follows,

$$\hat{H}_N = \hat{T}_N(\boldsymbol{R}) + \hat{H}_{elec}(\boldsymbol{R}, \boldsymbol{r}), \tag{6.3}$$

where we have expressed the nuclear kinetic energy term as $\hat{T}_N(\boldsymbol{R})$ and the remaining terms collected in $\hat{H}_{elec}(\boldsymbol{R}, \boldsymbol{r})$. The kinetic energy operator, $\hat{T}_N(\boldsymbol{R})$, for a diatomic can be expressed in polar coordinates as,

$$\hat{T}_N(\boldsymbol{R}) = -\frac{1}{2\mu}\left[\frac{1}{R^2}\frac{\partial}{\partial R}\left(R^2\frac{\partial}{\partial R}\right) + \frac{\hat{L}_N}{R^2}\right], \tag{6.4}$$

where μ is the reduced mass of the nuclei and $\hat{L}_N$ is the nuclear angular momentum operator.

Considering an stationary Born-Huang expansion analogous to Eq. (6.1) we can express the wavefunction as,

$$\Psi(\boldsymbol{r}, \boldsymbol{R}) = \sum_i^N \psi_i(\boldsymbol{r}; \boldsymbol{R})\chi_i(\boldsymbol{R}), \tag{6.5}$$

where N is the dimensionality of the electronic Hilbert space (i.e. the number of electronic states) and we have decomposed the total wavefunction into electronic, $\psi_i(\boldsymbol{r}; \boldsymbol{R})$, and nuclear wavefunctions, $\chi_i(\boldsymbol{R})$. The electronic wavefunctions, $\psi_i(\boldsymbol{r}; \boldsymbol{R})$, will be eigenfunctions of electronic Hamiltonian, $\hat{H}_{elec}(\boldsymbol{R}, \boldsymbol{r})$, defined in Eq. (6.3). Inserting Eq. (6.5) into Eq. (6.3) yields,

$$\begin{aligned}\hat{H}(\boldsymbol{r}, \boldsymbol{R})\Psi(\boldsymbol{r}, \boldsymbol{R}) &= \left(\hat{T}_N(\boldsymbol{R}) + \hat{H}_{elec}(\boldsymbol{r}, \boldsymbol{R})\right)\sum_i^N \psi_i(\boldsymbol{r}; \boldsymbol{R})\chi_i(\boldsymbol{R}) = \\ &= \sum_i^N \hat{T}_n(\boldsymbol{R})\psi_i(\boldsymbol{r}; \boldsymbol{R})\chi_i(\boldsymbol{R}) + \sum_i^N E_i^{elec}(\boldsymbol{R})\psi_i(\boldsymbol{r}; \boldsymbol{R})\chi_i(\boldsymbol{R}) = E_T\sum_i^N \psi_i(\boldsymbol{r}; \boldsymbol{R})\chi_i(\boldsymbol{R})\end{aligned} \tag{6.6}$$

where E_i^{elec} is the electronic (*ab-initio*) energy for state i and E_T the total energy. Multiplying both sides of Eq. (6.6) by the electronic wavefunctions, $\psi_j(\boldsymbol{r};\boldsymbol{R})$ and integrating over the electron coordinates, $\boldsymbol{r}$, yields,

$$(E_j^{elec}(\boldsymbol{R}) - E_T)\chi_j(\boldsymbol{R}) + \sum_j^N \langle\psi_j(\boldsymbol{r};\boldsymbol{R})|\hat{T}_N(\boldsymbol{R})|\psi_i(\boldsymbol{r};\boldsymbol{R}\rangle\chi_j(\boldsymbol{R}), \tag{6.7}$$

where we have reordered the terms using the orthonormality of the electronic wavefunctions and we use bracket notation for convenience. Ignoring the angular dependence of $\hat{T}_N(\boldsymbol{R})$ and invoking the Born-Oppenheimer approximation described in Ch. 1, the problem for a diatomic molecule is reduced to a single degree of freedom, the internuclear separation R. Inserting Eq. (6.4) into Eq. (6.7) leads to,

$$\left(E_j^{elec}(R) - E_T\right)\chi_j(R) - \frac{1}{2\mu}\sum_i^N \langle\psi_j(\boldsymbol{r};R)|\frac{1}{R^2}\frac{\partial}{\partial R}\left(R^2\frac{\partial}{\partial R}\right)|\psi_i(\boldsymbol{r};R)\rangle\chi_i(R) = 0, \tag{6.8}$$

which can be rearranged by multiplying -2μ and using the properties of the derivative,

$$\left[\frac{d^2}{dR^2} - 2\mu(E_j^{elec}(R) - E_T)\right]\chi(R) + \sum_i 2\underbrace{\langle\psi_j(r;R)|\frac{\partial}{\partial R}|\psi_i(\boldsymbol{r};R)\rangle}_{A_{ji}}\frac{\partial\chi(R)}{\partial R} + \underbrace{\langle\psi_j(\boldsymbol{r};R)|\frac{\partial^2}{\partial R^2}|\psi_i(\boldsymbol{r};R)\rangle}_{B_{ji}}\chi(R) = 0, \tag{6.9}$$

where A_{ji} and B_{ji} are the first and second derivative couplings respectively, also called non-adiabatic coupling elements (NACMEs). Non-adiabatic coupling elements are important in the treatment of avoided crossings or conical intersections as their magnitude will determine the probability of a crossing between coupled wavefunctions.

Eq. (6.9) can be expressed in a matrix form,

$$\left(\frac{d^2}{dR^2}\boldsymbol{I} - 2\mu(\boldsymbol{V}^{(ad)}(R) - \boldsymbol{E}) + \boldsymbol{B}(R)\right)\chi(R) + 2\boldsymbol{A}\frac{\partial\chi(R)}{\partial R} = 0, \tag{6.10}$$

where $\boldsymbol{I}$ is the identity matrix, $\boldsymbol{E}$ is the matrix of eigenvalues, $\boldsymbol{A}$ and $\boldsymbol{B}$ are the non-adiabatic coupling matrices and $\boldsymbol{V}^{(a)}$ is the diagonal matrix of eigenvalues of the electronic *ab-initio* Hamiltonian. Eq. (6.10) is known as *adiabatic representation*. In many instances, the propagation of the nuclear wavefunctions is simpler in a *diabatic representation*, in which the the new diabatic basis, will set the NACMEs to zero. The wavefunctions in this representation become,

$$\chi^{(\mathrm{d})}(R) = \boldsymbol{C}^{\dagger}(R)\chi(R), \tag{6.11}$$

$$\psi^{(\mathrm{d})}(\boldsymbol{r}; R) = \psi(\boldsymbol{r}; R)\boldsymbol{C}(R), \tag{6.12}$$

where the superscript (d) denotes the diabatic representation and $\boldsymbol{C}(R)$ is the unitary rotation matrix which relates both representations. As stated by Smith [161] and Dishoek *et al.* [162], $\boldsymbol{C}(R)$ can be calculated by using the first derivative coupling matrix, $\boldsymbol{A}$,

$$\frac{d\boldsymbol{C}}{d\boldsymbol{R}} + \boldsymbol{A}\boldsymbol{C} = 0, \tag{6.13}$$

which can be used in Eq. (6.10) yielding,

$$\left(\frac{d^2}{dR^2}\boldsymbol{I} - 2\mu(\boldsymbol{V}^{(\mathrm{d})}(R) - \boldsymbol{E})\right)\chi^{\mathrm{d}}(R) = 0, \tag{6.14}$$

which is the *diabatic representation* of the Schrödinger equation for a diatomic. Eq. (6.14) is useful when dynamics are calculated as it implicitly considers the non-adiabatic coupling between electronic wavefunctions. The diabatization procedure is based on Eq. (6.13), which assumes only one coordinate, but generalisations to more degrees of freedom exist.

6.2.3 Nuclear Propagation

The time-dependent X-ray scattering cross-section in Eq. (6.2) requires the propagation in time of the nuclear wavefunctions, $\chi(\boldsymbol{R}, t)$. The time-dependency of a quantum system can be studied by solving the time-dependent Schrödinger equation. It is represented as,

$$\imath\hbar\frac{d\chi(\boldsymbol{R}, t)}{dt} = \hat{H}\chi(\boldsymbol{R}, t). \tag{6.15}$$

where we have isolated the nuclear wavefunctions, $\chi(\boldsymbol{R}, t)$, from the Born-Huang expansion of the total wavefunction in Eq. (6.1). We will use a solve Eq. (6.15) using the so-called *split operator method* [101].

Briefly, this method allows the solution of the time dependent Schrödinger equation by splitting the propagator operator $\hat{U}(t, t_0)$ into a kinetic and a potential operator parts. Considering that the Hamiltonian is time-independent we can write the formal solution for the wavefunction as,

$$\Psi(t) = e^{-\imath\hat{H}t}\Psi(0) = e^{-\imath(\hat{T}+\hat{V})t}\Psi(0), \tag{6.16}$$

where $\Psi(0)$ is the initial guess of the wavefunction, $\hat{T}$ is the kinetic energy operator and $\hat{V}$ the potential energy operator. If we then represent the variation of the wavefunction, $\Psi(t)$, in one time step Δt it yields,

$$\Psi(t + \Delta t) = e^{-\imath\hat{H}\Delta t}\Psi(t) = e^{-\imath(\hat{T}+\hat{V})\Delta t}\Psi(t), \tag{6.17}$$

where we consider Δt as a infinitesimal period of time. Eq. (6.17) can be solved separating the Hamiltonian in $\hat{T}$ and $\hat{V}$ energy operators. However, as the potential and kinetic operators do not commute, the error produced is large and another procedure is required. We can diminish the error produced in the splitting by using the Baker-Campbell-Hausdorf theorem and Eq. (6.17). It yields an equation comparable with the original definition of the Hamiltonian with an associated error equal to $\hat{O}(\Delta t^3)$. It has the form,

$$\Psi(t + \Delta t) = e^{-\imath\hat{H}\Delta t}\Psi(t) \approx e^{-\imath\frac{\hat{T}}{2}\Delta t}e^{-\imath\hat{V}\Delta t}e^{-\imath\frac{\hat{T}}{2}\Delta t}\Psi(t), \tag{6.18}$$

where the Hamiltonian term, $e^{-\imath\hat{H}\Delta t}$, has been split in two half-kinetic operator exponentials, $e^{-\imath\frac{\hat{T}}{2}\Delta t}$, and one potential operator exponential, $e^{-\imath\hat{V}\Delta t}$. Dividing the potential energy operator in two equal parts will yield the same result.

The practical application of this method requires the usage of fast Fourier transformations for the operators $\hat{T}$ and $\hat{V}$ in their respective representations. The operator $\hat{T}$ is diagonal in the momentum space and, in turn, $\hat{V}$ is diagonal in the position space. The calculation of the time-dependent wavefunction will be then carried out using forward (momenta) and backward (position) fast Fourier transforms. If the kinetic operator is not diagonal in the momentum space other approaches must be used.

6.2.4 Scattering matrix elements

The procedure to calculate scattering matrix elements is explained in Ch. 4. In brief, the scattering matrix element, $L_{\alpha\beta}$, between two states, Ψ_α and Ψ_β, is represented as,

$$L_{\alpha\beta} = \langle\Psi_\alpha|\sum_i^{N_{el}} e^{-\imath\vec{q}\vec{r}}|\Psi_\beta\rangle, \tag{6.19}$$

where $\sum_i^{N_{el}} e^{-\imath\vec{q}\vec{r}}$ is the corresponding scattering operator, $\hat{L}$, with the sum running over the number of electrons in the system, N_{el}. The calculation of the matrix elements is carried out by Fourier transforming the multiconfigurational *ab-initio* electronic wavefunctions of the form,

$$|\Psi_\alpha(\mathbf{r};\boldsymbol{R})\rangle = \sum_{i=1}^{N_{\text{conf}}} c_{\alpha,i}\,|\Phi_{\text{SD}}^{\alpha,i}\rangle, \tag{6.20}$$

where the wavefunction, $\Psi_\alpha(\mathbf{r};\boldsymbol{R})$, depends parametrically on the nuclear coordinate, R, and is expanded in terms of Slater determinants, $|\Phi_{\text{SD}}^{\alpha,i}\rangle$. The representation of the wavefunction in terms of Gaussian functions allows the Fourier transformation to be calculated analytically as explained in Ch. 4.

6.3 Computational Details

The simulations performed to calculate time-resolved X-ray scattering from H_2 molecules are based on X-ray scattering codes written in our group [2, 84], while the dynamics simulations were done using the software package WAVEPACKET [30] with the *ab-initio* electronic structure calculations done using the *ab-initio* software package MOLPRO [122].

We are using *ab-initio* electronic wavefunctions calculated at the CASSCF(2,24)/d-aug-cc-PVDZ level to account for the first 9 singlet electronic states included in the X-ray scattering picture. The *ab-initio* potential energy curves are benchmarked against reference potential energy curves calculated by Wolniewicz *et al.* [163]. The dynamics is propagated on the reference potential energy curves. The IXS matrix elements and the final time-resolved X-ray scattering signal are obtained using the procedures explained in Chapters 2 and 4.

6.4 Results

6.4.1 H_2 potential energy curves

We begin by examining the results obtained in the calculation of potential energy curves in H_2. As it is a diatomic molecule, it has only one nuclear degree of freedom, the interatomic distance. We use a CASSCF(2,24)/d-aug-cc-PVDZ method to calculate the eigenvalues for 9 singlet states with different symmetries. The grid in R goes from 0.5 to 7.0 a.u. with a stepsize of $\Delta R = 0.005$. In Fig. 6.1 we compare calculated *ab-initio* electronic energies as a function of the internuclear distance with the reference potential energy curves calculated by Wolniewicz *et al.* [164]. The agreement between our results and the reference results is reliable despite our use of a method without dynamical correlation. Using MRCI or CASPT2 would correct the differences between the two sets of results but, as we are accounting for nine states, this would also constitute a rather expensive calculation.

The H_2 states with a Π character are doubly degenerate, producing a change in the character of the wavefunction at $R > 3.5$ a.u.. To guarantee

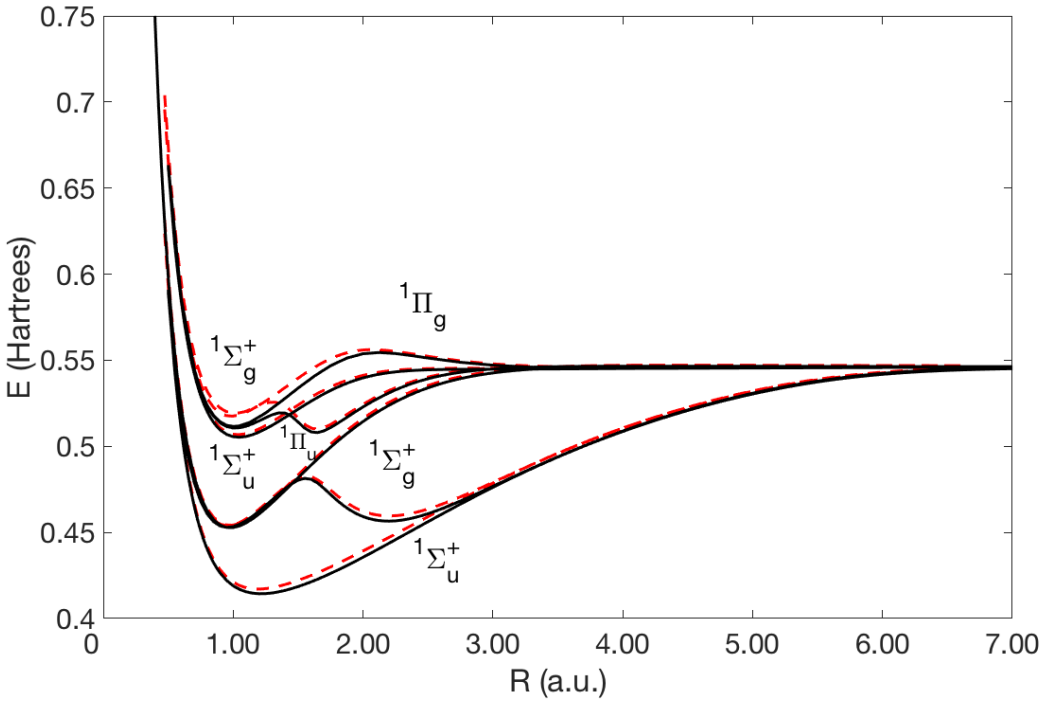

FIGURE 6.1: Comparison of the first eight singlet excited states in H_2 molecule (excluding ground state). The potential energy curves are calculated using *ab-initio* electronic calculations at CASSCF(2,24)/d-aug-cc-PVDZ level with an even-spaced grid on R. It is worth noting that $^1\Pi_u$ and $^1\Pi_g$ states are doubly degenerated. The reference potential energy curves (solid lines) are taken from Ref. [165].

the numerical continuity of scattering matrix elements, L_{ij}, we restrict our treatment to $0.5 < R < 3.5$ a.u.. In Fig. 6.2 we show the potentials labeled by their symmetries and the range we have used to perform our calculations.

6.4.2 Nuclear propagation results

The calculation of time-dependent wavefunctions has been carried out using the split-operator method as explained in Sec. (6.2.3). Diabatization of the potential energy curves is carried out using the method explained in Sec. 6.2.3. We are considering the first two $^1\Sigma_g^+$ states in the simulation, $2^1\Sigma_g^+$ and

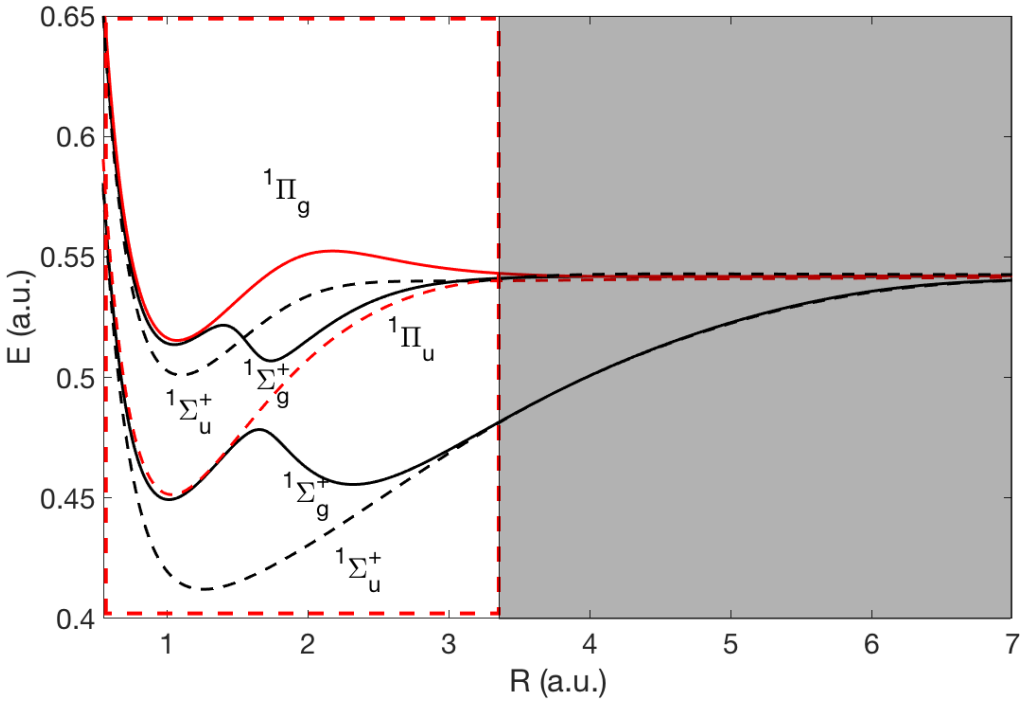

FIGURE 6.2: Potential energy curves with $n = 1, 2$ in H_2. The potential energy curves are calculated using *ab-initio* electronic calculations at CASSCF(2,24)/d-aug-cc-PVDZ level with an even spaced grid on R. The shadowed part indicates the region in which the scattering matrix elements are not continuous due to changes in the wavefunction character i.e. $R > 3.5$ a.u. .

$3^1\Sigma_g^+$, and to calculate their diabatic representation we use analytical potential energy curves and NACMEs from Wolniewicz *et al.* [165]. In Fig. 6.3 we can see a non-adiabatic representation of the two states, $2^1\Sigma_g^+$ and $3^1\Sigma_g^+$. It shows how both states are coupled, with a clear avoided-crossing region around 1.5 a.u..

The diabatic states represented in Fig. 6.3 are used in the time-propagation of the nuclear wavepacket. In Fig. 6.4 the initial conditions for the propagation are shown. As we can see, the initial population of the wavepacket is equal in both states, constructed using Gaussian functions with a width of 0.1 a.u., centred at 1.55 a.u. and an initial momentum of 0 a.u..

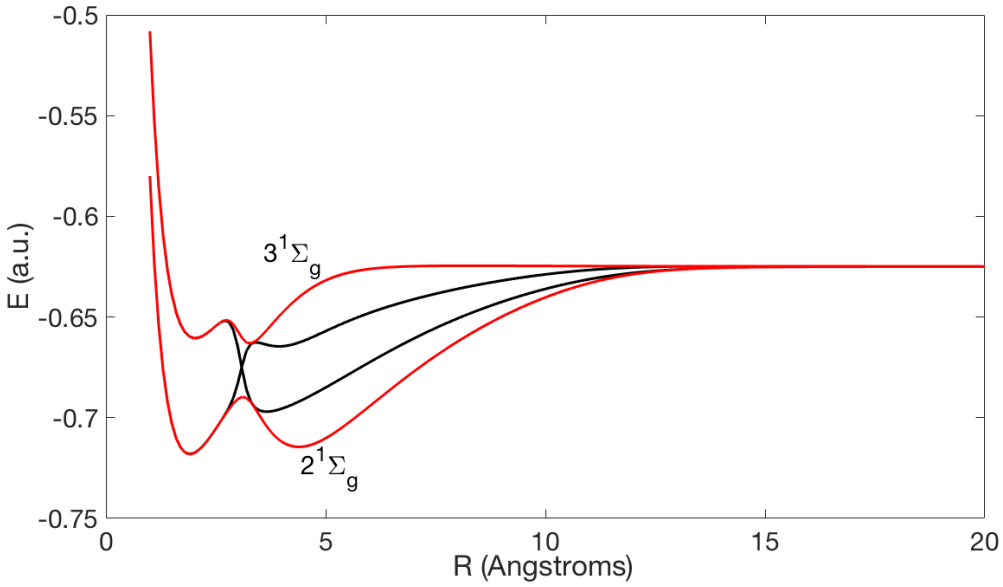

FIGURE 6.3: Adiabatic (red) and Non-Adiabatic (black) representations of the potential energy curves for the first two $^1\Sigma_g^+$ excited states in H_2 molecule.

The wavepacket simulation uses a time-step of 0.25 fs with 120 points. Once the simulation has finished, an adiabatization of the final results is carried out. In Fig. 6.10 we show the evolution of the adiabatic wavepackets. While the first excited state, $2^1\Sigma_g^+$, dissociates at 20 fs , the second excited state, $3^1\Sigma_g^+$, remains bound during all the simulation. A population transfer occurs at 6 fs between both levels via the avoided crossing.

The population of the first state increases to 80%, but the dispersion of both wavepackets is noticeable, coupling all possible R values in terms of scattering. This wavepacket simulation aims to be illustrative in order to study the time-resolved X-ray scattering signal. Nevertheless, in an actual experiment the bandwidth and characteristics of the pulse will determine the initial composition of the wavepacket.

6.4.3 Scattering Matrix Elements

In Eq. (6.2) different scattering matrix elements (SMEs), $L_{\alpha\beta}$, are considered. The treatment includes SMEs between the initial electronic states used in

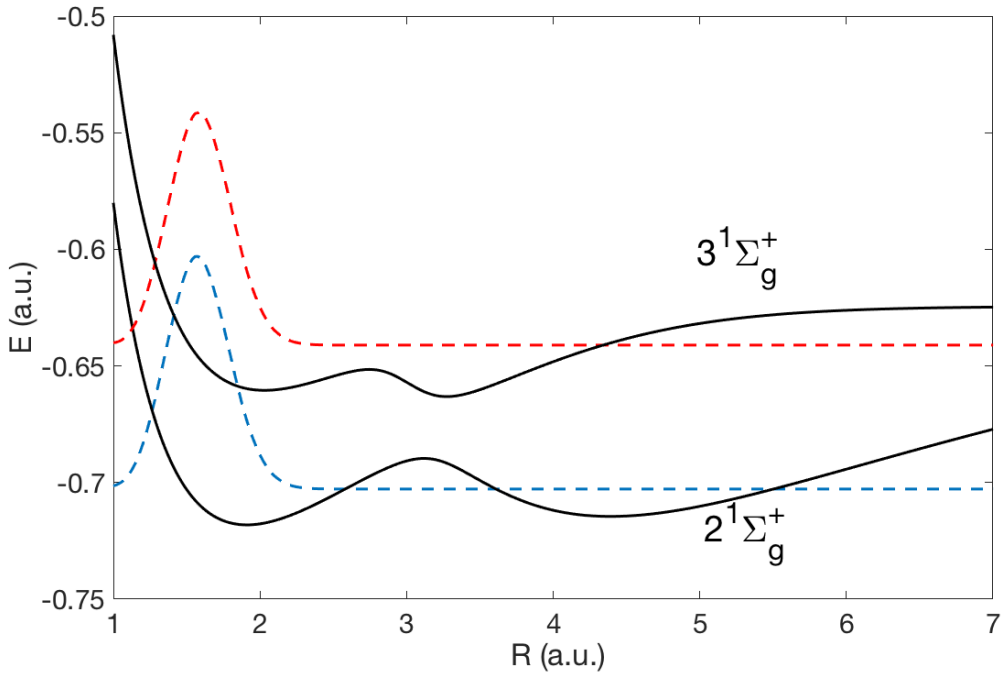

FIGURE 6.4: Initial conditions for the wavepacket propagation using $2^1\Sigma_g^+$ and $3^1\Sigma_g^+$ states in H_2. The initial populations are considered equal in both states. The wavepacket is simulated using a Gaussian function with a width of 0.1 a.u., centred at 1.55 a.u. and an initial momentum of 0 a.u..

the simulation, $2^1\Sigma_g^+$ and $3^1\Sigma_g^+$, and the bound electronic states included via the identity operator, $\mathbb{1} = \sum_k^\infty |\psi_k(\boldsymbol{r};\boldsymbol{R}\rangle\langle\psi_k(\boldsymbol{r};\boldsymbol{R}|$. We have considered nine singlet states in the simulation, producing 18 SMEs that are represented in Fig. 6.6. The calculated SMEs show smooth and continuous behaviour as we avoid the potential regions with $R > 3.5$ a.u., and their magnitude will be determined by the probability of transition between the states involved. The region of 1.5 a.u. shows clearly the fingerprint of the avoided crossing in most of the SMEs as the character of the electronic wavefunction changes rapidly at these values of the internuclear bond-distance, R.

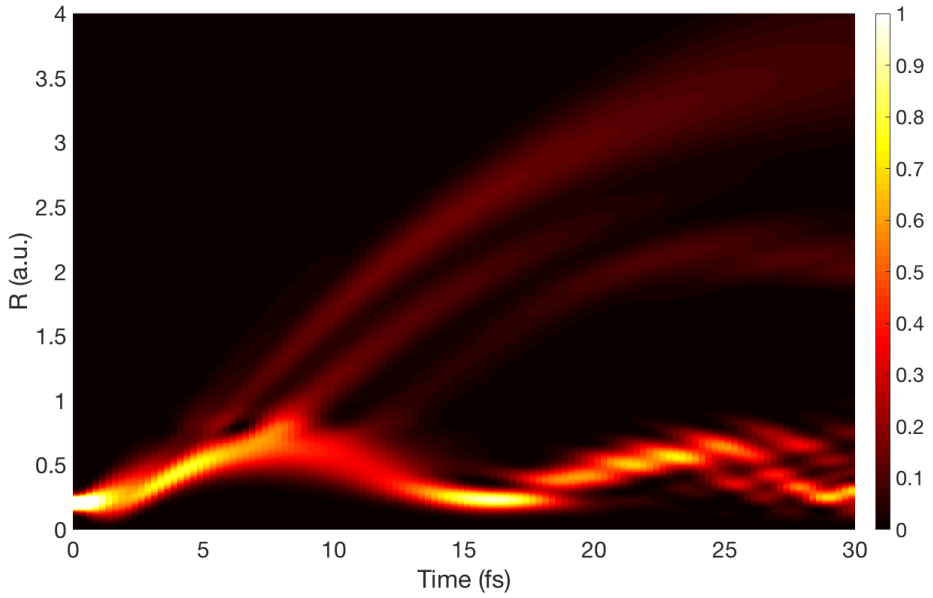

(A) $2^1\Sigma_g^+$ wave packet evolution in time.

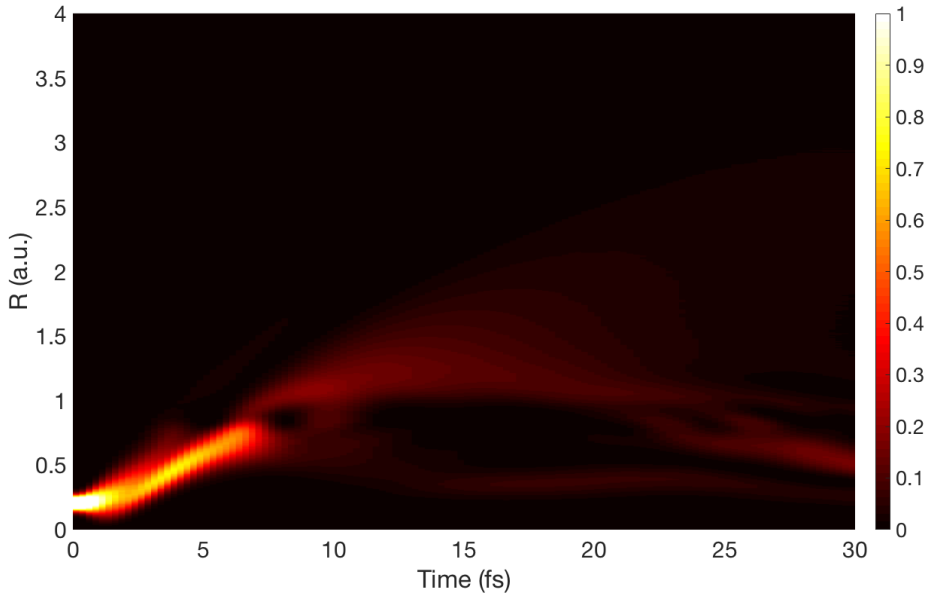

(B) $3^1\Sigma_g^+$ wave packet evolution in time.

FIGURE 6.5: Time-evolution of the adiabatic nuclear wave packet amplitudes, $|\chi(\boldsymbol{R}, t)|$, for the first two excited $^1\Sigma_g^+$ states in H_2. A) $2^1\Sigma_g^+$ state and B) $3^1\Sigma_g^+$ state. The amplitudes are calculated using the package WAVEPACKET.

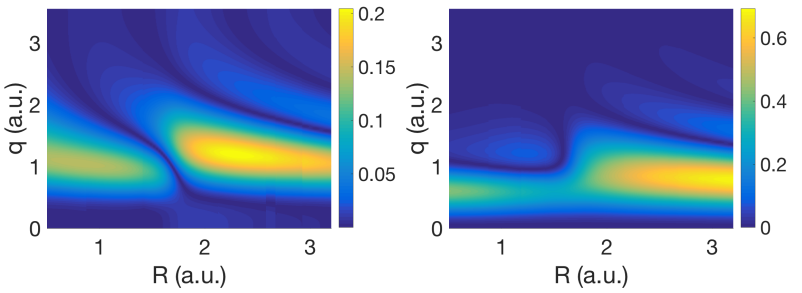

(A) $2^1\Sigma_g^+$-$1^1\Sigma_g^+$ (B) $2^1\Sigma_g^+$-$1^1\Sigma_u$

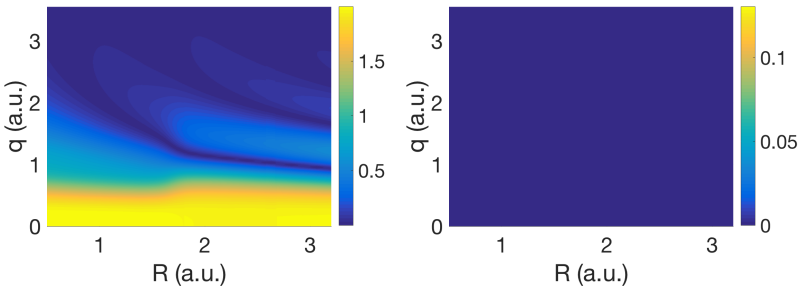

(C) $2^1\Sigma_g^+$-$2^1\Sigma_g^+$ (D) $2^1\Sigma_g^+$-$1^1\Pi_u$

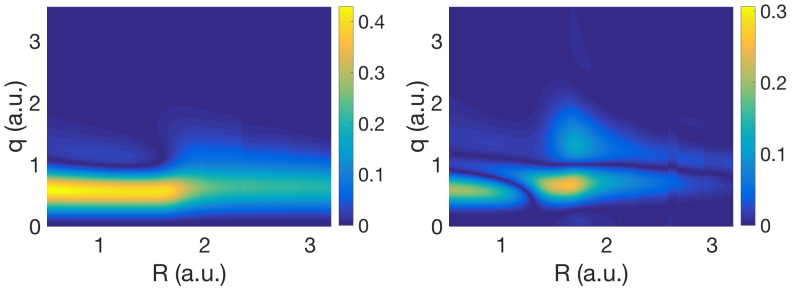

(E) $2^1\Sigma_g^+$-$1^1\Pi_u$ (F) $2^1\Sigma_g^+$-$3^1\Sigma_g^+$

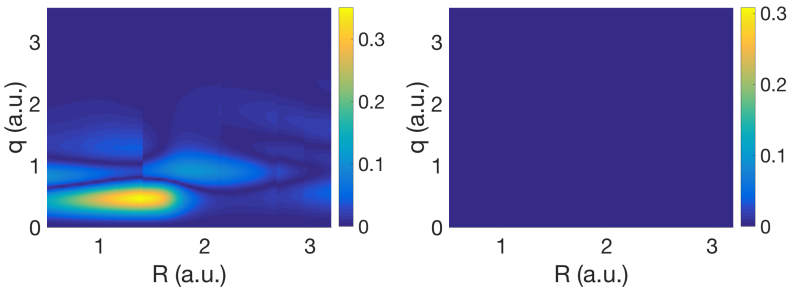

(G) $2^1\Sigma_g^+$-$2^1\Sigma_u$ (H) $2^1\Sigma_g^+$-$2^1\Sigma_u$

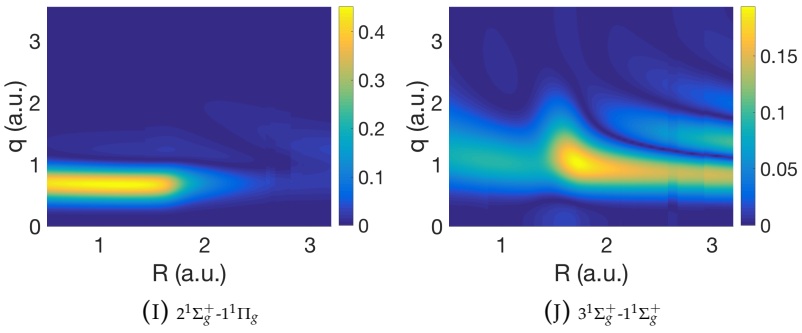

(I) $2^1\Sigma_g^+$-$1^1\Pi_g$

(J) $3^1\Sigma_g^+$-$1^1\Sigma_g^+$

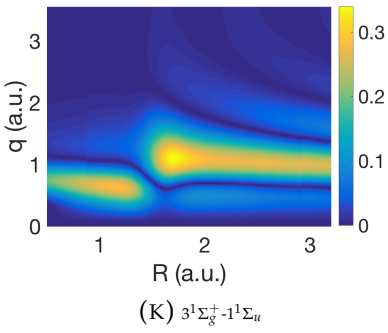

(K) $3^1\Sigma_g^+$-$1^1\Sigma_u$

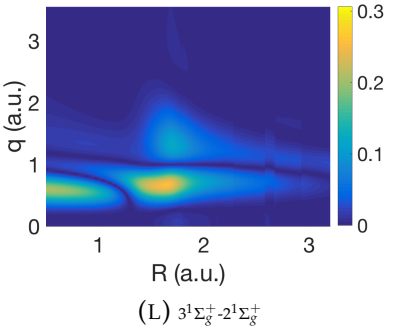

(L) $3^1\Sigma_g^+$-$2^1\Sigma_g^+$

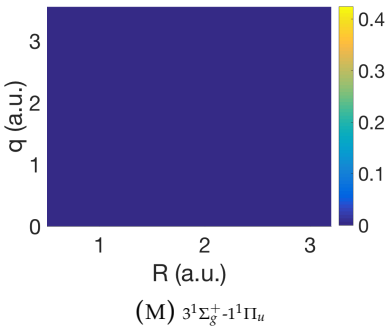

(M) $3^1\Sigma_g^+$-$1^1\Pi_u$

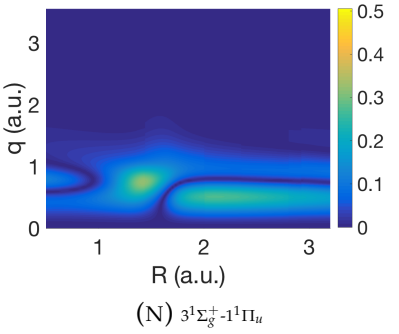

(N) $3^1\Sigma_g^+$-$1^1\Pi_u$

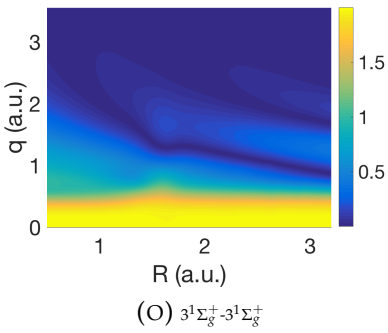

(O) $3^1\Sigma_g^+$-$3^1\Sigma_g^+$

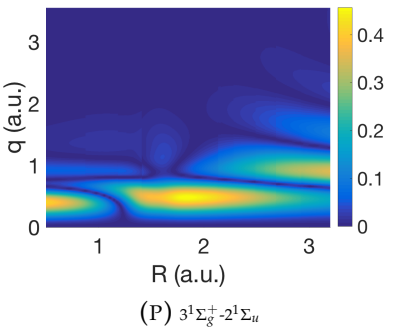

(P) $3^1\Sigma_g^+$-$2^1\Sigma_u$

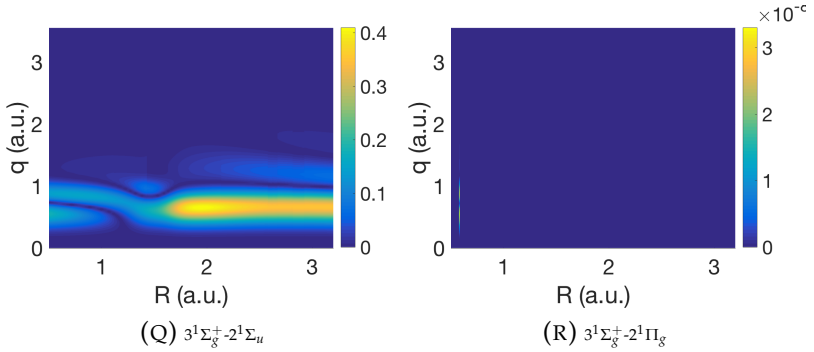

FIGURE 6.6: Scattering matrix elements, $L_{\alpha\beta}$, between the first 9 singlet states of H_2. The matrix elements are labeled using the states involved in the SME i.e. α-β.

6.4.4 Time-resolved X-ray scattering: The complete picture

The results obtained in the previous sections can be combined into Eq. (6.2) yielding an X-ray scattering time-dependent signal. The wavepacket encompassing the $2^1\Sigma_g^+$ and $3^1\Sigma_g^+$ states evolves in time and interacts with the X-ray photons. As this interaction involves two instances of the radiation field, we consider scattering as a two-step process in which the wavepacket interacts with the continuum of states in the molecule. This situation is represented in Fig. 6.7; the i and j indexes represent the electronic states considered within the wavepacket simulation and the index f the rest of electronic bound states.

Considering an X-ray intensity profile, $I(t-\tau)$, with a window of 0.5 a.u. in W_{fij}, one can simulate a time-resolved X-ray scattering situation in which only the states with $n < 2$ are considered (i.e. 9 states in the case of H_2 molecule). In order to represent the signal change in time we will use the percentage difference intensity, $\%\Delta I^{(\mathrm{sc})}(\tau)$. Taking as reference the initial wavepacket scattering intensity, $I^{\mathrm{sc}}(\tau=0)$, it reads,

$$\%\Delta I^{(\mathrm{sc})}(\tau) = \frac{I^{(\mathrm{sc})}(\tau) - I^{(\mathrm{sc})}(\tau=0)}{I^{(\mathrm{sc})}(\tau=0)} \cdot 100, \tag{6.21}$$

where $I^{(\mathrm{sc})}(\tau)$ is the scattering intensity collected by the detector at different probing times, $I(t-\tau)$.

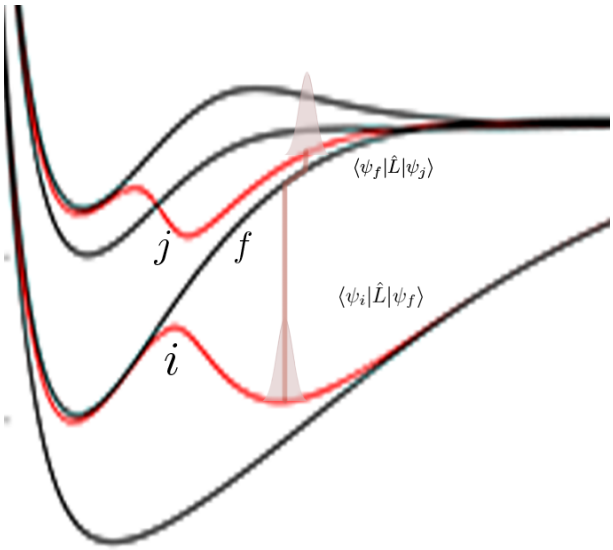

FIGURE 6.7: Schematic representation of the physical process taking place in the scattering event. The transitions are labeled according to equation 2.84. In this case $i \neq j \neq f$, reproducing an extreme situation. This indexes can take any value inside the framework studied.

In Fig. 6.8 we represent the full picture for the time-resolved X-ray scattering of a $2^1\Sigma_g^+$, $3^1\Sigma_g^+$ wavepacket in H_2. The changes in population between both states are collected by the signal. An initial non-adiabatic population transfer occurs at 6 fs, followed by a partial dissociation of the $3^1\Sigma_g^+$ state at 10 fs. In the $10 < \tau < 30$ fs range the signal shows an oscillatory behaviour as a direct consequence of the wavepacket movement but no population transfers occur.

The time-evolution of the signal is guided by the scattering interactions occurring between the X-ray and the molecule. The inclusion of inelastic scattering interactions between both $2^1\Sigma_g^+$ and $3^1\Sigma_g^+$ states will produce the most dramatic changes in the intensity collected by the detector, as demonstrated in Secs. 6.4.5 and 6.4.6.

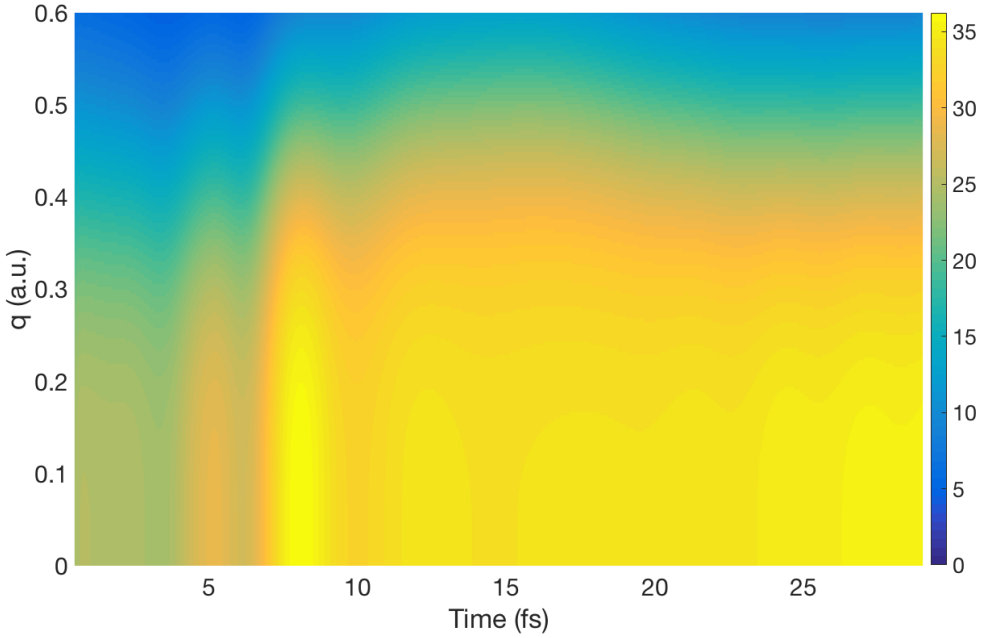

FIGURE 6.8: X-ray scattering intensity shown as percentage difference, $\%\Delta I$, for the time-evolution of a $2^1\Sigma_g^+/3^1\Sigma_g^+$ wavepacket in H_2 as a function of q and time. The X-ray scattering signal is calculated using Eq. (2.84) taking as the reference $I^{(\mathrm{sc})}(\tau = 0)$

.

6.4.5 Time-resolved X-ray scattering: The elastic picture

Considering only the elastic contributions in Eq. (6.2) leads to,

$$\frac{d\sigma}{d\Omega} = \frac{1}{2\pi}\left(\frac{d\sigma}{d\Omega}\right)_{\mathrm{Th}} \sum_i \int_0^\infty \int_{-\infty}^\infty I(t)\chi_i(\boldsymbol{R},t)^*\chi_i(\boldsymbol{R},t)dtL_{ii}^2 d\boldsymbol{R}, \tag{6.22}$$

where we have considered the scattering interaction as purely elastic and we have neglected the influence of the rest of states included via the identity operator, $\mathbb{1}$. The time-resolved elastic scattering signal is shown in Fig. 6.9. We can see that the non-adiabatic population transfer still produces a change in the intensity at 6 fs. Nevertheless, the difference with the complete picture in Fig. 6.8 is noticeable. The percentage difference is very small in comparison and the profile is not the same around population transfers.

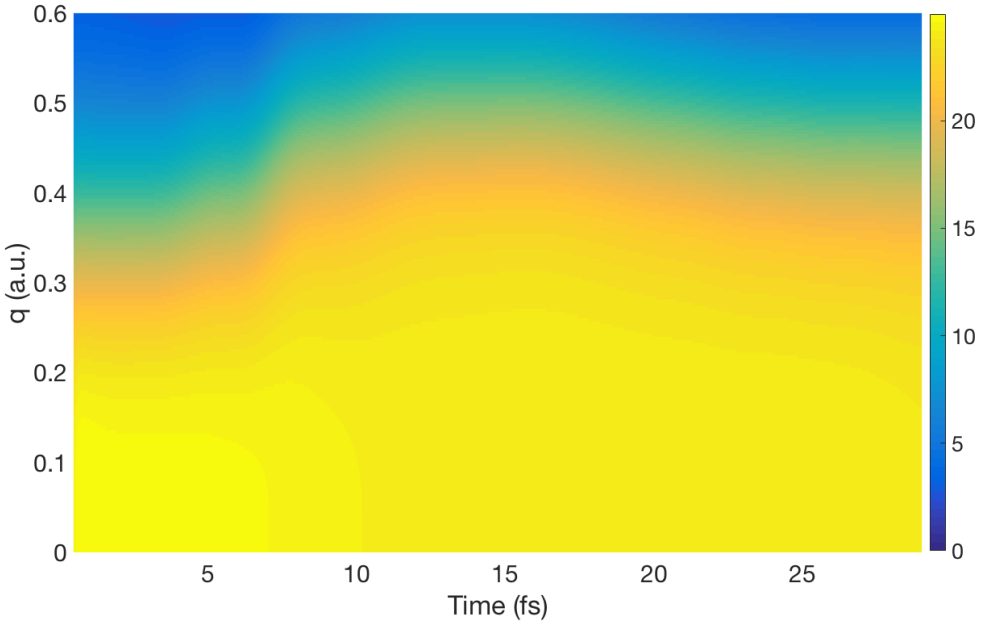

FIGURE 6.9: Elastic X-ray scattering intensity shown as percentage difference, $\%\Delta I$, for the time-evolution of a $2^1\Sigma_g^+/3^1\Sigma_g^+$ wavepacket in H_2 as a function of q and time. The X-ray scattering signal is calculated using Eq. (6.22) taking as the reference $I^{(\mathrm{sc})}(\tau = 0)$

The elastic population transfer between the states can be explained using the individual elastic scattering matrix elements for the $2^1\Sigma_g^+$ and $3^1\Sigma_g^+$ states and the difference between them. The percentage difference in Fig. 6.10 shows a maximum at $R = 1.5$ a.u., where the avoided crossing occurs.

6.4.6 Time-resolved X-ray scattering: The semi-complete picture

There is yet another picture that can be postulated for the study of time-dependent X-ray scattering. Considering that the X-ray scattering is a two-photon process, one might consider that the wavepacket scatters elastically but the process includes non-resonant interactions with the rest of states,

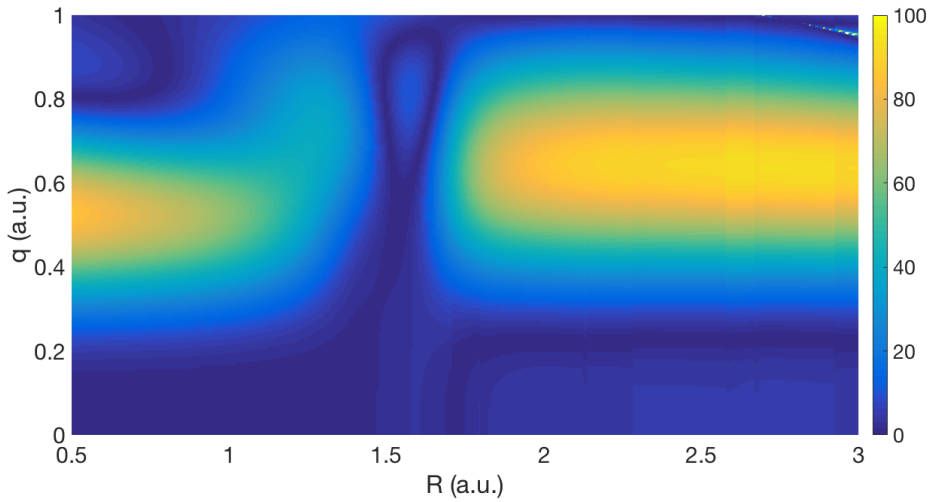

FIGURE 6.10: Percentage difference between $2^1\Sigma_g^+$ and $3^1\Sigma_g^+$ elastic scattering intensities.

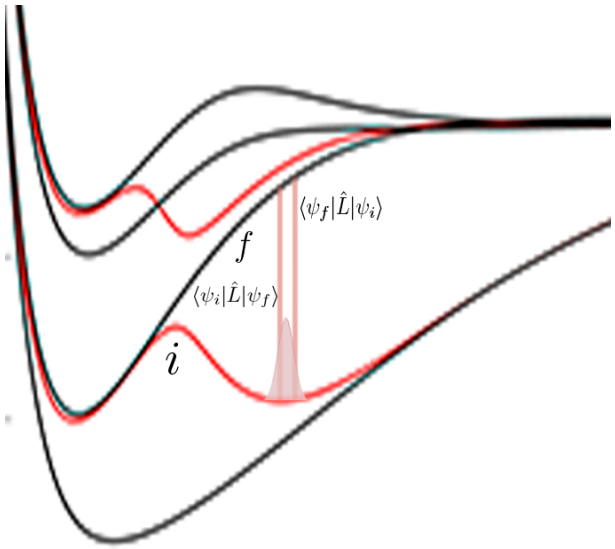

FIGURE 6.11: Schematic representation of the physical process taking place when only elastic wave packet scattering is considered. The transitions are labeled according to equation 6.23. In this case $i \neq f$. This indexes can take any value inside the framework studied.

$\mathbb{1} = \sum_f^\infty |f\rangle\langle f|$. Eq. (6.2) then is rearranged as follows,

$$\frac{d\sigma}{d\Omega} = \frac{1}{2\pi}\left(\frac{d\sigma}{d\Omega}\right)_{\text{Th}} \sum_{if} \int_0^\infty \int_{-\infty}^\infty I(t)\chi_i(\boldsymbol{R},t)^*\chi_i(\boldsymbol{R},t)dt \times L_{fi}^* L_{fi} W_{if}(\Delta\omega) d\omega_{k_s} d\boldsymbol{R}, \tag{6.23}$$

where only an elastic interaction is considered between the nuclear wavepackets. In Fig. 6.11 a schematic representation of the scattering process is shown.

In Fig. 6.12 we have represented the percentage intensity difference calculated using Eq. (6.23) and the percentage differences with respect to the pure elastic case calculated using Eq. (6.22) and the complete scattering process in Eq. (2.84). We can see that the effect of the rest of the bound states is negligible if only elastic scattering is considered between the wavepackets. Inelastic scattering terms guide the intensity changes of time-resolved scattering signal. Although small in magnitude, the SMEs coupling the two wavepackets are the key quantity to map the evolution of the system in time via X-ray scattering.

6.4.7 Conclusion

In this Chapter we have simulated time-resolved X-ray scattering in H_2. We have constructed our wavepacket from the first two excited $^1\Sigma_g^+$ states in H_2 and have propagated the wavepacket in time. The wavepacket propagation has been followed by the simulation of a the X-ray scattering signal at various pump-probe delay times.

We have explored the influence of IXS on the final time-resolved X-ray scattering. As demonstrated by Dixit *et al.* [24], the time-resolved X-ray scattering signal requires that IXS is included. Although the IXS terms are smaller in magnitude than elastic X-ray scattering terms, they are necessary to correctly account for the light-matter interaction guided by $\hat{A}^2$ terms in the interaction Hamiltonian. In this work, the importance of IXS has been demonstrated in practice. When only the elastic interactions are considered between the X-ray and the material system, the mapping does not reflect the features of the wavepacket propagation (see Fig. 6.9), even when the rest of states are included (see Fig. 6.12). However, as elastic scattering is directly related to the electron density of the molecule, the treatment of molecules with a higher number of core electrons will decrease the importance of IXS in the final scattering picture.

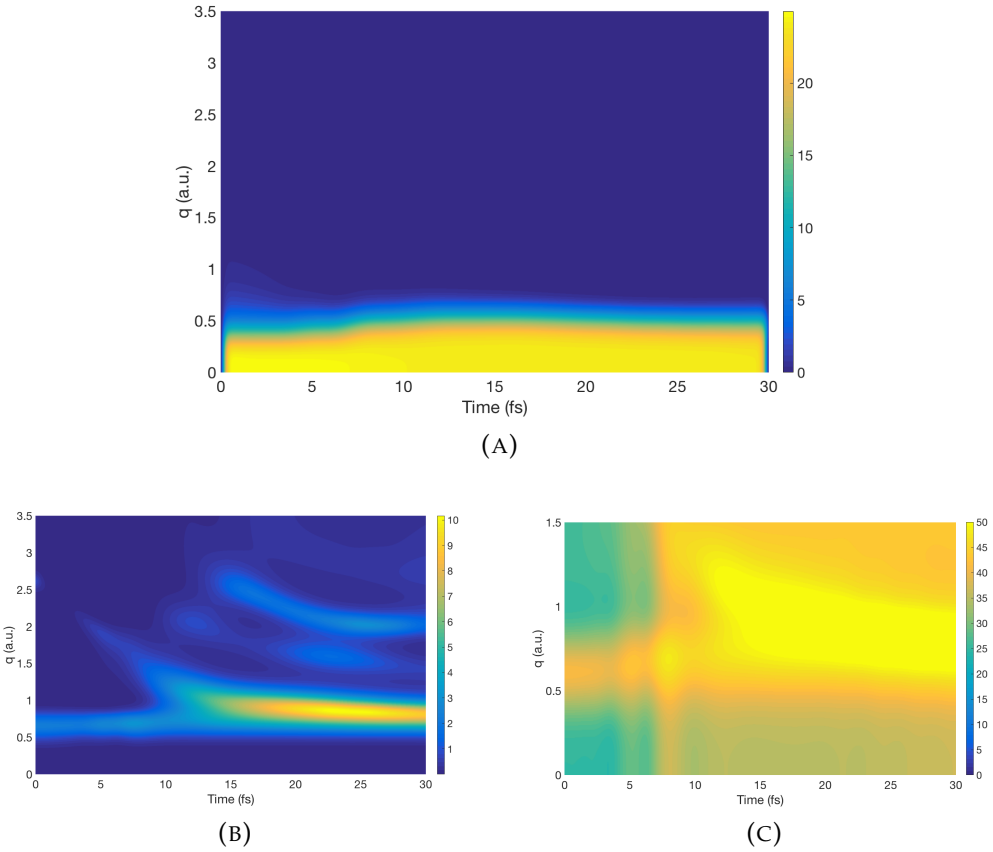

FIGURE 6.12: (A) Elastic X-ray intensity percentage difference, $\%\Delta I$, for the time-evolution of a $2^1\Sigma_g^+/3^1\Sigma_g^+$ wavepacket in H_2 as a function of q and time. This simulation includes the rest of the bound states in the scattering picture as expressed in Eq. (6.23). The reference is taken as $I^{(\mathrm{sc})}(\tau = 0)$. (B) Percentage difference between the pure elastic scattering picture and the elastic scattering picture including all bound states. (C) Percentage difference between the pure elastic scattering picture and the complete scattering picture

Chapter 7

Conclusion

In this thesis we have aimed to explain the main features of elastic and inelastic X-ray scattering from a theoretical point of view. We have tried to explain the main characteristics lying in the treatment of ultrafast X-ray scattering experiments and the computational methods required to calculate them. Based on the perspectives of different theoretical studies [11, 12, 24, 25, 80, 160] we have developed the theory and used our methods to simulate ultrafast X-ray scattering processes in atoms and molecules.

Starting with an introductory explanation about the history of X-rays, the experiments available using this X-ray scattering and the capabilities of novel X-ray sources, the main characteristics of the X-ray scattering processes have been unravelled.

The theory of X-ray scattering is explained from first principles in Ch. 2. The quantization of the electromagnetic field and the description of the interaction Hamiltonian have been followed by Fermi's golden rule to arrive at the stationary differential scattering cross-section. The non-stationary X-ray scattering differential cross-section is also derived using quantum electrodynamics, considering the atomic and molecular cases individually.

Once the theory is discussed, we examine the elastic X-ray scattering of state-selected molecules in Ch. 3 based on Refs. [1, 2]. Going beyond rotationally-averaged signals, and following the lead of recent experimental studies [14, 31, 112], we aim to explain how the aligned or state-selected molecules reflect their properties in their scattering patterns. Using the procedures developed in this thesis to calculate *ab-initio* X-ray scattering signals

[3, 84] and including rotational and vibrational contributions in the wavefunction of the system, we have characterised the influence of rotational and vibrational excitations in the X-ray scattering patterns of the CS_2 molecule.

In Ch. 4, which is based on Ref. [3], we calculate inelastic X-ray scattering in atoms (H, He^+,He, Na and C) and the N_2 molecule. The Chapter demonstrates how inelastic X-ray scattering can be calculated using *ab-initio* electronic wavefunctions and the effect of the quality of the *ab-initio* calculations is evaluated and benchmarked against reference values. Our approach is also validated by comparing our calculations with experimental data from inelastic X-ray scattering and electron energy-loss spectroscopies, showing an excellent agreement in both cases. The analogy between X-ray and electron scattering is discussed in some detail, with particular attention to the deviation of electron scattering signals at large values of q, corresponding to the break-down of the first Born approximation. Ch. 4 also presents the *ab-initio* X-ray scattering elastic and inelastic code (AIXRD), developed during this thesis. The code calculates elastic or inelastic X-ray scattering differential cross-sections for atoms and molecules, using *ab-initio* calculated electronic wavefunctions.

In Ch. 5 the temporal evolution of an excited coherent superposition of electronic states in hydrogen atoms is studied using time-resolved X-ray scattering. We validate our calculations by comparing them to Ref. [24]. The obtained scattering patterns show the importance of inelastic X-ray scattering in a physically correct description of the scattering process, as these elements entail all the temporal information in the X-ray scattering signal [13, 24].

In the final Chapter, Ch. 6, we combine all the previous results to carry out a simulation of time-resolved X-ray scattering in H_2 molecules. The molecular wavefunction is excited into a coherent superposition of nuclear and electronic states and its time-evolution is probed using X-ray scattering. In this case, the temporal information is also contained in the nuclear wavepackets, making it possible to produce time-dependent scattering patterns using elastic X-ray scattering. However the greatest contribution still comes from the IXS terms included in the full scattering picture.

The future directions of this work mainly fall in two categories. Firstly, the time-dependent picture developed in Chs. 5 and 6 could be applied to larger systems. In this thesis we have only treated two systems using time-resolved X-ray scattering, H and H_2, which present a low level of complexity in terms of their electronic structure. Systems with a larger number of nuclear degrees of freedom could be studied using our computational method. The dynamics simulations in larger molecules would require multidimensional methods such as multiconfigurational Ehrenfest [103], surface-hopping [105] or multiconfigurational time-dependent Hartree [102, 166] to carry out the nuclear wavepacket propagation. The X-ray scattering calculations will need to be revisited to consider larger and more complex molecules. Photochemical reactions such as the dissociation of a diiodobenzene [22] or the ring-opening reaction in 1,3-cyclohexadiene [21], could be studied using time-resolved X-ray scattering beyond the independent atom model [47] by using our *ab-initio* electronic wavefunction-based methods. The importance of these studies will not only rely on the characterisation of the time-evolution but also in the importance of IXS when larger number of electrons and nuclear degrees of freedom are considered.

Secondly, improvements could be made in the QED description of the time-resolved X-ray scattering picture. At the moment, only bound states are considered in the identity operator, $\mathbb{1} = \sum_f |f\rangle\langle f|$. However, as we calculate non-resonant X-ray scattering, also transitions into the continuum can also take place via IXS. The consideration of continuum states using multichannel quantum defect theory [167] or Dyson orbitals [25, 157] can be included in the time-dependent picture yielding the specific fingerprint of the particle-hole X-ray scattering. We aim to study how the excitations into the continuum affect the X-ray scattering patterns in the H-atom, where the continuum wavefunctions are analytical, and in larger systems, by using for instance a momentum representation for the wavefunctions [25].

Finally, interfacing the AIXRDEI code with other electronic structure softwares than MOLPRO [122] and a wider range of methods would be a priority. As our code is based on the treatment of Gaussian type orbitals

to calculate the X-ray scattering signal, any method, such as density functional theory [168], or even the plane wave expansion in periodic systems, could be treated by new computational implementations of our Gaussian functions-based approach.

Bibliography

[1] T. Northey *et al. J. Chem. Phys.* **145**. Elastic X-ray scattering from state-selected molecules, 154304 (2016).

[2] A. M. Carrascosa, T. Northey, and A. Kirrander. *Phys. Chem. Chem. Phys.* **19**. Imaging rotations and vibrations in polyatomic molecules with X-ray scattering, 7853 (2017).

[3] A. Moreno Carrascosa and A. Kirrander. *Phys. Chem. Chem. Phys.* **19**. Ab initio calculation of inelastic scattering, 19545 (2017).

[4] A. M. Carrascosa and A. Kirrander. *Manuscript*. Time-resolved X-ray scattering from LiF molecules (2017).

[5] A. M. Carrascosa and A. Kirrander. *Manuscript*. Time-resolved X-ray scattering from H-Atom electronic wavepackets (2017).

[6] A. M. Carrascosa *et al. Manuscript*. Time-resolved X-ray scattering from H_2 molecules (2017).

[7] J. Larsson. *Meas. Sci. Technol.* **12**, 1835 (2001).

[8] R. Neutze *et al. Phys. Rev. Lett.* **87**, 195508 (2001).

[9] M. P. Minitti *et al. Phys. Rev. Lett.* **114**, 255501 (2015).

[10] A. Kirrander, K. Saita, and D. V. Shalashilin. *J. Chem. Theory Comput.* **12**, 957 (2016).

[11] U. Lorenz, K. B. Møller, and N. E. Henriksen. *Phys. Rev. A* **81**, 023422 (2010).

[12] K. B. Møller and N. E. Henriksen. *Struct. Bond.* **142**, 185 (2012).

[13] M. Simmermacher, N. E. Henriksen, and K. B. Moller. *Phys. Chem. Chem. Phys.* **19**, 19740 (2017).

[14] J. Yang *et al. Phys. Rev. Lett.* **117**, 153002 (2016).

[15] S. Westenhoff *et al. Ac. Cryst. Sect. A Found. Cryst.* **66**, 207 (2010).

[16] M. Wulff *et al.* **879**, 1187 (2007).

[17] J. Yang *et al. Nat. Comm.* **7**, 11232 (2016).

[18] M. Bargheer *et al. Chem. Phys. Chem.* **7**, 783 (2006).

[19] K. J. Gaffney and H. N. Chapman. *Science* **316**, 1444 (2007).

[20] R. C. Dudek and P. M. Weber. *J. Phys. Chem. A.* **105**, 4167 (2001).

[21] M. P. Minitti *et al. Faraday Discuss.* **171**, 81 (2014).

[22] B. Stankus *et al. Faraday Discuss.* **194**, 525 (2016).

[23] J. Cao and K. R. Wilson. *J. Phys. Chem.* **102**, 9523 (1998).

[24] G. Dixit, O. Vendrell, and R. Santra. *Proc. Natl. Acad. Sci.* **109**, 11636 (2012).

[25] M. Grosser, J. M. Slowik, and R. Santra. *Phys. Rev. A* **95**, 062107 (2017).

[26] M. Kowalewski, K. Bennett, and S. Mukamel. *Structural Dynamics* **4**, 054101 (2017).

[27] L. Zhu *et al. J. Phys. B* **44**, 025203 (2011).

[28] L.-F. Zhu *et al. Chinese Phys. B* **24**, 43101 (2015).

[29] L. F. Zhu *et al. Phys. Rev. A* **85**, 030501 (2012).

[30] U. Lorenz, K. B. Møller, and N. E. Henriksen. *New J. Phys.* **12**, 113022 (2010).

[31] J. M. Glownia *et al. Phys. Rev. Lett.* **117**, 153003 (2016).

[32] H. Christopher, J. Yang, and M. Centurion. *Phys. Rev. Lett.* **109**, 133202 (2012).

[33] J. Yang *et al. Nat. Comm.* **6**, 8172 (2015).

[34] J. Yang *et al. Nat. Comm.* **7**, 11232 (2016).

[35] J. G. Anderson. *Trans. Fac. Act.* **17**, 219–221 (1945).

[36] W. C. Röntgen. *Science* **3**, 227 (1896).

[37] M. V. Laue. *Nobelprize.org. Nobel Media AB 2014* (1915).

[38] W. H. Bragg and W. L. Bragg. *Nature* **91**, 557 (1913).

[39] W. L. Bragg, R. James, and C. Bosanquet. *Phil. Mag.* **44**, 433 (1922).

[40] J. D. Watson and F. H. C. Crick. *Nature* **171**, 737 (1953).

[41] D. C. Hodgkin, R. S. Harris, and K. V. Thimann. "X-Ray Crystallography and Sterol Structure". Vol. 2. *Vitamins & Hormones*, 409 (1944).

[42] D. C. Hodgkin *et al. Nature* **178**, 64 EP (1956).

[43] M. Perutz. *Proc. R. Soc. Lond. A. Math. Phys. Sci.* **225**, 287 (1954).

[44] M. F. Perutz *et al. Nature* **185**, 416 EP (1960).

[45] W. D. Coolidge. *Phys. Rev.* **2**, 409 (1913).

[46] M. Deutsch *et al. Phys. Rev. A* **51**, 283 (1995).

[47] P. Debye. *Ann. Phys.* **46**, 809 (1915).

[48] J. Als-Nielsen and D. McMorrow. *Elements of Modern X-Ray Physics*. First Edition. John Wiley And Sons Ltd, 2001.

[49] D. Iwanenko and I. Pomeranchuk. *Phys. Rev.* **65**, 343 (1944).

[50] J. Ellis, N. Mavromatos, and A. Sakharov. *Astropart. Phys.* **20**, 669 (2004).

[51] E. F. Garman. *Science* **343**, 1102 (2014).

[52] J. M. J. Madey. *J. Appl. Phys.* **42**, 1906 (1971).

[53] D. A. G. Deacon *et al. Phys. Rev. Lett.* **38**, 892 (1977).

[54] W Ackermann *et al. Nat. Phot.* **1**, 336 (2007).

[55] P. M. W. Aseyev Sergei A. and A. A. Ischenko. *J. Anal. Sci. Meth. Instr.* **03**, 30 (2013).

[56] M. Jaskolski, Z. Dauter, and A. Wlodawer. *FEBS Journal* **281**, 3985 (2014).

[57] H. N. Chapman *et al. Nature* **470**, 73 (2011).

[58] H. N. Chapman, C. Caleman, and N. Timneanu. *Philos. Trans. R. Soc. Lond., B, Biol. Sci.* **369** (2014).

[59] T. Ekeberg *et al. Phys. Rev. Lett.* **114**, 098102 (2015).

[60] U. Weierstall *et al. Nat. Comm.* **5**, 3309 EP (2014).

[61] M. Sugahara *et al. Nat. Methods* **12**, 61 EP (2014).

[62] A. Y. Lyubimov *et al. Acta Crystallogr. Sect. D-Biol. Crystallogr.* **71**, 928 (2015).

[63] S. Oghbaey *et al. Acta Crystallogr. Sect. D-Biol. Crystallogr.* **72**, 944 (2016).

[64] J. M. Budarz *et al. J. Phys. B* **49**, 034001 (2016).

[65] J. Davidsson *et al. Phys. Rev. Lett.* **94**, 245503 (2005).

[66] Q. Kong *et al. Acta Cryst. A* **66**, 252 (2010).

[67] M. Levantino *et al. Nat. Comm.* **6**, 6772 EP (2015).

[68] K. H. Kim *et al. Nature* **518**, 385 EP (2015).

[69] J. Küpper *et al. Phys. Rev. Lett.* **112**, 083002 (2014).

[70] M. Ben-Nun, J. Cao, and K. Wilson. *J. Phys. Chem. A* **101**, 8743 (1997).

[71] V. S. Petrović *et al. Phys. Rev. Lett.* **108**, 253006 (2012).

[72] N. Berrah. *Phys. Script.* **2016**, 014001 (2016).

[73] P. Weinberger. *Philos. Mag. Lett.* **86**, 405 (2006).

[74] H. Ihee *et al. Science* **291**, 458 (2001).

[75] R. Srinivasan *et al. Helv. Chim. Acta* **86**, 1763 (2003).

[76] D. Shorokhov, S. T. Park, and A. H. Zewail. *Chem. Phys. Chem.* **6**, 2228 (2005).

[77] W. Schülke. *Electron Dynamics by Inelastic X-Ray Scattering*. First. Oxford Science Publications, 2007.

[78] L. X. Chen *et al. Acta Crystallographica Section A Foundations of Crystallography* **66**, 240 (2010).

[79] C. Bressler and M. Chergui. *Annual Review of Physical Chemistry* **61**, 263 (2010).

[80] R. Santra. *J. Phys. B* **42**, 023001 (2009).

[81] S. Schreck, M. Beye, and A. Föhlisch. *Journal of Modern Optics* **62**, S34 (2015).

[82] K Hämäläinen and S Manninen. *Journal of Physics: Condensed Matter* **13**, 7539 (2001).

[83] R. Loudon. *The Quantum Theory of Light*. Oxford University Press, 2000.

[84] T. Northey, N. Zotev, and A. Kirrander. *J. Chem. Theory Comput.* **10**, 4911 (2014).

[85] *International Tables for Crystallography Volume C: Mathematical, physical and chemical tables*. 2006th ed. Wiley, 2006.

[86] M. A. Coulthard. *Procs. Phys. Soc.* **91**, 44 (1967).

[87] A. G. Fox, M. A. O'Keefe, and M. A. Tabbernor. *Act. Cryst. A.* **45**, 786 (1989).

[88] P. A. Doyle and P. S. Turner. *Act. Cryst. A* **24**, 390 (1968).

[89] C. Cohen-Tannoudji, B. Diu, and F. Laloe. *Quantum Mechanics*. J. Wiley and Sons, 1977.

[90] D. R. Hartree. *Math. Proc. Camb. Philos. Soc.* **24**, 89–110 (1928).

[91] V. Fock. *Zeit. Phys.* **61**, 126 (1930).

[92] J. C. Slater. *Phys. Rev.* **81**, 385 (1951).

[93] G. G. Hall. *Proc. Royal Soc. A* **205**, 541 (1951).

[94] C. C. J. Roothaan. *Rev. Mod. Phys.* **23**, 69 (1951).

[95] P. W. Atkins. *Molecular Quantum Mechanics*. Second. Oxford University Press, 1983.

[96] A. Szabo and N. S. Ostlund. *Modern Quantum Chemistry: Introduction to Advanced Electronic Structure Theory*. Second. Dover Publishing Inc., 1996.

[97] P.-O. Löwdin. *Phys. Rev.* **97**, 1474 (1955).

[98] W. Heisenberg. *Zeitschrift für Physik* **33**, 879 (1925).

[99] P. A. M. Dirac. *Nature* **203**, 115 (1964).

[100] F. Gatti. *Molecular Quantum Dynamics: From Theory to Applications*. First Edition. Springer, 2014.

[101] D. J. Tannor, ed. *Introduction to Quantum mechanics: A time-dependent perspective*. First Edition. University Science Books, 2006.

[102] M. Beck *et al. Phys. Rep.* **324**, 1 (2000).

[103] K. Saita and D. V. Shalashilin. *J. Phys. Chem.* **137**, 22A506 (2012).

[104] M. Ben-Nun and T. J. Martinez. *Chem. Phys.* **259**, 237 (2000).

[105] S. Mai *et al. SHARC: Surface Hopping Including Arbitrary Couplings — Program Package for Non-Adiabatic Dynamics*. sharc-md.org. 2014.

[106] S. P. Hau-Riege. *Nonrelativistic Quantum X-Ray Physics*. First. Wiley, 2014.

[107] H. Bethe. *Ann. Phys.* **397**, 325 (1930).

[108] M. Inokuti. *Rev. Mod. Phys.* **43**, 297 (1971).

[109] Y.-W. Liu *et al. Phys. Rev. A* **89**, 014502 (2014).

[110] V. Lyamayev *et al. J. Phys. B* **46**, 164007 (2013).

[111] J. Küpper *et al. arXiv pre-print 1307.4577* (2013).

[112] J. Yang *et al. Faraday Discuss.* – (2016).

[113] G. Sitz and R. L. Farrow. *J. Chem. Phys.* **101**, 4682 (1994).

[114] A. D. Rudert *et al. J. Chem. Phys.* **111**, 9549 (1999).

[115] N. C. M. Bartlett *et al. J. Chem. Phys.* **129**, 084312 (2008).

[116] N. Mukherjee and R. N. Zare. *J. Chem. Phys.* **135**, 024201 (2011).

[117] N. Mukherjee *et al. J. Chem. Phys.* **138**, 051101 (2013).

[118] I. Waller and D. R. Hartree. *Proc. R. Soc. Lond. Ser.-A* **124**, 119 (1929).

[119] P. R. Bunker and P. Jensen. *Molecular Symmetry and Spectroscopy*. Second Edition. NRC Research Press, 1998.

[120] A. G. Fox, M. A. O'Keefe, and M. A. Tabbernor. *Acta Cryst.* **A45**, 786 (1989).

[121] P. A. Doyle and P. S. Turner. *Acta Cryst.* **A24**, 390 (1968).

[122] H.-J. Werner *et al. MOLPRO, version 2012.1, a package of ab initio programs*.

[123] R. F. Stewart, E. R. Davidson, and W. T. Simpson. *J. Chem. Phys.* **42**, 3175 (1965).

[124] N. P. R. Data. *http://www.nist.gov/*.

[125] M. R. Pressprich, M. A. White, and P. Coppens. *J. Am. Chem. Soc.* **115**, 6444 (1993).

[126] M. R. Pressprich *et al. J. Am. Chem. Soc.* **116**, 5233 (1994).

[127] M. Minzer *et al. Rev. Sci. Instr.* **79**, 086101 (2008).

[128] R. Verbeni *et al. J. Synchr. Rad.* **16**, 469 (2009).

[129] J. A. Bradley *et al. Phys. Rev. Lett.* **105**, 053202 (2010).

[130] J. A. Bradley *et al. Phys. Rev. A* **84**, 022510 (2011).

[131] B. Xie *et al. Phys. Rev. A* **82**, 032501 (2010).

[132] X. Kang *et al. Phys. Rev. A* **86**, 022509 (2012).

[133] Y.-G. Peng *et al. Phys. Rev. A* **89**, 032512 (2014).

[134] K. H. Kim *et al. Nature* **518**, 385 (2015).

[135] R. S. Minns and A. Kirrander. *Faraday Discuss.* **194** (2016).

[136] M. Y. Amusia *et al. Phys. Rev. A* **65**, 062705 (2002).

[137] H. B. Schlegel and M. J. Frisch. *Int. J. Quant. Chem.* **54**, 83 (1995).

[138] A. Kirrander. *J. Chem. Phys.* **137**, 154310 (2012).

[139] A. Szabo and N. S. Ostlund. *Chem. Phys. Lett.* **17**, 163 (1972).

[140] W. Martin and W. Wiese. "Atomic Spectroscopy". *Atomic, Molecular and Optical Physics Handbook*. Ed. by G. Drake. http://physics.nist.gov. AIP, Woodbury, NY, 1996. Chap. 10, 135.

[141] N. M. Cann and A. J. Thakkar. *J. Elec. Spectr. Rel. Phenom.* **123**, 143 (2002).

[142] H.-D. Cheng *et al. Phys. Rev. A* **72**, 012715 (2005).

[143] L. Gomis *et al. Phys. Scripta* **76**, 494 (2007).

[144] Z. Chen and A. Z. Msezane. *Phys. Rev. A* **70**, 032714 (2004).

[145] C. E. Bielschowsky *et al. Phys. Rev. A* **43**, 5975 (1991).

[146] W. L. Wiese, M. W. Smith, and B. M.Glennon. *Atomic Transition Probabilities*. Nat. Bur. Stand., Washington DC, 1966.

[147] K. T. Leung. *J. Electr. Spectr. Rel. Phenom.* **100**, 237 (1999).

[148] R. S. Barbieri and R. A. Bonham. *Phys. Rev. A* **45**, 7929 (1992).

[149] T. Giannerini, I. Borges, and E. Hollauer. *Phys. Rev. A* **75**, 012706 (2007).

[150] S. Chung and C. C. Lin. *Appl. Opt.* **10**, 1790 (1971).

[151] A. Sakko *et al. J. Chem. Phys.* **133**, 174111 (2010).

[152] E. Fainelli *et al. Il Nuovo Cimento D* **9**, 33 (1987).

[153] M. Stefanou *et al. Chem. Phys. Lett.* (2017).

[154] A. Kirrander and H. H. Fielding and Ch. Jungen. *J. Chem. Phys.* **127**, 164301 (2007).

[155] A. Kirrander and H. H. Fielding and Ch. Jungen. *J. Phys. B* **41**, 074022 (2008).

[156] A. Kirrander, C. Jungen, and H. H. Fielding. *Phys. Chem. Chem. Phys.* **12**, 8948 (2010).

[157] C. M. Oana and A. I. Krylov. *J. Chem. Phys.* **127**, 234106 (2007).

[158] P. Emma *et al. Nat. Photon.* **4**, 641 (2010).

[159] T. Ishikawa *et al. Nat. Photon.* **6**, 540 (2012).

[160] G. Dixit and R. Santra. *J. Chem. Phys.* **138**, 134311 (2013).

[161] F. T. Smith. **118**, 349 (1960).

[162] E. F. van Dishoeck *et al. J. Chem. Phys.* **81**, 5709 (1984).

[163] G. Staszewska and L. Wolniewicz. *J. Mol. Spec.* **198**, 416 (1999).

[164] L. Wolniewicz. *J. Mol. Spec.* **174**, 132 (1995).

[165] L. Wolniewicz. **233**, 647 (1995).

[166] H.-D. Meyer, U. Manthe, and L. Cederbaum. *Chem. Phys. Lett.* **165**, 73 (1990).

[167] C. Jungen. "Elements of Quantum Defect Theory". *Handbook of High-resolution Spectroscopy*. Ed. by M. Quack and F. Merkt. Wiley, 2010.

[168] W. Kohn and L. J. Sham. *Phys. Rev.* **140**, A1133 (1965).